Acoustic Anemometry on the Surface of Mars



Eurion Leonard-Pugh

Oriel College

A Thesis submitted for the degree of

Doctor of Philosophy

Trinity Term 2014

Acoustic Anemometry on the Surface of Mars

Eurion Leonard-Pugh, Oriel College

Submitted for the degree of Doctor of Philosophy, Trinity Term 2014

ABSTRACT

There is a need for wind sensors with high accuracy and measurement frequency for deployment on the surface of Mars. The wind data obtained to date have been adversely affected by thermal contamination and calibration issues. Improved data would not only help to constrain and validate theoretical models, but also increase safety and longevity of lander operations. The mechanical and thermal wind sensing techniques used on previous missions, whilst sufficient for basic meteorology, are wholly inadequate for measuring fundamental phenomena such as dust and volatile transport. Two promising technologies, optical and acoustic anemometry, could permit precise and high-frequency measurement of three-dimensional wind speeds on the Martian surface. Ultrasonic acoustic anemometry, which relies on time-of-flight measurements, was ultimately chosen for its lower processing requirements and ability to measure the speed of sound; and therefore temperature. Capacitive transducers were selected for their low impedance and high sensitivity, to maximise signal transmission through the rarefied Martian atmosphere. These transducers, which consist of a metallised polymer film oscillating on top of a contoured metal backplane, were evaluated for their suitability as anemometers on the Martian surface.

A theoretical framework was assembled to model transducer performance and determine which factors are the most important in determining received signal amplitude. A pair of transducers were designed and manufactured to allow for testing of a wide range of parameters including thickness of the oscillating membrane and diameter. Tests were carried out on the assembled transducers to investigate the dependence on these parameters, and their behaviour was generally found to fit the assembled theoretical framework well. Transducer performance was highly dependent on roughness depth of the backplanes, as expected. The frequency response of the transducers was dominated by the backplane roughness at atmospheric pressure but by film thickness at low pressures. Cross-correlation of the sent and received signals was confirmed as the most reliable signal detection method at low signal amplitudes.

The transducers were tested under simulated Martian conditions (a low-pressure carbon dioxide atmosphere with airborne dust), and found to be capable of accurately and reliably measuring the incident wind speed. The cumulative deposition of airborne dust noticeably reduced received signal amplitude, but further testing is required to determine the effect of significant amounts of dust on transducer performance. The impact of the transducer heads impeding the incident fluid flow was found to be very significant in wind tunnel testing. Preliminary computational models were found to accurately predict these effects, but a more comprehensive modelling campaign and experimental validation would be required to ensure accurate instrument calibration.

ACKNOWLEDGEMENTS

This work would not have been possible without the help of various people. Firstly, I would like to thank my supervisors Simon Calcutt and Colin Wilson for their invaluable guidance throughout the project. I will be forever indebted to my brilliant office-mate Lauren Fletcher; whose relentless enthusiasm and engaging discussions guaranteed that there was never a dull day at the office. From Aarhus University, I would like to extend my thanks to Jon Merrison and Jacob Iversen for showing me how to use the AWTS and for clearing up the dust after testing. From the Osney Thermo-Fluids Laboratory, thanks are due to Peter Ireland, Hal Surtell and Paul Cox for helping ensure that the wind tunnel relocation was as painless as possible. I am grateful to Lee Davis of Warwick University for the use of his facilities and experience in troubleshooting the prototype transducers. From the workshops, I would like to thank Jon Temple, Andy Clack, Jason Perry and Duncan Constable for taking the time to share their technical expertise and contacts around the department. I am especially grateful to my fellow students and the members of the Planetary group for the infamous Friday afternoon pub lunches.

Outside the office, there were plenty of people responsible for me receiving the full Oxford experience. My gratitude goes to the members of the OURC for all the top-notch banter, and to the associates of the Oriel MCR for ensuring that my social calendar was never empty.

On a more personal note, heartfelt thanks go out to my parents for their encouragement and support throughout my education. Finally, my utmost thanks goes to my sister Heilin-Anne for always being there for me.

CONTENTS

Abstract i

Acknowledgements iii

List of Nomenclature vii

1. Introduction 1
1.1 The Martian Atmosphere 1
1.1.1 Atmospheric Scales 3
1.1.2 The Planetary Boundary Layer 5
1.1.3 Turbulence 8
1.1.4 Dust 9
1.1.5 Volatiles 12
1.1.6 Wind Speeds on Mars 13
1.2 Past Anemometry Techniques 15
1.2.1 Thermal Methods 15
1.2.2 Mechanical Methods 19
1.2.3 Technological Limitations 22
1.3 Future Anemometry Technologies 23
1.3.1 Optical Methods 23
1.3.2 Acoustic Methods 24
1.3.3 Instrument Selection 26
1.4 Acoustic Anemometry on Mars 27
1.4.1 The Acoustic Environment on Mars 27
1.4.2 Transducer Selection 32

2. Capacitive Ultrasonic Transducer Modelling 35
2.1 Previous Work 35
2.2 Construction 36
2.3 Transmitter Modelling 37
2.4 Transducer Frequency Response 40
2.5 Losses to the Atmosphere 45
2.5.1 Absorption Losses 45
2.5.2 Impedance Mismatch Losses 46
2.5.3 Beam Spreading Losses 50
2.6 Receiver Modelling 52

3. Transducer Characterisation and Optimisation 55
3.1 Transducer Construction 55
3.2 Test Apparatus 58
3.3 Experimental Procedure 61
3.4 Backplane Roughness 62

3.5 Bias Voltage . . . 72
3.6 Membrane Thickness . . . 73
3.7 Backplane Diameter . . . 77
3.8 Low Pressure Frequency Response . . . 79
3.9 Optimum Transducer Parameters . . . 81

4. Instrument Testing and Optimisation . . . 83
4.1 Beam Pattern . . . 83
4.2 Transducer Separation . . . 85
4.3 Signal Shapes and Detection Methods . . . 86
4.4 Wind Tunnel Testing . . . 91
4.4.1 Wind Tunnel Specifications . . . 92
4.4.2 Procedure . . . 93
4.4.3 CFD Modelling and Transducer Shadowing . . . 94
4.4.4 Calibration . . . 103
4.4.5 Dust Survival . . . 111
4.5 Thermal Cycling . . . 115
4.6 Performance Assessment and Future Work . . . 116
4.6.1 Electronics . . . 117
4.6.2 Design Considerations . . . 118
4.6.3 Wind Tunnel Testing . . . 119
4.6.4 Dust . . . 120
4.6.5 Lander Accommodation . . . 121

5. Conclusion . . . 123

Appendix 127

A. Amplifier Frequency Response . . . 129

B. Electronics Circuit Diagram . . . 131

C. Wind Tunnel Schematics . . . 133

D. CFD Mesh . . . 135

LIST OF NOMENCLATURE

AC	Alternating Current
AWTS	Aarhus Wind Tunnel Simulator
DC	Direct Current
CAD	Computer Aided Design
CFD	Computational Fluid Dynamics
DSP	Digital Signal Processor
FPGA	Field-Programmable Gate Array
GCM	General Circulation Model
LDWT	Low Density Wind Tunnel
MEMS	MicroElectroMechanical System
MSL	Mars Science Laboratory
NASA	National Aeronautics and Space Administration
PBL	Planetary Boundary Layer
PEEK	PolyEther Ether Ketone
RH	Relative Humidity
RPM	Rotations Per Minute
SNR	Signal-to-Noise Ratio
TRL	Technology Readiness Level
VPP	Volts Peak-to-Peak

V_b	Bias Voltage
A	Backplane Area
d_m	Membrane Thickness
ρ_m	Membrane Density
m_m	Membrane Mass
T_m	Membrane Tension
d_a	Air Gap Thickness
p_a	Air Gap Pressure
V_a	Air Gap Volume
D_a	Air Gap Diameter
k	Gas Piston "Stiffness"
V_t	Transmitter Signal Voltage
V_r	Receiver Signal Voltage
p_t	Transmitted Acoustic Wave Pressure
p_r	Received Acoustic Wave Pressure
N	Transducer Natural Focus
f_0	Natural Oscillation Frequency
α	Attenuation Coefficient
Z	Acoustic Impedance
c	Speed of Sound
x_m	Membrane Deflection
x	Propagation Distance of Acoustic Pressure Wave
ω	Acoustic Angular Frequency
k	Acoustic Wavenumber
λ	Acoustic Wavelength

L	Transducer Separation
α_t	Acoustic Transmission Coefficient
θ	Absolute Beam Angle
U	Volume Velocity
j	Complex Frequency
z	Distance from Transmitting Transducer
r	Transducer Radius
Y	Atmospheric Signal Loss Coefficient
ρ	Atmospheric Density
b	Damping Factor
J_1	First order Bessel function
P	Air Pressure
f	Signal Frequency
D	Transducer Diameter

1. INTRODUCTION

1.1 The Martian Atmosphere

Mars is the most Earth-like planet in our solar system. Although it is roughly half as large as the Earth in diameter, it has a very similar axial tilt and experiences 24.7 hour days. As a result it experiences seasons like on Earth, though due to its elliptical orbit the seasons are not equally spaced out. The Northern winter is shorter and milder than the Southern one. One significant difference between the two planets are their atmospheres. Whilst the Earth's atmosphere is composed mainly of nitrogen and oxygen, Mars' is 95% carbon dioxide. The rest of the Martian atmosphere is comprised of 2.7% N_2, 1.6% Ar, 0.13% O_2 and variable amounts of water vapour. The resulting atmospheric density is much lower on Mars and the surface pressure is, on average, 170 times less than Earth. Whilst the weather on Earth is primarily driven by water, due to the abundance of its various forms, the radiative balance on Mars is driven by dust. This is significant because Mars has a very thin atmosphere (Figure 1.1) due to the lack of a global magnetosphere and atmospheric loss due to meteor impacts.

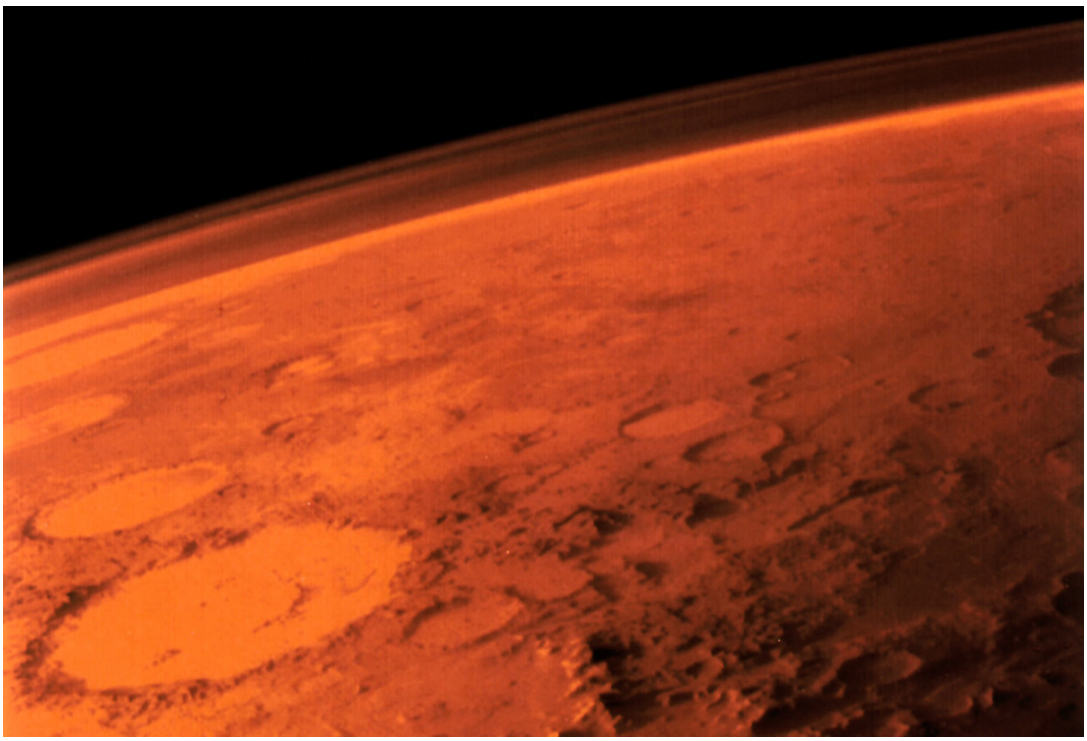


Fig. 1.1: Photograph from the Viking Orbiter showing the thin Martian atmosphere [1]

The lack of liquid water results in a low thermal inertia of the planet. As a result, there are substantial (~70 K) temperature differences between day and night due to solar radiation [2]. The intense solar surface heating can lead to vast dust storms in the summer months which engulf the entire planet, creating large variations in dust opacity and wind speeds in the planetary boundary layer. It is not known how these dust storms can grow to be so large or last for many months. Dust can make data collection on Mars difficult as dust storms can obscure satellite observations and coat the solar panels and instruments on surface landers. General Circulation Models (GCMs) are being developed to gain a better understanding of how the circulation is driven and how this will affect the Martian climate in the long term [3]. However, uncertainties in small scale process parametrisations can greatly affect large scale predictions, so more data are needed to test the validity of these small scale models and improve our understanding of the Martian atmosphere.

1.1.1 Atmospheric Scales

Changes in the Martian atmosphere occur over a wide range of distance and time scales, from very localised circulation patterns to ones affecting the whole atmosphere. These circulation patterns can be understood by considering three primary dynamics scales: global, mesoscale and planetary boundary layer (PBL). General Circulation Models are used to study the atmospheric circulation over the entire planet, and how it affects the Martian climate in the long-term. Mesoscale models predict circulation patterns over smaller, regional areas and PBL models are used to investigate the interactions between atmosphere and surface over small scales. These will each be explained in turn.

Global dynamics - The primary global circulation patterns alternate over diurnal and seasonal cycles and can affect the entire atmosphere. The diurnal and semi-diurnal changes in circulation patterns are primarily driven by solar heating. During the day when the Sun is directly overhead, hot air rises at the equator and moves at high altitudes towards the poles. This rising equatorial air is replaced by incoming cooler air at the surface moving towards the equator. As the Sun moves across the sky, away from the equator, the location of greatest heating also moves, resulting in a global meridional surface wind flowing from the cooler to the warmer hemisphere. Seasonal changes in circulation patterns are driven by the change in strength and latitude of the solar heating, leading to freezing and sublimation of carbon dioxide at the polar caps. During the winter months, up to a quarter of the atmosphere can precipitate out of the atmosphere into the winter polar cap, resulting in a meridional flow across the surface.

Mesoscale dynamics - The mesoscale covers distances ranging from one to several hundred kilometres. In these regions, the near-surface wind conditions are not only influenced by global circulation patterns but also more local features such as surface topography. Different terrain can create mesoscale circulation patterns directly, due to topography, or thermal inertia or albedo contrasts. The variation in local surface temperatures and heat fluxes on Mars can lead to very strong "slope" winds, since surfaces at different elevations are heated equally. They are therefore at the same temperature but different potential temperatures, resulting in convective instabilities. These slope winds are several times stronger on Mars than Earth due to low atmospheric thermal inertia and short radiative timescales [4].

PBL dynamics - The PBL is the region of the atmosphere closest to the surface in which the key interactions between the atmosphere and surface occur. It is of vital scientific importance since these interactions include exchanges of heat, momentum, dust and water. The largest gradients in temperature and wind speed are found in the PBL, which is highly variable due to low thermal inertia of the atmosphere. At night, the ground radiates the heat gained during the day and becomes cooler than the surrounding atmosphere (temperature inversion). The PBL is explored in more depth in the next Section, as it is where in-situ measurements are taken on Mars.

1.1.2 The Planetary Boundary Layer

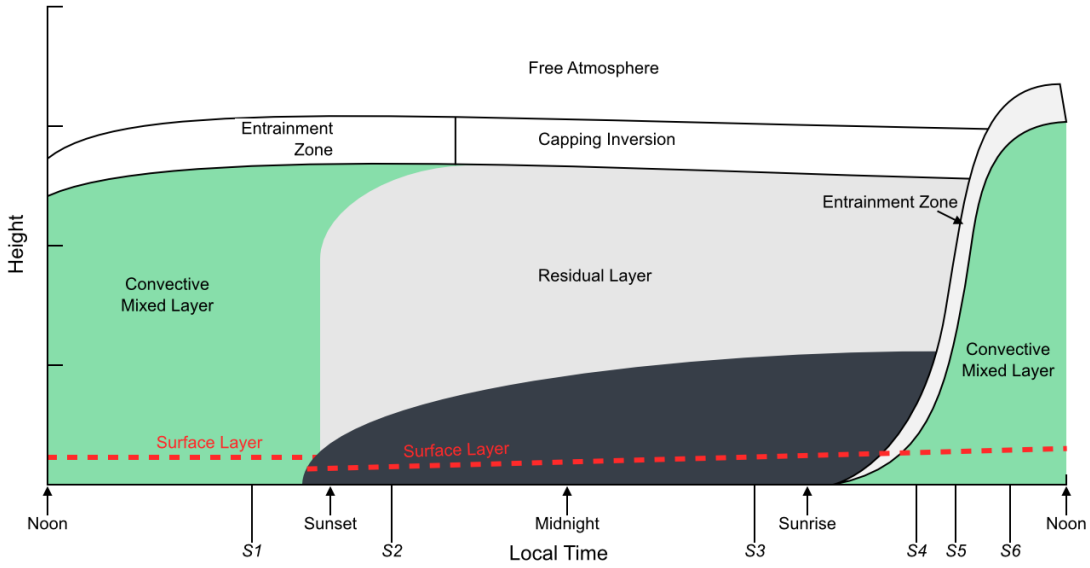


Fig. 1.2: Diurnal evolution of the Planetary Boundary Layer [5]

During the day, the PBL is split into three distinct regions: the laminar sub-layer (within a centimetre of the surface), the surface layer (up to hundreds of metres) and then the convective mixed layer (up to 5 km in height) [6]:

The **laminar sub-layer** is where the flow is laminar and the wind speeds are almost zero due to friction with the planetary surface [7]. Transport of volatiles takes place in this region through the processes of thermal conduction and molecular diffusion.

In the turbulent **surface layer**, large gradients in meteorological parameters are observed due to the significant parameter differences between surface and atmosphere. Close to the surface there is a significant shear as the wind speed must fall to zero whereas at the top of the layer, where it merges with the convective mixed layer, convective effects dominate any surface shear effects.

The **convective mixed layer** is where the potential temperature, wind speed and direction are approximately constant due to vertical convective mixing.
It exhibits an adiabatic lapse rate but this layer is still statically unstable as it is cooler than the turbulent layer below, so a column of air rising up from the turbulent layer would keep rising through the mixed layer. Above the mixed layer is the entrainment zone, where the free atmosphere is entrained into the underlying flow.

At night, the turbulent surface layer becomes statically stable with a subadiabatic (sinking) lapse rate. There is an increase in lapse rate from the surface layer to the convective mixed layer, which still exhibits the same adiabatic lapse rate due to uniform radiative cooling. The convectively mixed layer is now statically stable as no columns of air will rise from below.

Within the PBL, interactions between the surface and atmosphere are characterised by turbulence, dust and volatiles. The turbulent surface layer is of key importance as it is where in-situ measurements are taken. Here, how the wind speed varies with height is governed by the boundary layer similarity theory [8]. Heat and momentum fluxes in the PBL can be estimated using wind and temperature readings from multiple heights above the surface to obtain the wind and temperature profiles. These can also be calculated from readings taken at a single height and estimating the surface temperature (assuming a zero surface wind) [9]. The Monin-Obukhov similarity theory predicts mean temperatures and wind speeds as a function of height. Data collected so far has shown some consistency between the Mars and Earth boundary layers [10]; but

also some interesting differences, possibly due to the greater direct radiative heating of the Martian atmosphere [11]. However, there is a paucity of sufficiently high-resolution and frequency data for a proper analysis of the adapted model. Surface wind speeds and temperatures can be calculated from satellite observations but they suffer from poor temporal and spatial resolution. Full quantification of surface atmospheric conditions requires sensors on the ground. The meteorological data from Viking Lander 2 and Pathfinder have been compared with predictions from the boundary layer scaling laws [10], but only a limited comparison was possible as turbulent fluxes were not measured and only the Pathfinder instruments measured vertical temperature gradients [9]. The ideal data set for a full evaluation of similarity theory, without any estimates, would require concurrent measurements of wind, temperature, humidity and flux. New high-resolution Earth PBL models are being adapted for Mars [11] but more high-resolution measurements are required to validate these models, since the largest source of consistent meteorological data from the surface of Mars is the Viking landers in the 1970s. The Mars Pathfinder and Phoenix landers have since successfully deployed to the surface of Mars, but the wind speed data they provided was of limited scientific value due to calibration problems and inconsistent data rates. Mars Science Laboratory is currently operating on the Martian surface with a 3-D thermal wind sensor, but no results have yet been published after two years of operation. Thus new measurement technologies need to be chosen for future missions to provide more comprehensive and reliable datasets.

Better understanding of the PBL will lead to improved predictions of Martian weather and climate. However this is not just of purely scientific importance as all surface landers, as well as future manned missions, need to pass through and operate in this area. Of particular concern are turbulent vertical winds, especially for volatile transport and certain proposed landing systems such as parachutes [11]. Whilst we know there are large exchanges of volatiles between the surface and atmosphere in the PBL, we do not have data to quantify the fluxes and constrain the models. The processes responsible for dust transport and entrainment are not well understood, and can only be investigated by data gathered from in-situ measurements.

1.1.3 Turbulence

Turbulent fluid flow, such as smoke rising from a cigarette, is characterised by rapid spatial and temporal variations of parameters such as velocity and pressure. Turbulence is primarily quantified by three variables: the Reynolds, Richardson and Kolmogorov numbers [6]. The Reynolds number is the ratio of inertial forces to viscous forces. Since turbulent flows are dominated by inertial forces, they are represented by high Reynolds numbers. Another measure of turbulence, the Richardson number, is the ratio of potential to kinetic energy; a smaller number indicates stronger turbulence. The smallest turbulent eddies are characterised by the Kolmogorov scale, which at around 1 cm on Mars is 20 times more than on Earth [9]. As a result of the low atmospheric density, the Reynolds number is also lower on Mars and the inertial subrange of the turbulence variance shorter and of less importance than on Earth. The roughness Reynolds number, which characterises the interactions near the

surface, is also smaller on Mars resulting in more laminar flows than on Earth at comparable speeds. Due to the low atmospheric pressure, the thermal structure of the PBL is primarily driven by heat transfer between atmosphere and surface, creating strong turbulent temperature and wind variations during the day and stability at night. The steady night-time flows occur over large height intervals and with corresponding large Richardson numbers.

The vertical wind speeds associated with the smallest turbulent eddies are typically <1 ms^{-1} [11], so measuring these would require high frequency measurements of the order of 100 Hz (assuming ten measurements per eddy). However, the predicted turbulence spectra show that there should only be 2% as many eddies at 100 Hz compared to 0.1 Hz [10]. In fact, most of the energy transport in the surface layer is carried out by turbulent eddies ~10 m in size [12], and measuring these would require much lower measurement frequencies ~10 Hz.

1.1.4 Dust

As previously mentioned (Section 1.1.2), the primary driver of change in the atmosphere is dust. During dust storms, the atmospheric optical depth can increase by an order of magnitude or more. Since the dust is confined to the planet and atmosphere, this implies significant dust exchange between the surface and atmosphere. The mechanisms for exchange are driven by winds near the surface and can occur at high frequency, so require high spatial resolution and high-frequency wind speed data to quantify them. The two primary mechanisms for dust lifting from the surface of the planet are near-surface wind

stress and convective vortices (dust devils); though it is not known how much dust is entrained by each of the various mechanisms. As well as the high local wind speeds observed with dust devils, the large pressure gradient between the core and atmosphere are thought to be important in dust lifting [13].

The wind speeds on the Martian surface are too low to lift micron-sized dust particles directly into the atmosphere [14]. The threshold wind speed for dust lifting is dependent on several factors including dust density, particle size and inter-particle cohesion. Instead, it is believed that the primary mechanism for dust lifting on Mars is saltation, where larger particles ($\leq$20 μm diameter) are swept up from the surface and when they return to the surface, the impact suspends dust particles in the atmosphere [15]. The wind speed threshold at which saltation occurs on Mars is 1.5 ms^{-1} [16]. Saltation is thought to occur over distances of approximately 30 cm [15], so measuring saltation events would require data rates of around 50 Hz (for ten measurements per event). Thermophoresis, electrostatics and convective turbulence are other candidate mechanisms for dust injection. In thermophoresis, gas molecules trapped in the top surface layer are heated more than the atmosphere and surface dust particles are released through momentum transfer.



Fig. 1.3: Satellite photograph from the Mars Reconnaissance Orbiter showing a twelve mile high dust devil [17]

Dust devils (Figure 1.3) are convective vortices with low-pressure cores which allow for effective upwards advection of surface dust [18]. Whilst relatively common on Earth, they were not thought to occur on Mars due to the much lower atmospheric pressure. They have been detected on Mars using surface wind and pressure measurements, as well as satellite and lander imagery, and can stretch up to 10 km in height and 1 km in diameter. Additionally, the surface wind speeds associated with dust devils can range up to 60 ms^{-1}, which is significantly greater than the Martian saltation threshold [16]. Their existence on the surface of Mars has been confirmed but they are poorly understood due to a lack of high-frequency data. A typical dust devil, with a wind speed of 20 ms^{-1} and a diameter of 10 m [19], would require a measurement frequency of 20 Hz for ten measurements; or 60 Hz for the fastest wind speeds.

1.1.5 Volatiles

There are many possible sources, sinks and reservoirs for volatiles on Mars. Volatiles in the atmosphere can escape into space or be exchanged with the surface or polar caps [20]. Fluvial features on the Martian surface are evidence for flowing liquids; however it has not yet been determined whether this was liquid water, carbon dioxide, methane or another volatile. Carbon dioxide is the most abundant volatile on Mars, and is responsible for most of its atmospheric pressure and composition. It is distributed between the atmosphere and the polar ice caps, with seasonal variations in composition observed as the ice caps melt and freeze.

Other than Earth, Mars is the only planet where water has perhaps significantly altered surface features. Most of the water on Mars is in the form of polar ice with trace amounts of vapour in the atmosphere. The low pressure and temperature on Mars prevent any liquid water from pooling on the surface; though it has been shown that conditions favourable for small transient amounts of liquid water to form on the surface or sub-surface are possible [21]. The presence of water on Mars is of great importance for its role in the habitability of a planet. On Earth, the water cycle acts to reduce the diurnal temperature difference through evaporation and condensation but on Mars, the lack of significant amounts of water leads to large diurnal temperature variations.

Direct vertical flux measurements of volatiles through the boundary layer have never been attempted on Mars, but such data could be used to quantify the exchanges of volatiles between the surface and atmosphere. The horizontal

transport of water from the surface has been modelled experimentally [22], and this data indicates that transport occurs over a distance of ~50 cm at wind speeds ~1 ms^{-1}. Whilst the exact vertical volatile fluxes have not yet been modelled, they will likely be <1 ms^{-1} and therefore require high spatial and temporal resolution wind speed data. Measurements of these transport fluxes would need to occur at 20 Hz, which is in line with the 10 Hz of the proposed MWX lander [23].

1.1.6 Wind Speeds on Mars

Science Objective	Weather	Turbulence Spectra	Dust Devils	Dust Saltation	Volatiles
Wind Vector	2-D	3-D	3-D	3-D	3-D
Wind Speed	30 ms^{-1}	10 ms^{-1}	20 ms^{-1}	1.5 ms^{-1}	1 ms^{-1}
Data Frequency	0.001 Hz	10 Hz	20 Hz	50 Hz	20 Hz
Spatial Resolution	1000 m	10 m	10 m	30 cm	50 cm
Co-located Data	p, T	N/A	p, T, dust	dust	Volatiles
Prior Wind Data	Viking 2-D, 1 Hz	Viking Pathfinder 2-D, 1 Hz	Viking Pathfinder 2-D, 1 Hz	Viking Pathfinder 2-D, 1 Hz	No

Tab. 1.1: Summary of scientific phenomena of interest and associated typical measurements. References are contained in each relevant Section

Table 1.1 shows a variety of the phenomena discussed in the previous three subsections; along with their typical associated measurement ranges. The measured horizontal wind speeds on Mars have been found to fit a Weibull Distribution [24]. This function is defined by two parameters: the scale speed c, and dimensionless shape parameter k. An example distribution for a windy day on Mars, using data taken from the Viking 1 lander, is shown in Figure 1.4.

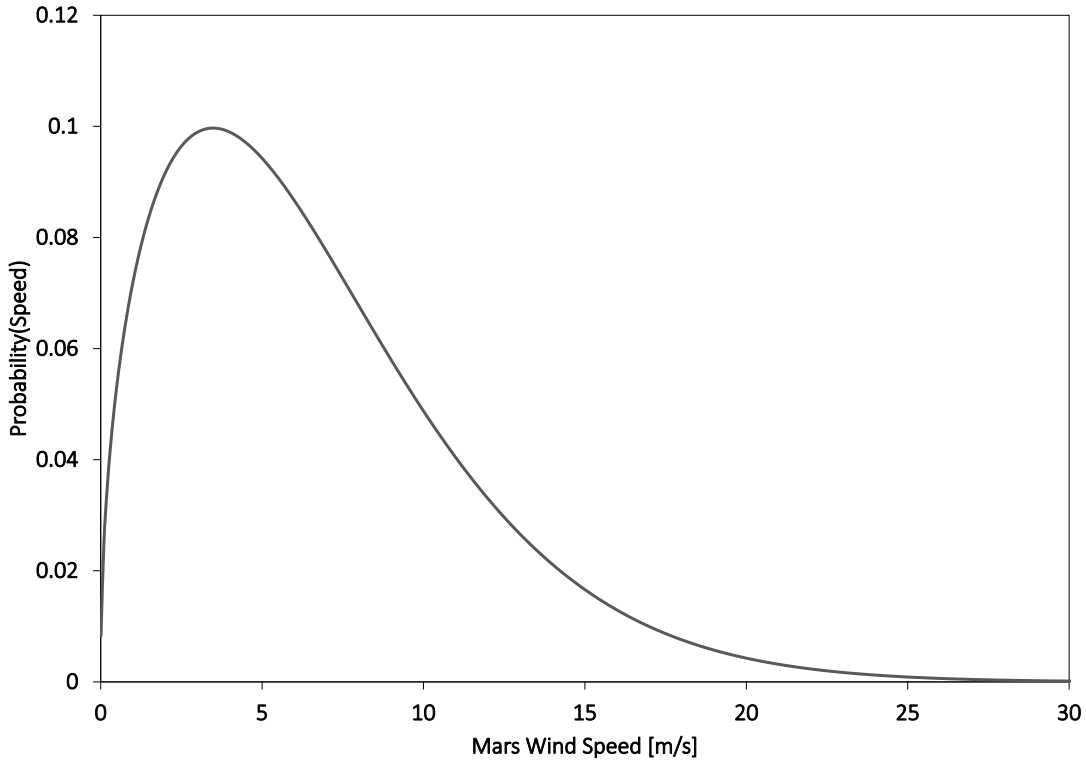


Fig. 1.4: Probability distribution for surface wind speeds on Mars (using k=1.48, c=7.45 values from Lorentz [24])

Figure 1.4 shows that, even on a relatively windy day on Mars, half of the recorded wind speeds would be <6 ms^{-1} and 80% would be <10 ms^{-1}. The maximum surface wind speed measured to date was 25.9 ms^{-1} by the Viking 1 lander [25].

1.2 Past Anemometry Techniques

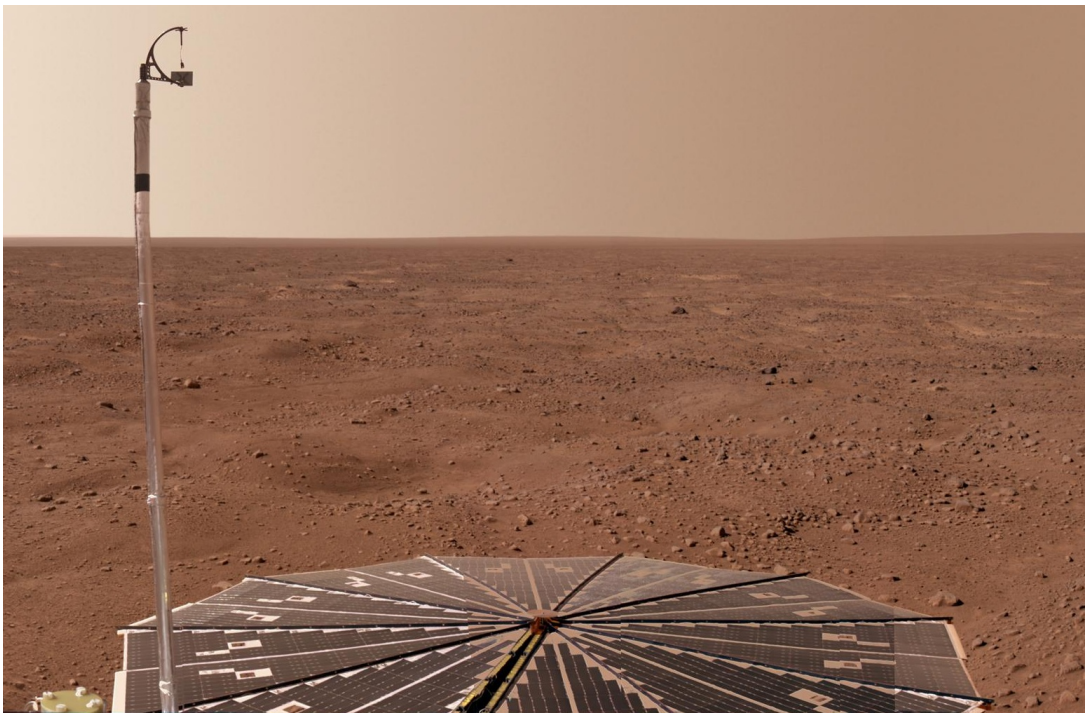


Fig. 1.5: The Phoenix Telltale sensor on Mars [26]

There are a wide range of anemometry techniques used on Earth, but since the Martian and Earth atmospheres are so different, choosing which techniques can be adapted to work on the Martian surface requires careful consideration. Previous surface missions have used thermal and mechanical wind sensing technologies.

1.2.1 Thermal Methods

These rely on the principle of convection, since materials lose heat to the atmosphere and the rate of convective heat loss is related to the wind speed. Hot wire and hot film sensors, which operate on the same principles, have been used successfully on previous missions. A wire/film is heated by passing a current through it, and the temperature of the wire obtained by measuring its resistance. The temperature of the wire/film varies with wind speed due to convection, and comparing this temperature with an independent ambient

temperature reading allows a wind speed to be determined. Since the amount of convection is proportional to the square root of the wind speed [27], thermal anemometers are capable of measuring a wide range of velocities. Though these are generally a robust, low-mass method for wind speed sensing on Mars, they require accurate individual calibrations and are prone to erroneous results caused by varying ambient temperatures and other thermal loads.

The Viking landers (1975-1982) were capable of measuring pressure, temperature and wind velocity. Viking 2 reported wind data for 1050 sols whereas Viking 1 only gave 375 sols of wind data due to failure of one of its two hot film sensors [28]. The onboard wind sensors consisted of two orthogonal hot wires and a reference temperature sensor; plus a quadrant sensor for independent wind direction [29]. They were capable of measuring speeds in the range 2-150 ms^{-1}, with an absolute accuracy of $\pm 10\%$ in wind speed and direction, at a maximum frequency of 1 Hz. The onboard ambient temperature sensor had an accuracy of 1.5 K, but operational temperature and wind measurements suffered from thermal contamination due to heat from the craft's radioisotope thermal generators. Mission data suggested the wind patterns were predominantly the result of pressure gradients due to local topographical slopes and coupling with large-scale winds [25].

The Mars Pathfinder (1996-1997) 6-wire wind sensors were specified to measure wind speed with an absolute accuracy of <1 ms^{-1} in wind speed up to 20 ms^{-1} and <4 ms^{-1} above that; and $\pm 10\%$ in wind direction at a maximum frequency of 0.25 Hz [32]. The onboard ambient temperature sensor had an accuracy of

1 K. Pathfinder gathered 83 sols of wind data but few absolute wind values were ever published from the mission due to unsuccessful calibration attempts [33]. These difficulties were primarily due to the low overheat of the wires above the ambient temperature and uncertainties in the local air temperature due to the thermal boundary layer of the cylinder. Thermal anemometers are prone to technical calibration issues as the technology is sensitive to systematic errors due to varying pressure, air temperature, gas composition and their own overheating.

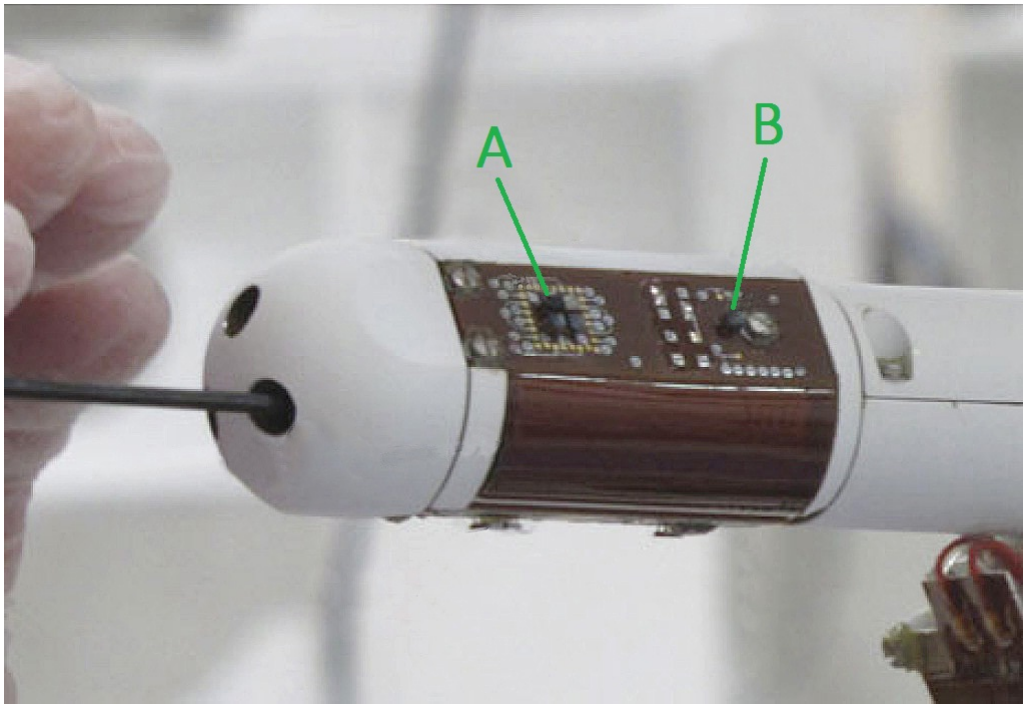


Fig. 1.6: Image of one of the damaged MSL boards (before launch), clearly showing the four heated die (A) and reference temperature die (B) [34]

Mars Science Laboratory (MSL, 2012-present) carries two thermal wind sensors which, for the first time, should be able to measure the vertical wind component as well as the previously measured horizontal components. The instrument is comprised of two identical booms 120° apart. The two booms comprise three equally-spaced transducer boards around a cylindrical core, each capable of

measuring 2-D wind speed. Therefore the set of three transducer boards on a single boom returns a 3-D wind vector. Two booms provide redundancy and ability to measure different incident wind directions without interference from the central mounting boom. The instrument was designed this way as, unlike previous Martian anemometers, they could not be housed on the end of a boom away from the landed craft. Thus the wind data are greatly affected by the fluid flow around the rover body and protruding masts. The transducer boards house four hot die and one cold die, where each die is constructed from titanium thin-film resistors (Figure 1.6). The cold die is used to measure the ambient temperature and the hot dies are kept at a constant temperature above ambient to measure the two-dimensional wind speed. The three-dimensional wind speed and direction are calculated using the convolution of the wind data from the six transducer boards to a specified accuracy of <1 ms^{-1} in wind speed up to 70 ms^{-1} and $\pm 30\%$ in wind direction [35]. As is common for flight thermal anemometers, the qualification models were calibrated instead of the flight models [36]. However, during landing some of the wind sensor wires on the exposed circuit boards were damaged, possibly by small rocks expelled from the surface by the propulsion system. This resulted in two of the three boards on one of the wind sensor booms giving erroneous saturated high or low readings [37]. However the functioning boom wind data, in conjunction with other instruments, has already confirmed the existence of vortices in Gale Crater [38]. Convective vortices were not thought to occur in that region as no tracks have ever been observed there.

1.2.2 Mechanical Methods

These derive the wind speed from the force of the wind on an object, for example wind socks and cup anemometers. Though these are relatively simple to manufacture, they are difficult to calibrate and are prone to damage from launch and landing due to their moving parts. For example, the Phoenix Telltale failed during vibration testing just before scheduled delivery in May 2006. Additionally, the low atmospheric pressures on Mars make it difficult to calibrate the sensors and measure a wide range of wind speeds. This is because the dynamic pressure is proportional to the square of the velocity, so it is a challenge to design a single device capable of measuring a wide range of velocities.



Fig. 1.7: The three conical Pathfinder wind socks on the surface of Mars (right) [39]

Mars Pathfinder included three wind socks at different heights above the surface, whose orientations were observed by the lander camera (Figure 4). Each one was a 10 cm long hollow aluminium cone on a pivot with a steel counterweight. Few absolute wind values were ever published from the Pathfinder mission due to calibration problems [33]. However, the wind socks did provide limited data about boundary layer profiles for the first time. The wind socks were sensitive to wind speeds 5-30 ms^{-1}, but most of the measured deflections were too small to reliably infer a wind speed from the calibration data; and were discarded [40].

The Phoenix (2007-2008) Telltale sensor (Figure 1.5) consisted of a 10 mg Kapton cylinder suspended on a bundle of Kevlar fibres above an angled mirror [41]. Originally, a hot-wire wind sensor had been proposed for the mission, but was deselected from the payload due to mass and cost constraints [42]. The Telltale was included late in the mission development stage to provide approximate wind speed and direction with no additional power or direct data transmission requirements. Data collection involved photographing the suspended mass to determine wind speed and direction. However operational problems led to inconsistent data rates; between zero and 193 values per sol with an average of 49 [43]. The Phoenix data showed an average wind speed of 5 ms^{-1} and a maximum of 16 ms^{-1}, as well as diurnal variations in both wind speed and direction. The Phoenix Telltale wind sensor was never attributed any resolution or accuracy figures as these were difficult to provide [44]. However, the science requirement stipulated that the device be capable of measuring winds in the range 2-5 ms^{-1} with a 20% accuracy and 5-10 ms^{-1} with a 40% accuracy. Above this, the Telltale would always be horizontal so no accurate

wind speed information could be obtained. In addition to the wind speed and direction, it was capable of measuring the wind turbulence since more turbulent winds would result in more blurred images. Whilst operational, it had a maximum measurement frequency of 0.002 Hz due to the large amount of data required to take an image of the position of the suspended mass. The onboard temperature sensor had an accuracy of 1 K and the temperature data, although contaminated by the warm craft, was used to estimate heat fluxes between the atmosphere and surface [45]. The estimations had corresponding large error bars; which could have been reduced significantly if the vertical wind speeds had been directly measured.

1.2.3 Technological Limitations

Mission	Sensor	Accuracy, Range, (Vector)	Data Frequency (Hz)	Data Length (sols)	Operational Issues
Viking 1 [28]	2-wire, film	±10% 2-150 ms^{-1} (±10%)	1	375	Thermal contamination, sensor failure
Viking 2 [28]	2-wire, film	±10% 2-150 ms^{-1} (±10%)	1	1050	Thermal contamination
Pathfinder [33]	6-wire	±1 ms^{-1} <20 ms^{-1} ±4 ms^{-1} >20 ms^{-1} (±10%)	0.25	83	Unsuccessful calibration attempts
Pathfinder [40]	Windsocks	±1 ms^{-1} 5-30 ms^{-1}	10^{-6}	49	Calibration problems
Phoenix [44]	Telltale	±20% 2-5 ms^{-1} ±40% 5-10 ms^{-1}	0.002	151	Calibration problems
MSL [35]	Two booms, 6 hot die boards, 3-D	±1 ms^{-1} <70 ms^{-1} (±30%)	1	N/A	One boom damaged during landing

Tab. 1.2: Specifications of wind sensors which have been successfully deployed on Mars

Comparing this data with Table 1.1, it is clear that the technologies used to date, whilst adequate for basic meteorology, have been inadequate for measuring many of the aeolian phenomena of interest. High-frequency and high resolution data are required to measure the small-scale processes and vertical winds. However thermal and mechanical methods are not suitable candidates.

1.3 Future Anemometry Technologies

The previous Section highlighted the need for new technologies to be implemented to achieve a more comprehensive understanding of certain wind-related phenomena; such as interactions between the ground and atmosphere and other small-scale processes. The two most promising next-generation designs are based around optical and acoustic anemometry techniques.

1.3.1 Optical Methods

Laser Doppler anemometry is used on Earth for remote, non-invasive flow measurements. Two coherent laser beams of slightly different frequencies are focussed onto a point inside the flowing fluid. The light is back-scattered off particles suspended in the fluid flow and the Doppler-shifted frequency of the scattered light intensity can be used to determine the speed of the particle perpendicular to the beams. The beams need to be different frequencies as, if they are of the same frequency, the instrument cannot distinguish a zero velocity or flow direction. These measurements are highly accurate and non-invasive but may represent particle velocity rather than true fluid velocity. In addition, the sensors are relatively large and require complicated electronic processing. If they were successfully miniaturised, they could be the most accurate method of wind sensing on Mars. They are not frequently used for turbulence studies on Earth as they require seeding particles for the light to be reflected from; whereas on Mars, dust in the atmosphere would act as the seeding particles. Current research is being carried out in developing such devices for use on Mars [46], but these sensors are not without their drawbacks. The measurements require dust

as a seeding particle, and the accuracy of the wind speed is dependent on the amount of dust. Additionally, the speed of the seeding particles may not be the same as the underlying wind speed and large amounts of dust deposition, such as during dust storms, could obscure the laser beams.

1.3.2 Acoustic Methods

Acoustic ultrasonic transducers are very popular on Earth for turbulence measurements due to their full-range accuracy and high measurement frequency. This method relies on the fact that acoustic waves travel inside a fluid medium. Therefore if the medium is moving, there will be a difference between sending and receiving a wave compared to if the medium were stationary. This difference can be measured in the frequency or time domain, as discussed below.

For frequency-domain measurements, an acoustic signal is continually transmitted and the phase shift of the received signal allows the wind speed to be calculated. This was the method proposed for the Beagle 2 ultrasonic sensor [47], but is not without potential operational problems. The constant signal frequency must be chosen to be such that the maximum phase difference is much less than one wavelength. On Mars, for a maximum wind speed of 60 ms^{-1}, this dictates a signal frequency of approximately 3 kHz; at which there would be significant losses due to beam spreading (Section 1.4.1). In addition to this method being high-power, as the transducers are constantly transmitting, the transmitter and receiver electronics must be very carefully isolated to eliminate cross-talk; which would compromise the accuracy of the wind speed measurement.

Measuring the "time of flight" of an acoustic signal between two opposite transducers allows a wind speed to be calculated directly, and cross-talk is not a problem as the sent and received signals occur at different times. Since the transducers are not transmitting constantly, less power is required. Working in the time-domain allows the use of powerful signal detection techniques which can be used at much lower signal-to-noise ratio (SNR), such as pulse compression.

Frequency-domain measurements were proposed for the Beagle 2 anemometer as narrow-band transducers were used in conjunction with a small separation, and both factors would have prevented time-domain measurements. However, time-domain measurements are preferable due to their higher operating frequency, lower power requirements and the option to use powerful signal detection techniques. To obtain these measurements, two transducers are positioned opposite each other and the time of flight for the acoustic wave measured over both directions. Since the transducer separation is known, the difference in transit times can be used to calculate the wind velocity component parallel to the sensor axis, and the speed of sound can be determined from the average transit time. As the speed of sound on Mars is only a function of temperature, and these measurements are immune to errors from thermal loads, ultrasonic transducers can also be used as high-frequency temperature sensors. Three-dimensional measurements are possible using three pairs of mutually-orthogonal transducers. Transducer separation is key; not only because this technique is insensitive to turbulent cells smaller than the separation, but also because it dictates the necessary measurement frequency and, therefore, wind speed resolution. This is particularly important for measuring vertical

wind speeds, which have more stringent accuracy requirements and tend to dictate the operating frequency of the instrument.

1.3.3 Instrument Selection

Science Requirements	Instrument Requirements	Thermal Measurement	Optical Measurement	Acoustic Measurement
Weather	2-D vector	✓	✓	✓
	1Hz	✓	✓	✓
	ms^{-1} accuracy	✓	✓	✓
Turbulence	3-D vector	✓	✓	✓
	10Hz		✓	✓
	cms^{-1} accuracy		✓	✓
Dust Devils	3-D vector	✓	✓	✓
	20Hz		✓	✓
	cms^{-1} accuracy		✓	✓
	Temperature	✓		✓
Saltation	3-D vector	✓	✓	✓
	50Hz		✓	✓
	mms^{-1} accuracy		✓	✓
Volatiles	3-D vector	✓	✓	✓
	20Hz		✓	✓
	mms^{-1} accuracy		✓	✓

Tab. 1.3: Traceability matrix for instrument selection, including which instruments are capable of measuring each phenomenon

Ultrasonic transducers are very promising for use on Mars due to their high measurement frequency, accuracy, immunity to drift and 3-D wind vector potential. In addition to just measuring wind speed, the high-frequency data can be used to calculate the air temperature, which is important to investigate heat fluxes. Their data would place important constraints on current and future PBL models as well as characterise important aeolian processes such as dust lifting

and water cycles. They would be able to resolve individual turbulence patterns and allow investigations into the transport of volatiles in individual eddies.

However, whilst acoustic anemometers are a promising technology for high quality wind speed data from the Martian surface, their accuracy is determined by the signal-to-noise ratio. Robust measurements require that the signal is reliably distinguishable from the noise, so the anemometer first needs to be coupled to operate in the Martian atmosphere.

1.4 Acoustic Anemometry on Mars

Whilst acoustic transducers are in common usage on Earth for a variety of purposes, including non-destructive testing and acoustic anemometry, it is not trivial to adapt an Earth-optimised acoustic transducer to operate on Mars since the two atmospheres are very different.

1.4.1 The Acoustic Environment on Mars

It is much more difficult for acoustic waves to propagate through the Martian atmosphere due to greater attenuation and impedance losses.

Attenuation

In fluids there is acoustic attenuation due to heat conduction, viscosity, diffusion and molecular relaxation. Whilst attenuation increases with frequency on both Earth and Mars, the attenuation on Mars is several orders of magnitude greater than on Earth (Figure 1.8).

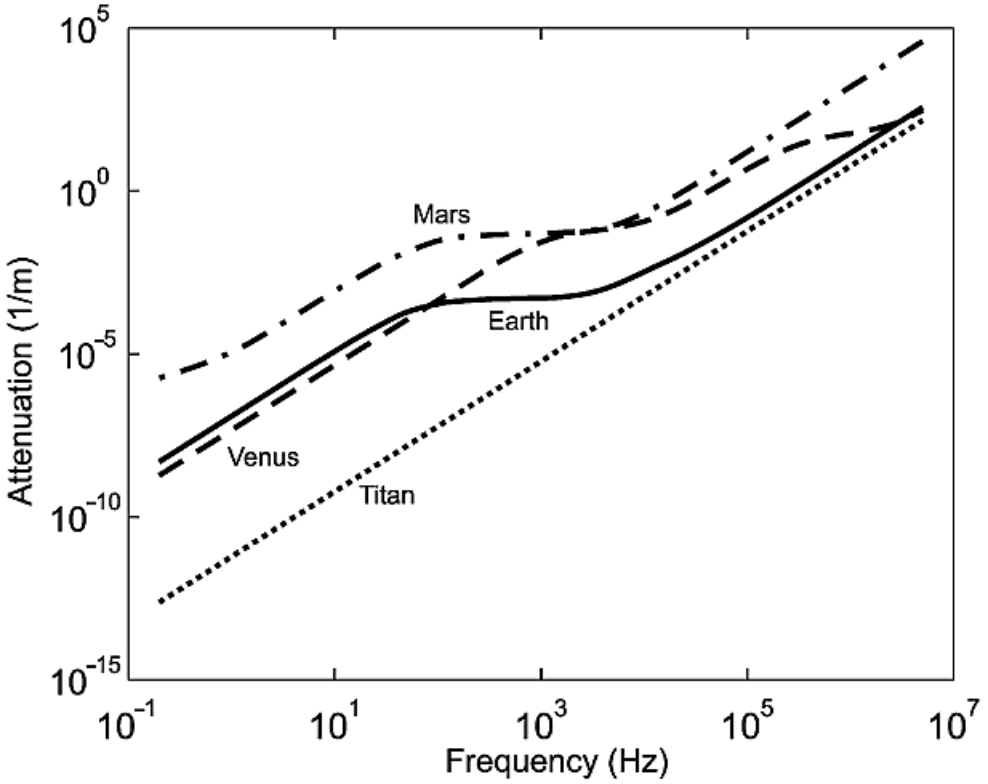


Fig. 1.8: Variation of atmospheric attenuation with frequency at surface pressure [48]

The attenuation coefficient is dependent on atmospheric composition, pressure, temperature and relative humidity (RH). The high acoustic attenuation on the Martian surface can be attributed to the low temperature and carbon-rich atmosphere. Attenuation increases with increasing pressures and varies with relative humidity depending on the temperature [50].

Minimising the atmospheric attenuation losses, therefore, requires that the transducers be close together and operate at as low a frequency as possible.

Acoustic Impedance

The characteristic acoustic impedance of a medium is the ratio of pressure to flow per unit area. For a sound wave travelling through a medium, the acoustic impedance Z is an intrinsic property of the material and is given by the product

of the density ρ and speed of sound c:

$$Z = \rho c$$

The impedances of the transducers and atmosphere should be as close as possible as wherever there are impedance mismatches, a significant proportion of the signal is lost to reflection. The acoustic impedance of the atmosphere at the surface is approximately 407 $\mathrm{kgm^{-2}s}$ on Earth and 4 $\mathrm{kgm^{-2}s}$ on Mars. Therefore an acoustic instrument designed for use on Earth may not function on Mars at all, depending on the transducer acoustic impedance. This large difference in acoustic impedances is primarily due to different gas densities in the medium and corresponding different atmospheric pressures. The speed of sound varies with temperature and gas composition, and is independent of pressure. On Mars, the speed of sound is lower than Earth due to the higher molecular weight of the atmosphere and generally lower observed temperatures. The acoustic impedance of the Martian atmosphere varies very slightly with frequency since the speed of sound on Mars is also frequency-dependent (Figure 1.9).

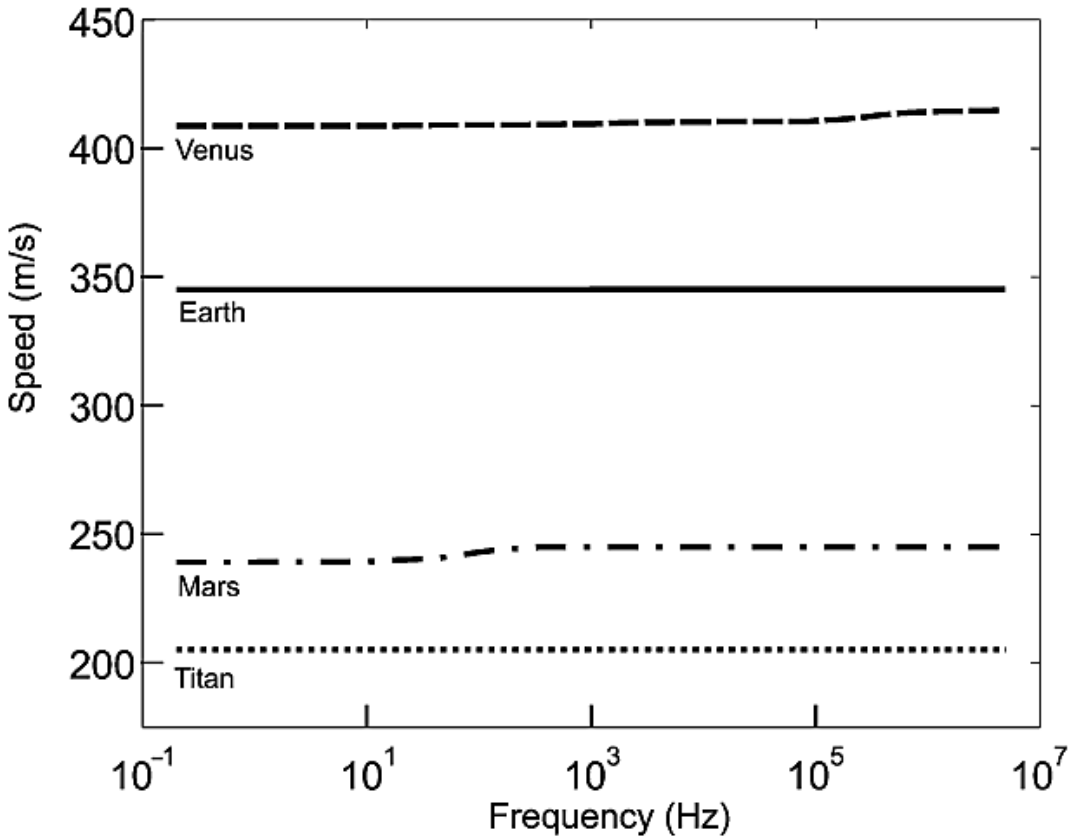


Fig. 1.9: Variation of the speed of sound (impedance) on Mars [48]

This change in speed of sound with frequency results in a small (2%) change in acoustic impedance of the Martian atmosphere.

Theoretically, there are less signal losses in CO_2 than in air at the same pressure. The lower speed of sound in CO_2 results in reduced losses due to the divergence of the acoustic wave (Section 2.5.3) and also a higher acoustic impedance of the gas; resulting in lower impedance losses. Whilst attenuation is much greater in CO_2 (40 m^{-1}) than in air (0.26 m^{-1}) at ultrasonic frequencies [49], the overall effect is that received amplitudes should be greater in CO_2 than air at the same pressure.

Frequency-dependence of received signals

Additionally, acoustic signals are lost to the atmosphere through beam spreading since not all energy is transferred in a straight line through the medium. A good analogy is to think of two balls hitting each other at an off-centre angle; they will recoil in different directions away from the axis of zero initial momentum. The amount of beam spreading is frequency-dependent since the beam pattern is relative to the acoustic wavelength. Higher frequencies diverge less, and so result in larger received intensities (Section 2.5.3) . However this behaviour is opposite to the frequency response of the attenuation losses, so there is a trade-off in operating frequency. Incorporating the major frequency-dependent sources of signal loss to the atmosphere allows us to determine the optimum acoustic operating frequency on the Martian surface (Figure 1.10).

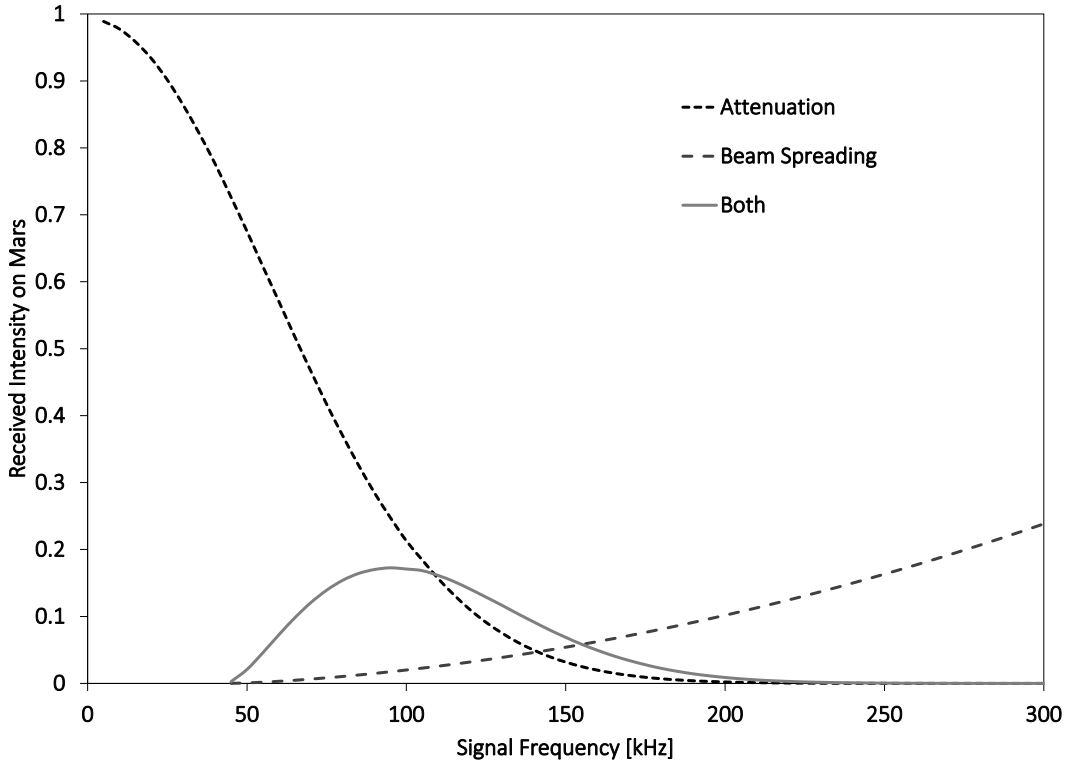


Fig. 1.10: Optimum signal frequency for maximum acoustic transmission on the Martian surface (for two identical 10 mm diameter transducers placed 10 cm apart)

This gives an optimum signal frequency of 85 kHz on Mars using 10 mm diameter transducers placed 10 cm apart, which agrees with the ~100 kHz value calculated by Banfield [51]. Note that the wind speed resolution is dependent on the sampling frequency of the sent and received signals, but not the signal frequency.

Therefore whilst acoustic transducers are a promising anemometry technique on Mars, operating frequency selection is vital for maximising signal transfer in Martian atmospheric conditions. An incorrect value can cause significant losses due to attenuation, impedance mismatch and beam spreading losses. These are discussed further in Section 2.5.3.

1.4.2 Transducer Selection

Since the atmospheres of Earth and Mars are so different, care must be taken in selecting transducers for generating and receiving acoustic signals on Mars. Section 1.4.1 provided some requirements for using acoustic transducers on the Martian surface; namely that they be sensitive, low frequency (<100 kHz) and have an acoustic impedance approaching that of the Martian atmosphere (4 $\mathrm{kgm^{-2}s}$).

The most widely-used ultrasonic transducers for acoustic anemometry on Earth are piezo-electric driven. The piezo-electric effect describes that certain materials deform in a specific, predictable manner when an external voltage is applied. If an oscillating voltage is applied to the crystal, it will also oscillate. In piezo-electric transducers, the crystal is connected to a moveable disc which then

also oscillates. However, they have large impedances (10^7 kgm^{-2}s [54]) and so would be impractical for use on Mars due to the significant impedance mismatch with the atmosphere. In addition, they have narrow frequency responses due to the natural frequencies of the crystals used, and exhibit greatly reduced sensitivities away from the resonant frequency.

Capacitive transducers are a much more suitable choice for realising acoustic anemometry on the Martian surface. Principally they are much more sensitive than piezo devices and have significantly lower impedances (~10^3 kgm^{-2}s [54]), and therefore lower impedance losses to the Martian atmosphere. They also exhibit much wider bandwidths than piezo-electric transducers and can be successfully driven at any frequency, not just their natural frequency. This allows complex signal shapes to be transmitted using both frequency and amplitude modulation; aiding in signal detection at low signal-to-noise ratios via advanced techniques such as pulse compression. Capacitive transducers are constructed of thin metallised polymer films over conductive surfaces. The microscopic features on the conductive surfaces trap small pockets of gas and allow the film to oscillate when a varying voltage is applied. Different methods for contouring the surface of the transducer, including traditional machining techniques and more advanced micro-mechanical ones, affect its operating characteristics. Capacitive transducers with micro-machined backplanes are currently being developed for future Mars missions [54]; however the design includes classified commercial information.

It has been determined that more accurate and reliable anemometers are required on the Martian surface, and that acoustic anemometers offer a promising alternative to previous instruments. However, their viability depends on the received signal amplitude and therefore achieving low acoustic impedance to enable efficient generation and reception of acoustic signals in the rarefied Martian atmosphere. Capacitive transducers appear to offer a solution in that they have comparably low impedances and can operate at wide frequency ranges; opening up the possibility of using advanced signal detection techniques. Chapter 2 will detail the physical principles behind the operation of these devices and, in particular, which parameters should theoretically have the greatest impact on received signal amplitudes. These theoretical predictions will be experimentally verified in Chapter 3, and Chapter 4 will investigate how the device performs measuring wind speeds under simulated Martian conditions and using different signal detection methods.

2. CAPACITIVE ULTRASONIC TRANSDUCER MODELLING

This Chapter will detail the entire process of acoustic generation, propagation and sensing in the proposed instrument. The transmitting transducers (Section 2.3) turn electrical signals into longitudinal acoustic waves; which are attenuated and dispersed by the transmission medium (Section 2.5). The receiving transducers (Section 2.6) turn received acoustic waves into a varying capacitance, which is then amplified by the electronics. Since operating frequency is so crucial in determining device operation under Martian conditions, Section 2.4 describes how device construction affects its peak frequency response. After an analytical framework for modelling transducer performance is developed in this Chapter, experimental validation will be presented in Chapter 3.

2.1 Previous Work

Capacitive transducers rely on the same principles as condenser microphones, which were invented in 1916 by E.C. Wente. Since then, research has been carried out on characterising transducer performance [52] and optimisation for signal transmission through different materials [53]. They have also been shown to work at low gas pressures and in carbon dioxide atmospheres, but there is more work to be done to optimise the transducers for operation on the Martian surface [54]. There has also been research on the different backplane manufacturing techniques including machining and etching [55]. Thin-film

capacitive transducers were chosen for further testing as Martian anemometers for their low impedance, high sensitivity and wide frequency response; which allows for time-domain signal processing.

Currently there is at least one other group interested in developing acoustic anemometers for use on the Martian surface, using silicon micro-machined (MEMS) backplanes and thin metallised films [54]. The goal of this research is to develop, characterise and optimise capacitive thin-film transducers for use on the Martian surface. The sensors developed for this project were produced using conventional machining techniques and materials, and use a thin metallised film as the vibrating layer.

2.2 Construction

The transducers consist of a metallised polymer film of thickness d_m laid on top of a contoured metal backplane. The metal layer is drawn towards the backplane by a DC bias voltage V_b. In effect, they are two parallel plates separated by an insulator; and so behave like a capacitor. The backplane is contoured to allow small trapped air pockets to form and allow the film to oscillate; a varying signal $V_t(t)$ is coupled on top of the DC bias to oscillate the film. Different fabrication methods allow various roughnesses, and therefore air gap sizes, to be investigated. Micro-machined etching processes can produce roughnesses of the order of tens of microns [64]; whereas feature sizes on the order of hundreds of microns can be manufactured using standard machining processes on a lathe [61].

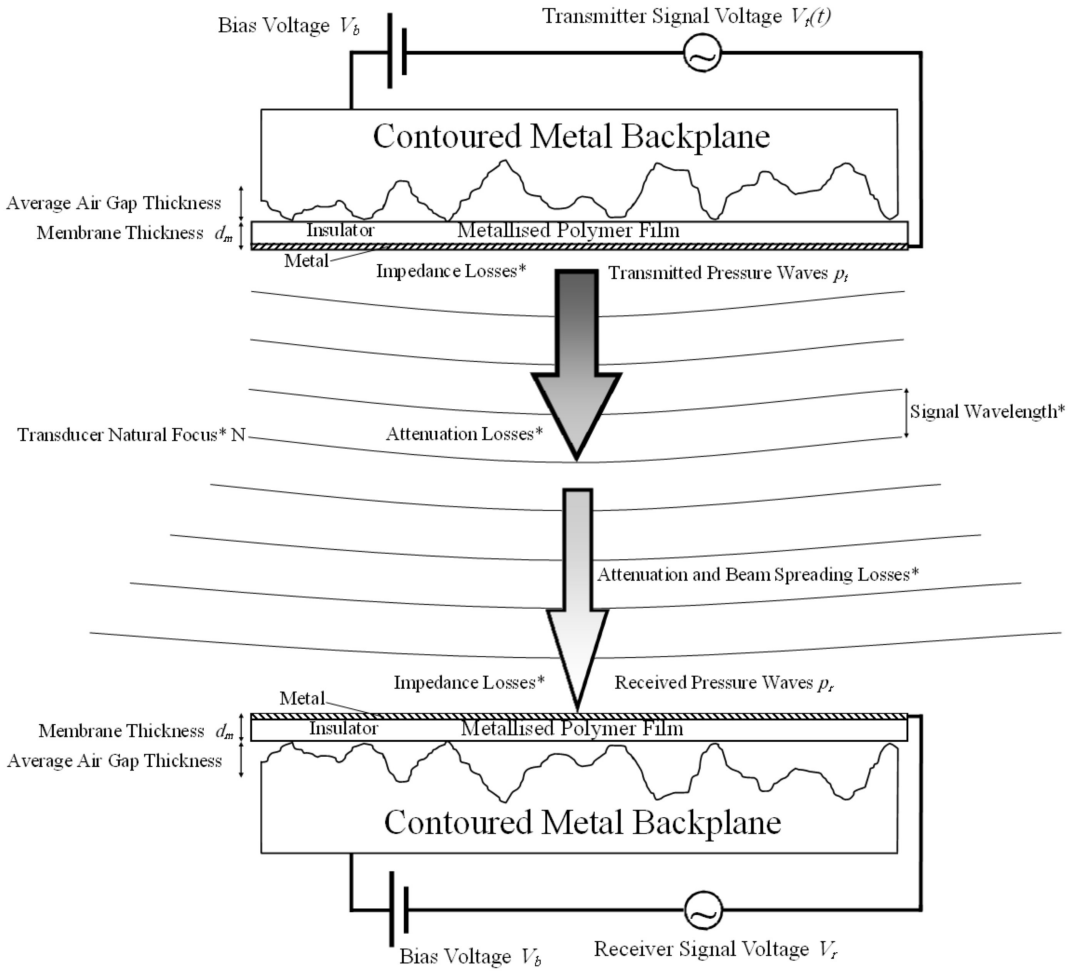


Fig. 2.1: Physical representation of the system (not to scale). Frequency-dependent parameters are denoted by an asterisk.

Either transducer can be used as a transmitter or receiver as they are identical. The transducers are primarily characterised by their sensitivity and frequency response [61].

2.3 Transmitter Modelling

The transmitter can be modelled as a damped forced oscillator where the varying signal voltage drives the motion of the metallised film; which is also constrained by damping from friction and the effect of the gas trapped behind the film. This is modelled as a mass m_m oscillating on a spring of stiffness k (Figure 2.2).

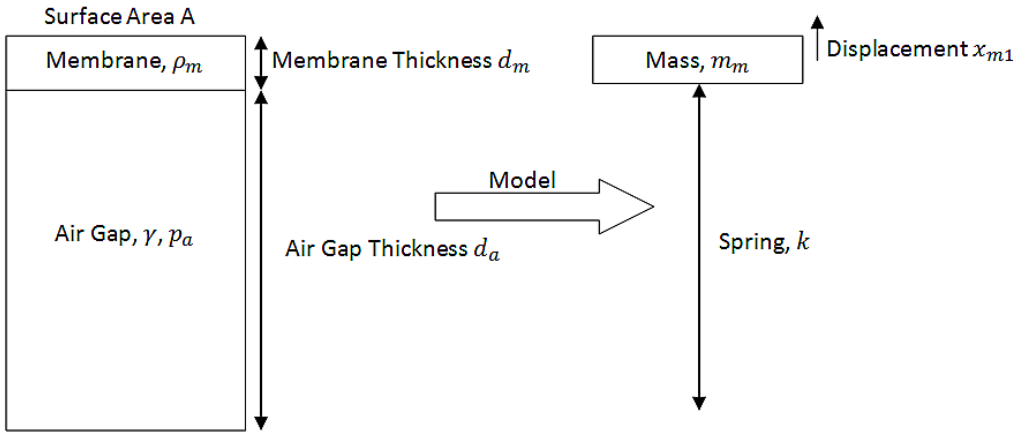


Fig. 2.2: Transducer model

The transmitting transducer can be thought of as two capacitors in series, representing the air gap and metallised film. The total capacitance of the system is:

$$\frac{1}{C} = \frac{(d_a + x_{m1})}{\varepsilon_0 A} + \frac{d_m}{\varepsilon_0 \varepsilon_r A} \tag{2.1}$$

$$C = \frac{1}{\frac{(d_a+x_{m1})}{\varepsilon_0 A} + \frac{d_m}{\varepsilon_0 \varepsilon_r A}} \tag{2.2}$$

The energy stored in the capacitor is given by

$$E = -\frac{1}{2}CV^2 = \frac{1}{2}\frac{1}{\frac{(d_a+x_{m1})}{\varepsilon_0 A} + \frac{d_m}{\varepsilon_0 \varepsilon_r A}}V^2 \tag{2.3}$$

Which gives us an expression for the driving force on the membrane

$$F_{dr} = -\frac{dE}{dx_{m1}} = \frac{1}{2}\frac{\varepsilon A}{(d_a + d_m/\varepsilon_r + x_{m1})^2}V^2 \tag{2.4}$$

Where the voltage across the capacitor is described as

$$V = V_b + V_t \sin \omega t \tag{2.5}$$

The equation of motion for the membrane, combining driving, damping and stiffness terms, is therefore:

$$F = m_m \ddot{x}_{m1} = \frac{1}{2} \frac{\varepsilon A}{(d_a + d_m/\varepsilon_r + x_{m1})^2} V^2 - b\dot{x}_{m1} - kx_{m1} \tag{2.6}$$

The first term is a driving force whereas the second term is a damping term (proportional to membrane velocity) and the third term a restoring force (proportional to the distance of the film from equilibrium). The equilibrium point ($x_{m1} = 0$) is where both the bias voltage V_b and signal voltage V_t are zero. When there is no voltage, the film is free in its natural position and so there is no restoring force. However when a bias voltage is applied, the film is drawn in towards the backplane/air gap and a restoring force would try to bring the film back to its natural position; and the bias voltage force and restoring force would be equal. So the distance x_{m1} is the time-dependent displacement from the equilibrium point. The overall "stiffness" of the membrane (k) is due to a combination of the characteristic membrane stiffness (k_m) and the trapped air behind the membrane ($k_a = p_a \gamma A/d_a$). At high gas pressures, such as Earth's atmospheric pressure, the air behind the membrane dominates the stiffness term, so $k \approx k_a$. The opposite is true at low pressures, such as on the Martian surface, where the characteristic membrane stiffness dominates and $k \approx k_m$.

To simplify the equation

$$K = \frac{1}{2} \frac{\varepsilon A}{(d_a + d_m/\varepsilon_r + x_{m1})^2} \tag{2.7}$$

So the total force on the transmitting transducer membrane

$$F_t = K(V_b + V_t \sin \omega t)^2 - b\dot{x}_{m1} - kx_{m1} \tag{2.8}$$

When there is no transmitting voltage V_t, the bias voltage is balanced by the restoring force. When there is no applied voltage at all, the restoring force would bring the membrane back to its natural position. Since the film is free to move, this causes it to oscillate and produce a longitudinal acoustic wave of pressure P_t

$$P_t = \frac{F_t}{A} \tag{2.9}$$

$$P_t = \frac{K}{A}\left[(V_b + V_t \sin \omega t)^2 - \frac{b\dot{x}_{m1} - kx_{m1}}{K}\right] \tag{2.10}$$

2.4 Transducer Frequency Response

The frequency response of the transducers is dependent on the thickness of the film membranes and sizes of the air-gap sizes. Where the membrane stiffness dominates the frequency response, the peak frequency is given by [60]:

$$f_0 = \frac{2.405}{\pi D_a}\sqrt{\frac{T}{\rho_m}} \tag{2.11}$$

This expression uses Bessel functions as the membrane motion is derived in two-dimensions. If not dominated by the membrane stiffness, the peak frequency of the transducer response can be modelled by treating the surface features as gas "pistons" with the membrane oscillating in one dimension [61] (Figure 2.2).

$$f_0 = \frac{1}{2\pi}\sqrt{\frac{k_a}{m}} = \frac{1}{2\pi}\sqrt{\frac{\gamma P_a}{\rho d_m d_a}} \tag{2.12}$$

It is clear from this equation that there is a dependence on peak frequency with atmospheric pressure, which is not present in the stiffness-controlled regime (Equation 2.11). Therefore, at large atmospheric pressures the gas piston model should dominate the frequency response whereas in rarefied atmospheres, the frequency response should be dominated by the membrane stiffness.

Experimentally, the transducers should have a wide-band frequency response due to the wide range of air-gap sizes on the randomly contoured backplanes. As described in Section 1.4.1, correct selection of the operating frequency is vital for maximum signal transmission under Martian atmospheric conditions. Determining the frequency response of a forced, damped oscillator requires solving the equation of motion for the membrane in one dimension:

$$F = m\ddot{x} = F_0 \sin \omega t - b\dot{x} - kx \tag{2.13}$$

$$F_0 \sin \omega t = m\ddot{x} + b\dot{x} + kx \tag{2.14}$$

$$\omega_0^2 = \frac{k}{m} \tag{2.15}$$

$$\frac{F_0}{m} \sin \omega t = \ddot{x} + \frac{b}{m}\dot{x} + \omega_0^2 x \tag{2.16}$$

There are two parts to the equation solution; a steady-state and transient solution:

$$x(t) = x_0 \cos(\omega t - \phi) + x_1 e^{-bt/2m} \cos\left(t\sqrt{\omega_0^2 - b^2/4m^2} - \phi_1\right) \tag{2.17}$$

The steady-state solution (left term) is determined by the driving force, is of constant amplitude and does not depend on initial conditions. The transient solution (right term), on the other hand, is highly dependent on the initial

conditions and behaves like an undriven damped oscillator; that is to say the amplitude decays exponentially with time. Therefore the initial conditions are of no consequence in the long-term, where there are multiple oscillations or even continuous oscillations, as the oscillator will eventually behave purely as if due to the driving force.

The steady-state solution is obtained using a trial solution of the form

$$x(t) = x_0 \cos(\omega t - \phi) \tag{2.18}$$

where ϕ is the phase lag and x_0 is the oscillation amplitude.

$$\dot{x} = -\omega x_0 \sin(\omega t - \phi) \tag{2.19}$$

$$\ddot{x} = -\omega^2 x_0 \cos(\omega t - \phi) \tag{2.20}$$

Substituting into the equation of motion

$$\frac{F_0}{m} \sin \omega t = -\omega^2 x_0 \cos(\omega t - \phi) - \frac{b}{m} \omega x_0 \sin(\omega t - \phi) + \omega_0^2 x_0 \cos(\omega t - \phi) \tag{2.21}$$

$$\frac{F_0}{m} \sin \omega t = (\omega_0^2 - \omega^2) x_0 \cos(\omega t - \phi) - \frac{b}{m} \omega x_0 \sin(\omega t - \phi) \tag{2.22}$$

Using the identities

$$\cos(A - B) = \cos(A)\cos(B) + \sin(A)\sin(B) \tag{2.23}$$

$$\sin(A - B) = \sin(A)\cos(B) - \cos(A)\sin(B) \tag{2.24}$$

Gives

$$[x_0(\omega_0^2 - \omega^2)\cos\phi + x_0\tfrac{b}{m}\omega\sin\phi\cos\omega t + [x_0(\omega_0^2 - \omega^2)\sin\phi - x_0\tfrac{b}{m}\omega\cos\phi - \tfrac{F_0}{m}]\sin\omega t = 0 \tag{2.25}$$

Which is only possible if, simultaneously

$$x_0(\omega_0^2 - \omega^2)\cos\phi + x_0\frac{b}{m}\omega\sin\phi = 0 \tag{2.26}$$

$$x_0(\omega_0^2 - \omega^2)\sin\phi - x_0\frac{b}{m}\omega\cos\phi - \frac{F_0}{m} = 0 \tag{2.27}$$

These two equations can be combined to give an expression for the frequency response of the transducers:

$$\frac{x_0}{F_0} = \frac{1}{\sqrt{(\omega_0^2 - \omega^2)^2 + (\frac{b}{m})^2\omega^2}} \tag{2.28}$$

However, this is an ideal result since the values of k, m and b will be slightly different for each "piston". The real frequency response would have a slightly wider peak than expected due to the range of these values, but as shown in Figure 2.3 the difference is negligible. Since $\omega_0^2 = k/m$, and $k \propto 1/d_a$, Equation 2.28 can also be used to predict the dependence of the response on air gap depth d_a for operation at a given signal frequency ω; the optimum air gap depth is that which results in a resonant frequency close to the operating frequency ω.

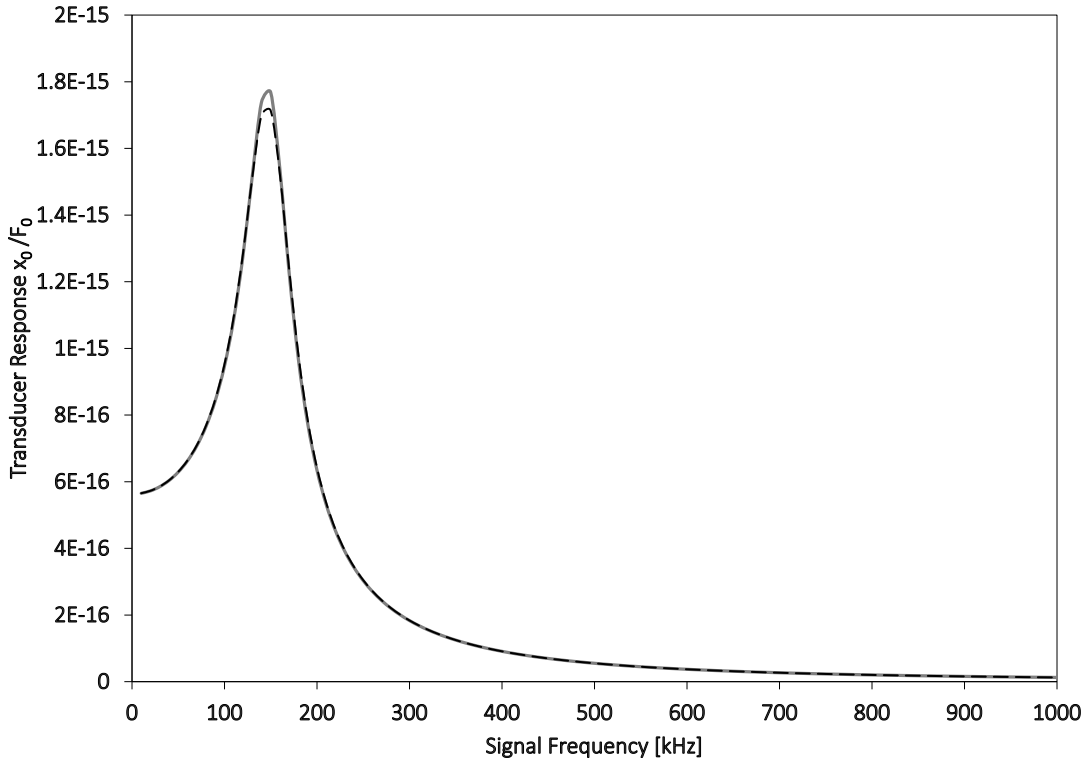


Fig. 2.3: Theoretical frequency response for a transducer with a natural frequency of 150 kHz (grey line). The dashed line is the result of a 10% variation in the air gap size, with corresponding different values of ω_0, and is almost indistinguishable from the original single-frequency plot

The frequency response peaks at the resonant frequency ω_0; this is the optimum driving frequency for maximum signal amplitudes. Below the resonant frequency, the oscillator is stiffness dominated; whereas the mass of the membrane dominates at high frequencies. The oscillator is in phase with the driving force for $\omega \ll \omega_0$, in phase quadrature at $\omega = \omega_0$ and anti-phase for $\omega \gg \omega_0$. The quality factor Q of the transducers equals the resonant amplification factor and affects how peaked the frequency response is:

$$Q = \frac{x_0(\omega = \omega_0)}{X_0} = \frac{m\omega_0}{b} = \frac{\sqrt{km}}{b} \tag{2.29}$$

The fractional width of the peak

$$\frac{\Delta\omega}{\omega_0} = \frac{1}{Q} \tag{2.30}$$

$$\Delta\omega = \frac{\omega_0}{Q} = \frac{b}{m} \tag{2.31}$$

Where the peak edges are defined at $1/\sqrt{2}$ of the maximum amplitude. Since $k \propto 1/d_a$, rougher backplanes should produce wider fractional peak widths. This can also be achieved through the use of thinner films; which provide a smaller mass to oscillate. When $Q > 1$, the resonance curve is sharply peaked whereas the resonance is not pronounced for $Q < 1$. The quality factor is a useful quantity as it combines all three parameters; k, m and b.

2.5 Losses to the Atmosphere

Travelling through the fluid, the transmitted acoustic wave is subject to three sources of signal loss. The signal is attenuated due to absorption in the fluid, impedance mismatches between transducers and fluid and the divergence of the beam (beam spreading). These losses are significant and frequency-dependent. As described in Section 1.4.1, the selection of operating frequency is vital in maximising signal transmission through planetary atmospheres.

2.5.1 Absorption Losses

The acoustic intensity (I_L), proportional to the square of the acoustic pressure, is attenuated with distance travelled (L) according to the following formula:

$$I_L = I_0 e^{-\alpha L} \tag{2.32}$$

Where α is the attenuation coefficient of the fluid.

$$\frac{P_L^2}{P_t^2} = e^{-\alpha L} \tag{2.33}$$

2.5.2 Impedance Mismatch Losses

Impedance is the factor which allows assessment of how the transducers perform at low pressures (or densities). Wherever there is an impedance difference between transmission media, signal is lost due to reflection at each boundary (Figure 2.4).

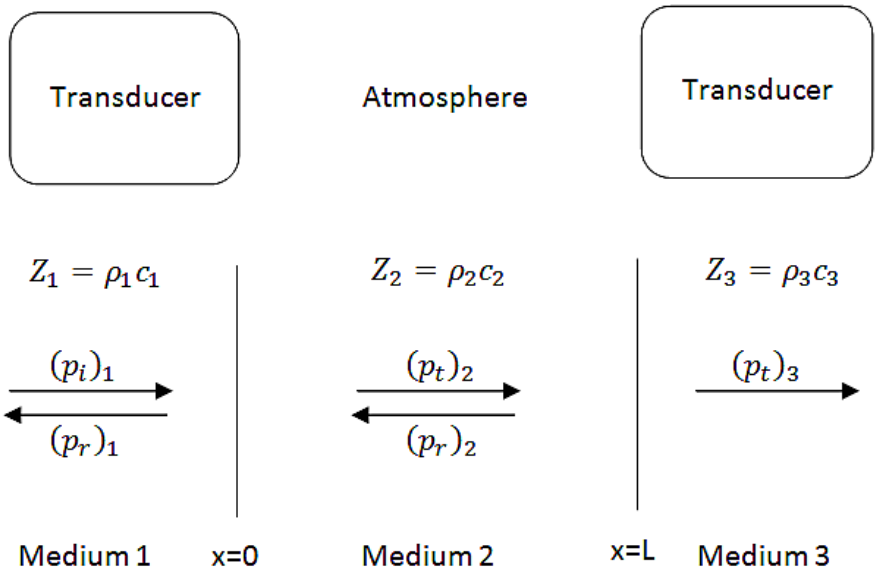


Fig. 2.4: Model of impedance losses

The pressure acting on the diaphragm in the transmitting transducer (medium 1) can be expressed as:

$$(p_i)_1 = A_1 e^{j(\omega t - k_1 x)} \tag{2.34}$$

Due to impedance mismatches between the different media, some of the incident pressure waves are reflected at each interface.

$$(p_r)_1 = B_1 e^{j(\omega t + k_1 x)} \tag{2.35}$$

$$(p_t)_2 = A_2 e^{j(\omega t - k_2 x)} \tag{2.36}$$

$$(p_r)_2 = B_2 e^{j(\omega t + k_2 x)} \tag{2.37}$$

$$(p_t)_3 = A_3 e^{j(\omega t - k_3 [x - L])} \tag{2.38}$$

The continuity of pressure at $x = 0$ gives

$$A_1 + B_1 = A_2 + B_2 \tag{2.39}$$

The continuity of particle velocity at $x = 0$ gives

$$Z_2(A_1 - B_1) = Z_1(A_2 - B_2) \tag{2.40}$$

The continuity of pressure at $x = L$ gives

$$A_2 e^{-jk_2 L} + B_2 e^{jk_2 L} = A_3 \tag{2.41}$$

The continuity of particle velocity at $x = L$ gives

$$\rho_3 c_3 \left(A_2 e^{-jk_2 L} + B_2 e^{jk_2 L} \right) = Z_2 A_3 \tag{2.42}$$

The continuity of pressure and velocity equations at $x = 0$ can be combined to

eliminate B_1

$$A_1 = \frac{(Z_2 + Z_1)A_2 + (Z_2 - Z_1)B_2}{2Z_2} \tag{2.43}$$

Similarly, the continuity equations at $x = L$ can be combined

$$A_2 = \frac{Z_3 + Z_2}{2Z_3} A_3 e^{jk_2 L} \tag{2.44}$$

$$B_2 = \frac{Z_3 - Z_2}{2Z_3} A_3 e^{-jk_2 L} \tag{2.45}$$

Substituting these equations into the $x = 0$ continuity equation combination

$$\frac{A_1}{A_3} = \frac{(Z_2 + Z_1)(Z_3 + Z_2)e^{jk_2 L} + (Z_2 - Z_1)(Z_3 - Z_2)e^{-jk_2 L}}{4Z_3 Z_2} \tag{2.46}$$

$$\frac{A_3}{A_1} = \frac{4Z_3 Z_2}{(Z_2 + Z_1)(Z_3 + Z_2)e^{jk_2 L} + (Z_2 - Z_1)(Z_3 - Z_2)e^{-jk_2 L}} \tag{2.47}$$

$$= \frac{4Z_3 Z_2}{[Z_2 Z_3 + Z_2^2 + Z_1 Z_3 + Z_1 Z_2]e^{jk_2 L} + [Z_2 Z_3 - Z_2^2 - Z_1 Z_3 + Z_1 Z_2]e^{-jk_2 L}} \tag{2.48}$$

$$= \frac{4Z_3 Z_2}{2Z_2 Z_3 \cos k_2 L + 2Z_1 Z_2 \cos k_2 L + 2Z_2^2 j \sin k_2 L + 2Z_1 Z_3 j \sin k_2 L} \tag{2.49}$$

$$\frac{A_3}{A_1} = \frac{2Z_3 Z_2}{(Z_2 Z_3 + Z_1 Z_2)\cos k_2 L + (Z_2^2 + Z_1 Z_3) j \sin k_2 L} \tag{2.50}$$

$$\frac{A_3}{A_1} = \frac{2Z_3}{(Z_3 + Z_1)\cos k_2 L + (Z_2 + Z_1 Z_3/Z_2) j \sin k_2 L} \tag{2.51}$$

For transmission from medium 1 through 2 to 3, the acoustic transmission coefficient is defined as the ratio of transmitted and incident sound intensities [56]:

$$\alpha_t = \frac{(P_t)_3^2/2Z_3}{(P_i)_1^2/2Z_1} = \frac{Z_1}{Z_3}\frac{|A_3|^2}{|A_1|^2} \tag{2.52}$$

$$\frac{P_r^2}{P_t^2} = \frac{|A_3|^2}{|A_1|^2} = \frac{4Z_3^2}{(Z_3 + Z_1)^2 \cos^2 k_2 L + (Z_2 + Z_1 Z_3/Z_2)^2 \sin^2 k_2 L} \tag{2.53}$$

In this case, we can say that $Z_1 = Z_3$

$$\frac{P_r^2}{P_t^2} = \frac{4Z_1^2}{4Z_1^2 \cos^2 k_2 L + (Z_2 + Z_1^2/Z_2)^2 \sin^2 k_2 L} = \frac{4}{4\cos^2 k_2 L + (Z_2/Z_1 + Z_1/Z_2)^2 \sin^2 k_2 L} \tag{2.54}$$

The pressure losses against transducer impedance for Mars and Earth atmospheres can therefore be plotted (Figure 2.5).

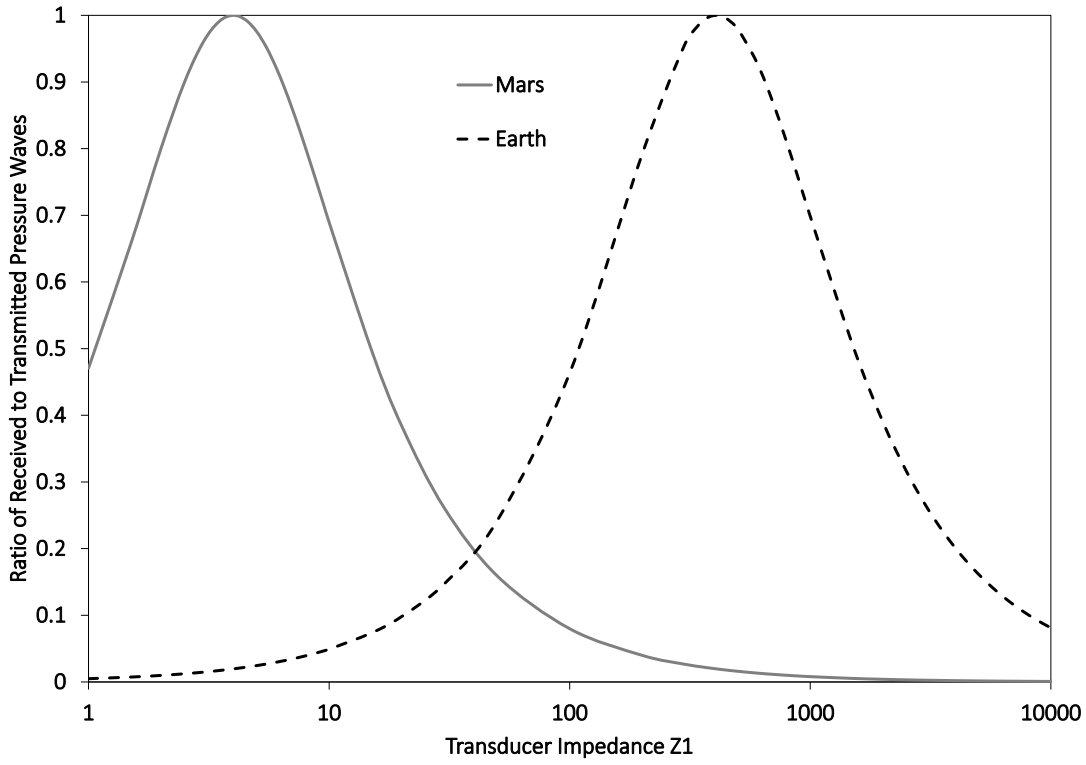


Fig. 2.5: Pressure losses to the atmospheres of Mars and Earth for different transducer impedances

This plot confirms the prediction from Chapter 1 that a transducer which is optimised for use on Earth may not work at all on Mars; and vice-versa. This is also evident when the impedance mismatches are used to predict the change in received amplitude with pressure (Figure 2.6).

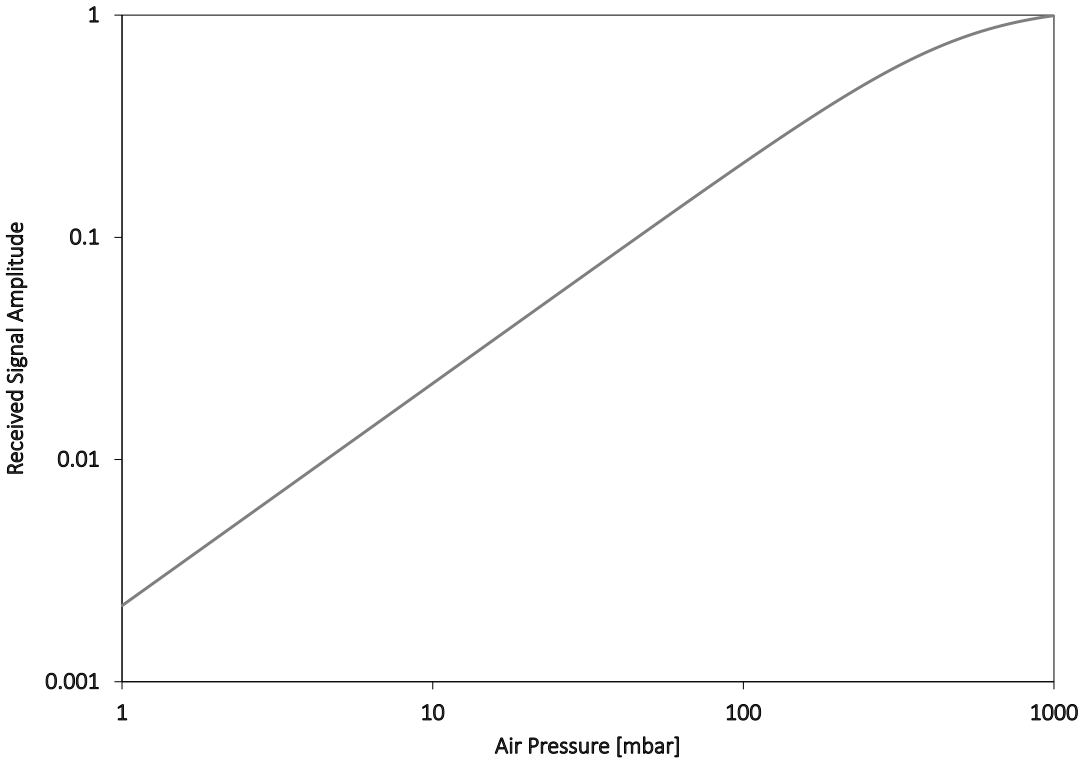


Fig. 2.6: Expected dependence of received signal amplitude on air pressure due to impedance losses, for two transducers 10 cm apart using a 100 kHz signal frequency

Figure 2.6 illustrates even more clearly that a transducer which operates well at Earth atmospheric pressures (~1010 mbar) will have much lower received signal amplitudes at Mars pressures (~6 mbar). This substantiates the hypothesis that capacitive ultrasonic transducers, with their comparatively low acoustic impedance, are the optimal choice for acoustic anemometry on Mars.

2.5.3 Beam Spreading Losses

The beam pattern of the acoustic waves varies with distance from the transmitting transducer. There are two distinct regions in which the waves behave very differently; the Fresnel zone (near-field) and the Fraunhofer zone (far-field). Within the Fresnel zone, nearest to the transmitting transducer, there is significant variation in signal intensity but no beam divergence; so losses

are purely due to attenuation. The point at which the behaviour changes from near-field to far-field is called the natural focus N of the transducer, and depends on diameter D.

$$N = \frac{D^2}{4\lambda} \tag{2.55}$$

The natural focus sets the optimum separation between transducers as it is where the intensity is at a maximum and the beam angle is at a minimum. Beyond the natural focus, in the Fraunhofer zone, losses occur due to attenuation and beam divergence. The full beam interference pattern, using Bessel functions, is given by

$$I(\theta) = I_0 \left(\frac{2J_1 kDsin\theta}{kDsin\theta} \right)^2 \tag{2.56}$$

Where the absolute edge of the beam angle can be approximated by

$$\sin \frac{\theta}{2} = \frac{1.22\lambda}{D} \tag{2.57}$$

The interference pattern along the beam length is given by the following equation:

$$p(z) = 2p_t \left| \sin \left(\frac{k}{2} \left[\sqrt{r^2 + z^2} - z \right] \right) \right| \tag{2.58}$$

The beam spreading losses can be calculated from the ratio of the receiving transducer area to the radiated area since any signal which does not reach the receiver is lost.

$$\frac{P_r^2}{P_t^2} = \frac{Transducer\ Area}{Beam\ Area} = \frac{A}{\pi (L \tan \theta)^2} \tag{2.59}$$

As detailed in Section 1.4.1, beam spreading losses to the atmosphere are frequency-dependent since the beam angle is reduced at higher frequencies.

2.6 Receiver Modelling

Combining the attenuation, beam spreading and impedance mismatch losses gives:

$$P_r^2 = P_t^2 \left[e^{-\alpha L} \times \frac{4Z_1^2}{4Z_1^2 \cos^2 k_2 L + (Z_2 + Z_1^2/Z_2)^2 \sin^2 k_2 L} \times \frac{A}{\pi (L \tan\theta)^2} \right] = P_t^2 Y^2 \tag{2.60}$$

Where Y is a term incorporating all the fluid losses between transmitter and receiver. When the attenuated pressure wave reaches the receiving transducer, it exerts an oscillating force on the transducer film

$$F_r = AP_r \tag{2.61}$$

This changes the capacitance of the receiving transducer and, due to the bias voltage, also varies the voltage across it. The receiver can be modelled as a condenser microphone with active capacitance C_a and stray capacitance C_s coupled to an AC voltage source (Figure 2.7):

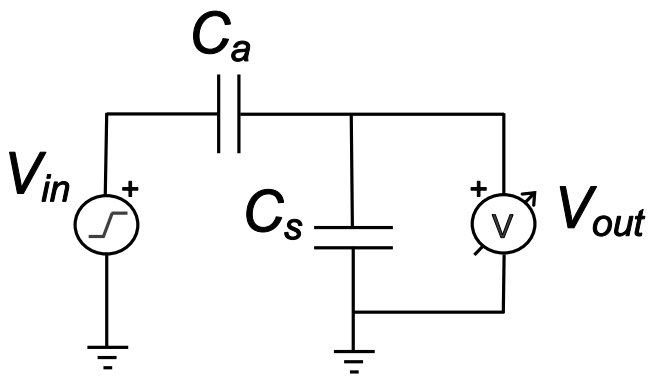


Fig. 2.7: Receiver Electrical Model

For this equivalent circuit

$$V_{out} = V_{in}\frac{C_a}{C_a + C_s} \tag{2.62}$$

Dynamic receiver diaphragm displacement

$$x_{m2} = \frac{U}{j\omega A} \tag{2.63}$$

Assuming a constant electric field inside the capacitor, the incoming acoustic wave produces an AC signal voltage:

$$V_{in} = \frac{x_{m2}V_b}{d_a} = U\frac{V_b}{j\omega A d_a} \tag{2.64}$$

$$U = \frac{p}{Z_1} \tag{2.65}$$

Since the air gap capacitance does not vary much and is much less than the film capacitance, we can assume that the capacitances are constant:

$$V_{out} = U\frac{V_b}{j\omega A}\frac{C_a}{d_a}\frac{C_a}{C_a + C_s} = \frac{P_r}{Z_1}\frac{V_b}{j\omega A d_a}\frac{C_a}{C_a + C_s} \tag{2.66}$$

Additionally, we can assume that $C_a \gg C_s$ giving

$$V_{out} = \frac{P_r}{Z_1}\frac{V_b}{j\omega A d_a} \tag{2.67}$$

Using the transmitted pressure wave from before (Equation 2.10)

$$V_{out} = \frac{KYV_b}{AZ_1 j\omega d_a}\left[(V_b + V_t \sin\omega t)^2 - \frac{b\dot{x}_{m1} - kx_{m1}}{K}\right] \tag{2.68}$$

In this equation, all three terms are frequency-dependent. The first two terms in

square brackets represent the driving force and the last term signifies the damping force. The behaviour of the transducers depends on the relative magnitudes of the different terms; which in turn are dependent on the different parameters. Note that this analysis has been purely based on how the various parameters affect the received signal amplitude; and that knowing all of the values of this equation will not give an accurate value for the received signal. However, this expression does model how the received signal amplitude is dependent on the various transducer parameters. A computer model of Equation 2.68 was used to extract the effect of each individual parameter on received signal amplitude, neglecting frequency dependence:

$$V_{out} \propto d_a^{-3} V_b^{2.04} d_m^{-2} D^2 e^{-L} sinc^2(\theta) \tag{2.69}$$

From this analysis, it was clear which factors would, theoretically, have the greatest impact on the received signal amplitude V_{out}. As discussed in Chapter 1, instrument reliability is dependent on having a large received signal which is distinguishable from the noise. The four most important theoretical factors in maximising received signal amplitude, from the parameter indices in Equation 2.69, are air-gap thickness d_a, bias voltage V_b, membrane thickness d_m and backplane diameter D. The focus of the discussion will now shift to the practical application of these transducers, how they are affected by these factors and to what extent they behave in line with the theory outlined in this Chapter.

3. TRANSDUCER CHARACTERISATION AND OPTIMISATION

Following on from the establishment of the theoretical operation of transducers, it is necessary to discuss how they are constructed and perform experimentally.

3.1 Transducer Construction

An existing pair of 14 mm diameter prototype transducers were available at the start of the project, but initial testing found that they were unsuitable for several reasons. Primarily, they were designed to be flight-like and, due to their size, did not allow testing of backplanes larger than 10 mm diameter. They were not designed for evaluation of different backplanes and films; and consequently the disassembly and reassembly process was laborious. Additionally, the design of the transducer heads was such that it was common for the backplanes and films to touch, creating an electrical short which was often difficult to eliminate. As such, they were incapable of testing the four main parameters affecting transducer performance established in Equation 2.69. An improved transducer design, loosely based on these prototype transducers, was developed and specified to allow for a wider range of testing parameters whilst also addressing the issues identified in the previous design. The specifications for the transducers designed for testing are given in Table 3.1.

Parameter	Specified Testing Range
Backplane Roughness	1-500 μm
Bias Voltage	0-60 V
Membrane Thickness	1-15 μm
Backplane Diameter	5-20 mm

Tab. 3.1: Range of test parameters specified in transducer design

All construction materials were chosen to be compatible with spaceflight; more specifically low density, low outgassing and qualifiable.

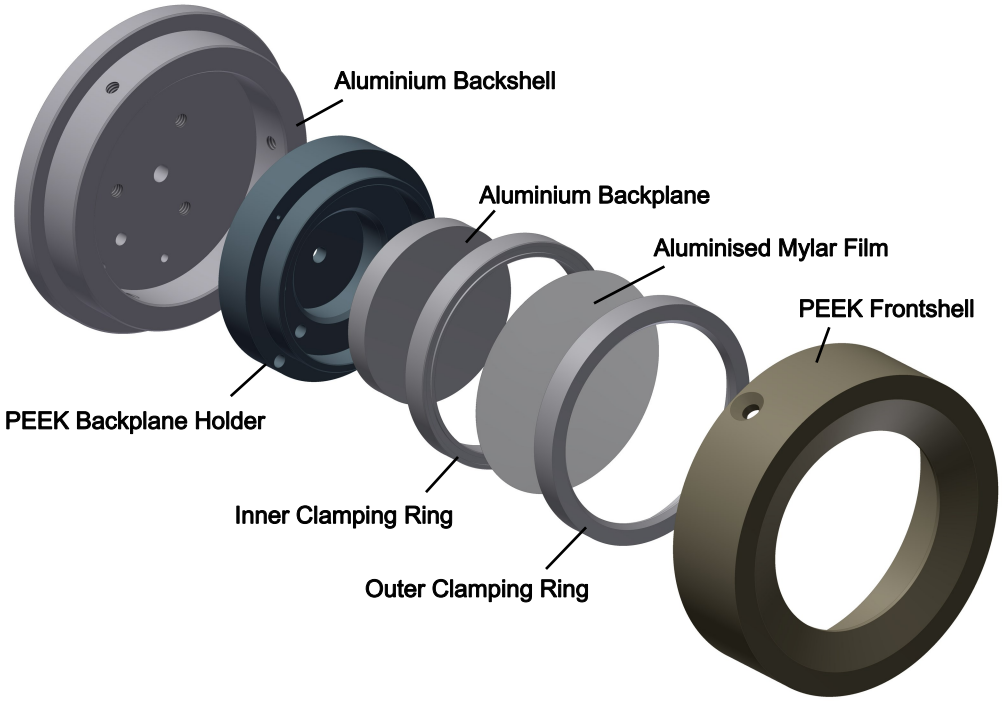


Fig. 3.1: Exploded diagram detailing transducer construction

Each individual transducer is made up of a selection of components, shown in Figure 3.1. All of the components are secured to an aluminium backshell, whilst also being electrically isolated from each other. A Polyether Ether Ketone (PEEK) component isolates the backplane from the backshell and holes in both components allow a coated electrical wire to connect to the backplane. The aluminised film is clamped between two stainless steel rings to keep it taught. These are assembled

by first laying the aluminised film, conductive side down, on a clean glass plate and securing it in place by gluing the edges; whilst under tension. A recess on the front of the the inner ring is then filled with a small amount of conductive epoxy and very carefully placed on top of the taught film. The assembly is then left to cure in an oven, to allow the epoxy to secure the ring to the film, and a scalpel is used to cut around the ring. The outer ring is finally glued to the inner ring and a wire glued to the inner ring for electrical continuity with the film. The PEEK backplane holder allows the insulating side of the film membrane to be taught against the contoured front side of the backplane whilst also ensuring the metal rings and backplane do not make contact; and allowing the film assembly wire a path through the back of the transducer. A PEEK frontshell then secures all the internal components in place and is screwed into the aluminium backshell.

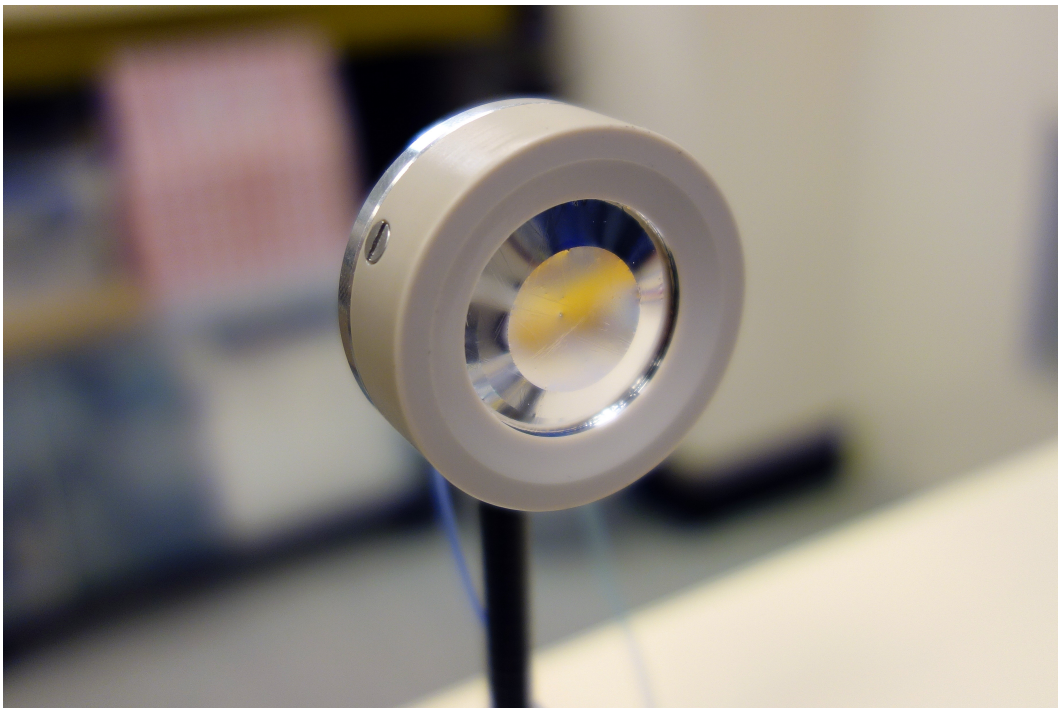


Fig. 3.2: An assembled 38 mm diameter transducer head designed for testing, housing a 14 mm backplane

The overall assembly (Figure 3.2) was purposefully built about four times larger than a flight model would be, to accommodate backplanes up to up to 20 mm in diameter and allow for easier exchanging of components. For testing, two identical transducers were manufactured. Each was secured to a carbon fibre rod assembly, which in turn was attached to an aluminium metal base allowing for the transducers to be secured in place at different separations.

3.2 Test Apparatus

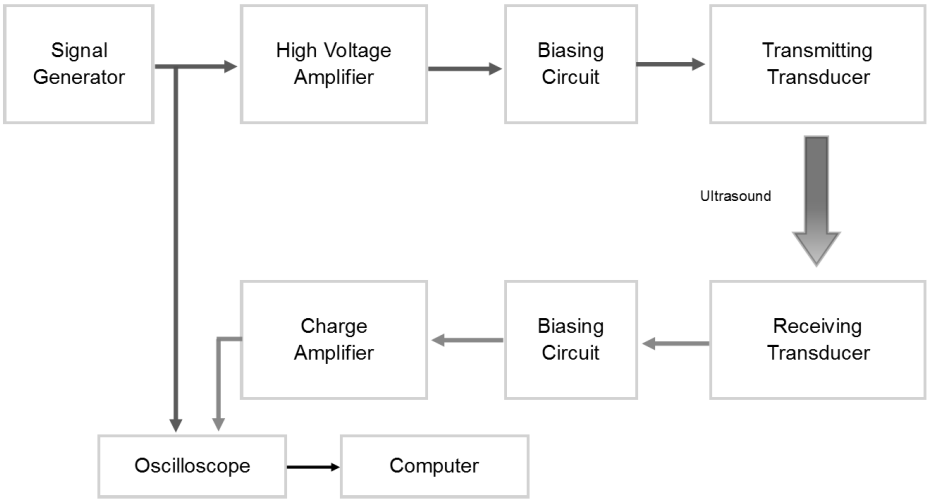


Fig. 3.3: Block diagram of experimental setup. A full electronic schematic can be found in Appendix B

The purpose of the test setup was to produce electronic signals which the transmitting transducer could then convert into acoustic waves; then measure the amplified output of the receiving transducer. Time-domain signals consisting of multiple sinusoidal pulses were used for the reasons discussed in Section 1.3.2. These signals were produced using a TTi TG1010 arbitrary waveform generator capable of outputting signals up to 10 VPP. The generated signals were then amplified to 140 VPP by a custom high-voltage amplifier built to specification

(frequency response included as Appendix A). Following amplification, the signal was passed through a biasing stage; a potential divider superimposing a DC voltage (typically 60V) on the AC signal. The transmitting transducer converted this electronic signal into acoustic waves which, when received at the receiving transducer, were converted back into an electrical signal.

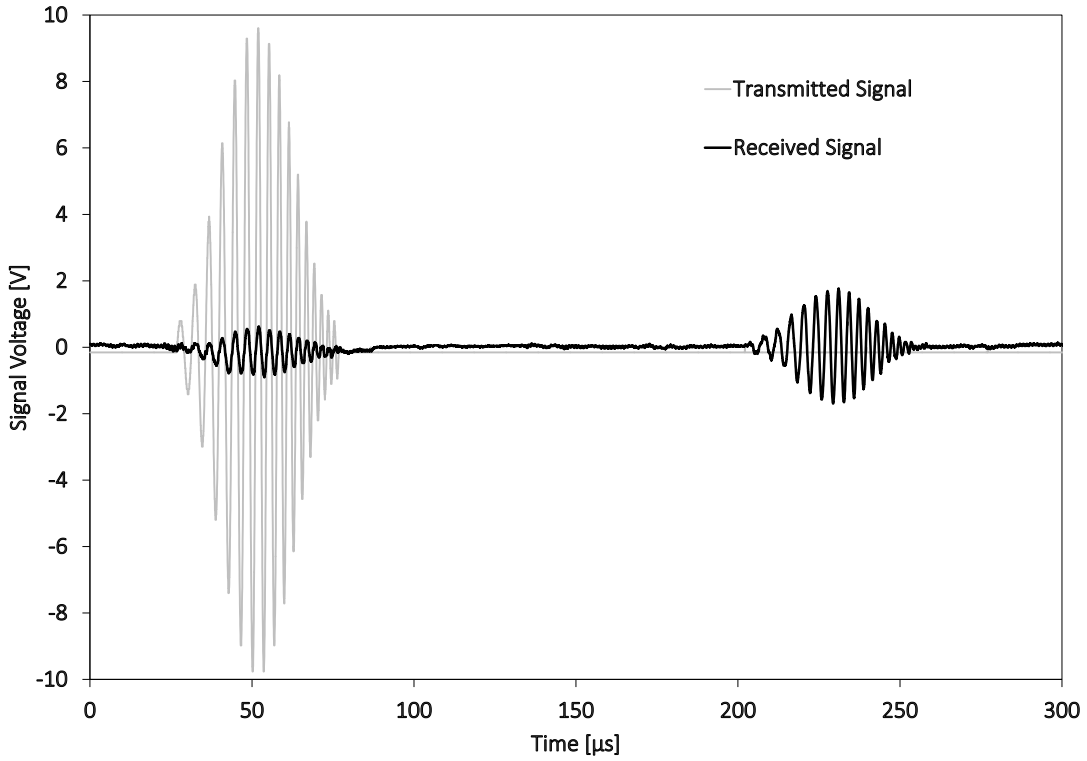


Fig. 3.4: Transmitted (light) and received (dark) signal voltages. The transmitted signal shown is pre-amplification and some coincident electrical pickup is visible in the received signal. Note that, for transducer testing purposes, frequency and amplitude modulation of the sinusoidal waves was not performed. These were only applied for later tests involving signal detection (Section 4.3)

Signal amplification and receiving transducer bias were provided by a Cooknell CA7/C amplifier [57] whose output (Figure 3.4) was measured by an oscilloscope (Tektronix TDS3054). The CA7/C had 3 dB frequency cutoff at 10 kHz and 25 MHz. Appendix B shows a complete circuit diagram for the test electronics, including a schematic of the Cooknell amplifier.

Initial laboratory tests were performed in air, as it has already been established that signal propagation is more difficult in air than CO_2 at the same pressure (Section 1.4). Transducer performance at low pressure was evaluated in a vacuum chamber (Figure 3.5), which contained sensors for measuring the pressure (piezoresistive), temperature (silicon band-gap) and humidity (capacitive) inside the chamber.

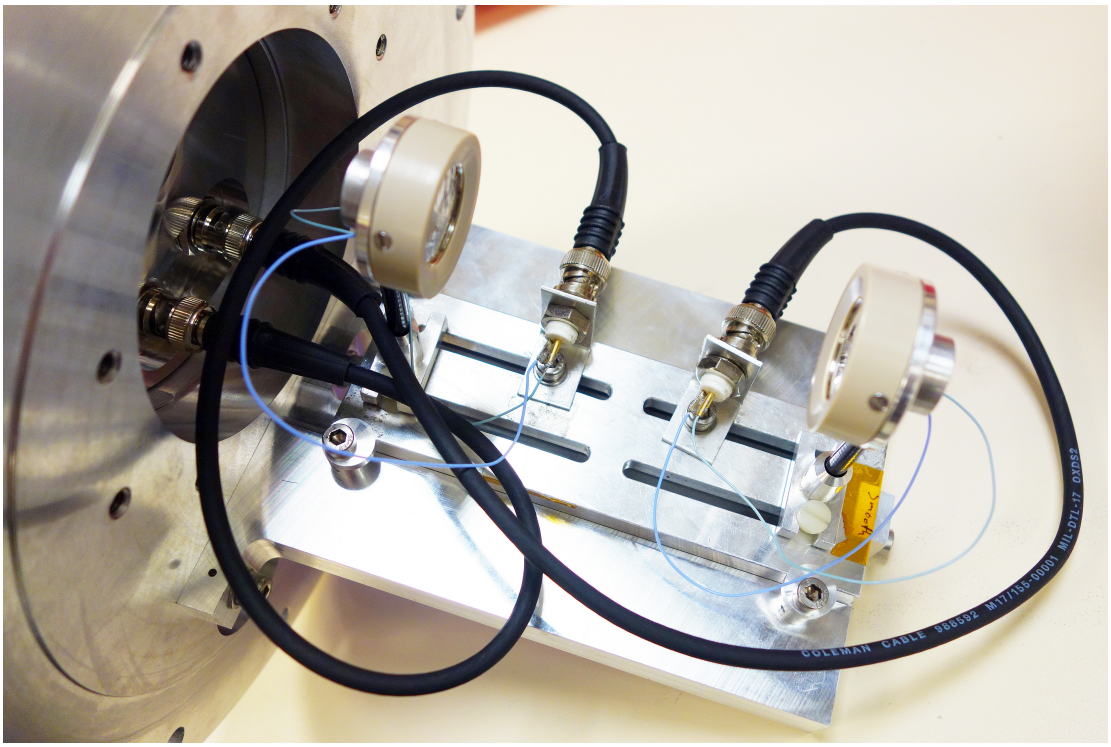


Fig. 3.5: Photograph showing the transducer assembly secured to the lid of the vacuum chamber before being lowered in. The environmental sensors are located on the other side of the mounting plate.

3.3 Experimental Procedure

A pulse train of two sinusoidal signals was used to allow for testing at low signal frequencies. All signal measurements, unless otherwise specified, were taken from oscilloscope measurements using 200x averaging to minimise the impact of both high- and low-frequency noise. Each data point was taken three times and averaged to give a value for the variability of the measurement. The averaging was necessary due to the very wide bandwidth of the Cooknell amplifier, but an electronic filter was not incorporated due to the wide range of signal frequencies under investigation. Averaging was performed solely for the purpose of accurately determining signal amplitudes, and would not be necessary for a flight instrument where electronic filters could be used if required.

To test the transducers in a rarefied atmosphere, the chamber was evacuated down to 0.1 mbar then back-filled to the desired pressure using a needle valve. Once the pressure had equilibrated, the signal amplitude was measured using the oscilloscope and the process repeated at specific intervals up to room pressure. No data was taken with the vacuum pump running as it produced too much acoustic noise; which would have introduced significant errors into the data. This low-frequency acoustic noise was not filtered out, to maintain the very wide bandwidth of the CA7/C for measuring transducer frequency response. Whilst reflections inside the chamber were visible in the received signal, they were disregarded by only measuring the first received signal.

Unless otherwise specified, all tests were conducted under the following conditions:

Parameter	Symbol	Value
Backplane Roughness	d_a	20.8 μm
Backplane Diameter	D	20 mm
Mylar Film Thickness	d_m	2 μm
Transducer Separation	L	9 cm
Air Pressure	P	1010 mbar
Signal Frequency	f	100 kHz
Signal Amplitude	V_t	70 V
Bias Voltage	V_b	60 V

Tab. 3.2: Default testing parameters

The errors plotted on each graph resulted from the standard deviation of each data point plus one least significant digit. Unless otherwise shown, all errors are contained within the individual marker areas.

3.4 Backplane Roughness

As described in Chapter 2, transducer performance depends strongly on backplane roughness characteristics. To test this prediction, ten identical 20 mm backplanes were manufactured on a lathe and then roughened; this process involved clamping the backplanes in a pillar drill and rotating them at 1370 rpm whilst gently making contact with an abrasive film five times for four seconds each. Initial testing suggested that rougher backplanes resulted in higher sensitivities so four different grit sizes (grades) of rough abrasive film were used: 30 μm (A30), 325 μm (S2), 525 μm (P36) and 750 μm (P24). Two backplanes were left as machined for comparison; and even greater roughnesses were achieved by machining equidistant V-shaped grooves of 0.1 mm, 0.2 mm and 0.5 mm into the backplanes. One

backplane from each pair was then optically profiled by an Alicona InfiniteFocus profilometer, with a vertical resolution of 20 nm, to measure their surface profiles (Figure 3.6).

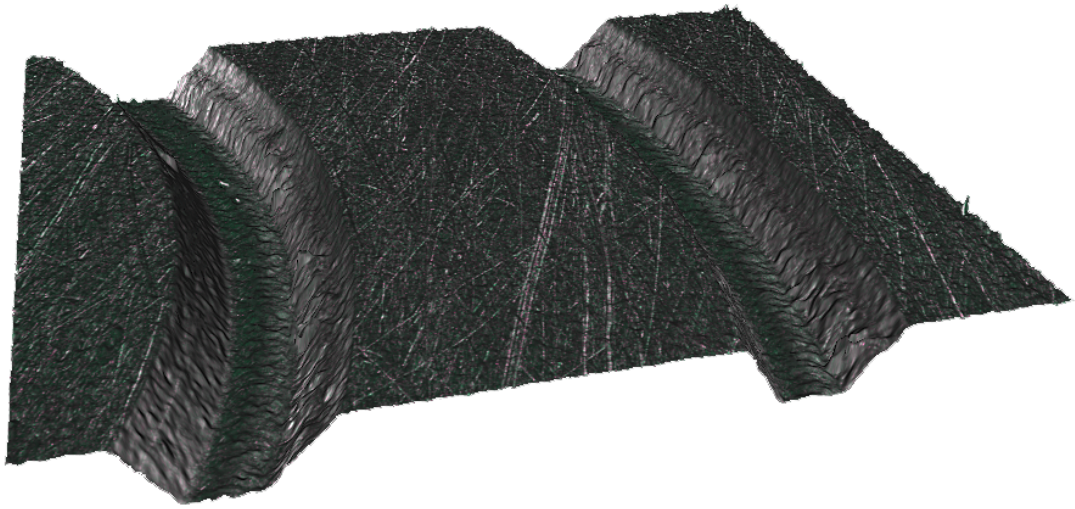


Fig. 3.6: 3-D middle section view of one of the 0.2 mm grooved backplane surface profiles

The profilometer software characterises the roughness using several metrics, as shown in Table 3.3. Of these, the mean peak-to-valley height (R_z) is the most representative of the air gap depth (d_a) described in Chapter 2.

Parameter	Description
Ra	Average Profile Roughness
Rq	RMS Profile Roughness
Rt	Maximum Peak-to-Valley Height
Rz	Mean Peak-to-Valley Height
Rp	Maximum Peak Height
Rv	Maximum Valley Depth
Rc	Mean Height of Irregularities

Tab. 3.3: Descriptions of surface roughness parameters

Three different 3 x 2 mm sections of each backplane - the centre, middle and edge, were profiled and from every section, three cross-sections were drawn across each. The roughness values for each backplane were averaged over all nine cross-sections and are plotted as Figure 3.7.

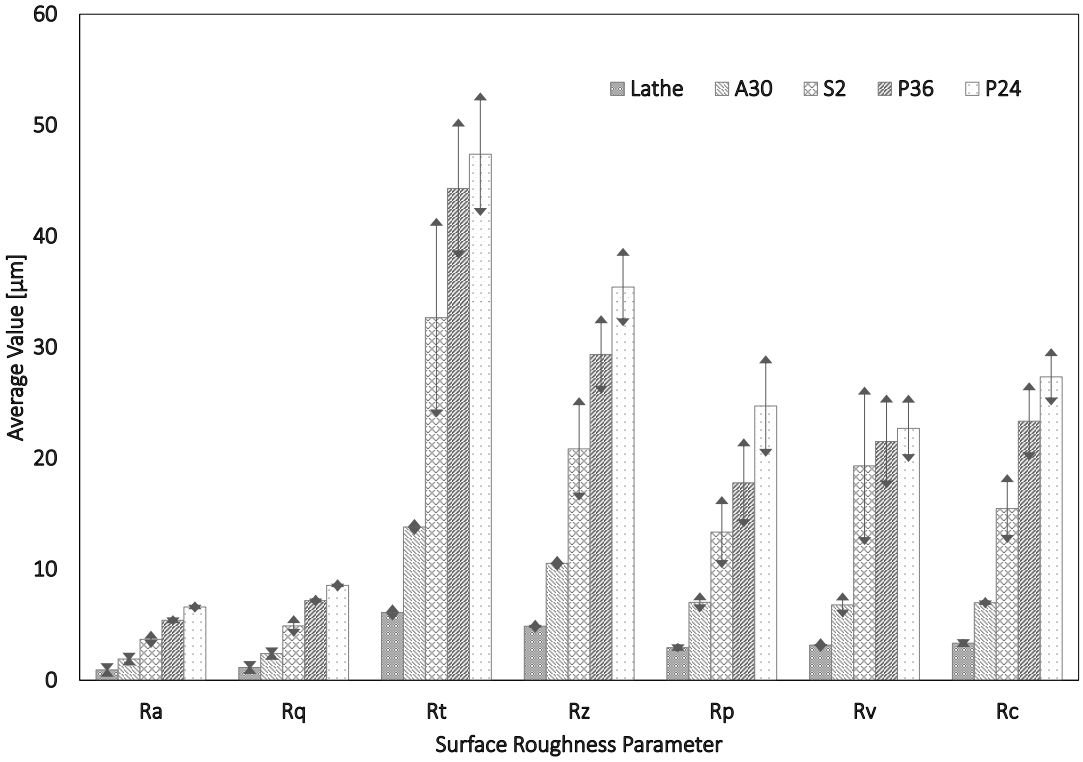


Fig. 3.7: Variation of backplane roughness with different grade of abrasive film applied. The standard deviations plotted result from the various sampling regions, and are much greater than those reported by the program for each section

Figure 3.7 confirmed the prediction that contouring with rougher abrasive films would result in larger peak-to-valley heights. The backplanes straight off the lathe were much smoother than even those contoured using the smoothest film tested. Using this technique, however, it was not possible to alter only the peak-to-valley height as the mean spacing between irregularities, Rsm, also varied. The backplanes contoured using the three roughest abrasive films had feature spacings of twice that of the Lathe or A30 ones. Additionally, whilst

there was a correlation between backplane roughness and abrasive film grit size, they were not on the same order of magnitude. This was likely due, in part, to the limited time of application of the film; which was to prevent too much material being taken away and altering the physical dimensions of the backplanes.

Now that the roughness of each contoured backplane was known, the performance of each pair of contoured backplanes could be evaluated and compared to the theoretical expectations (Section 2.6). Firstly, sensitivity at low air pressures was evaluated.

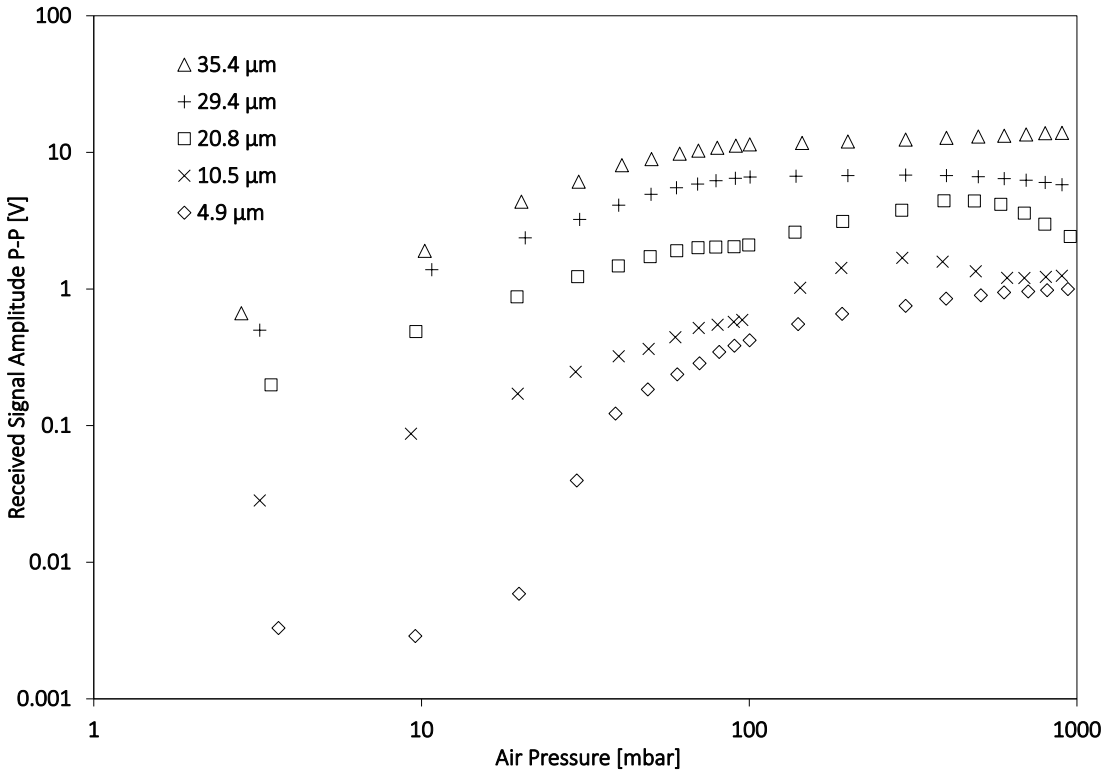


Fig. 3.8: Plot showing how transducer sensitivity at low pressure increases with backplane roughness d_a. Error bars are contained within the individual marker areas.

Figure 3.8 confirmed the initial testing results since the rougher backplanes clearly produced greater received signal amplitudes at all pressures than the

smoother ones. This is contrary to the theory (Equation 2.69), which predicted that the smoother backplanes would be the more sensitive. It should be noted that, of all the scientific literature reviewed, only one paper ([58]) reported that condenser microphone sensitivity increases with backplane roughness. The eight that dealt specifically with electrostatic transducers ([59]-[67]), all reported that sensitivity should increase with smaller air-gaps, and therefore MEMS backplanes. To investigate this discrepancy further, even rougher backplanes needed to be manufactured. The roughest film commercially available had already been used for contouring the backplanes, so three new pairs of transducers were manufactured with V-shaped grooves of different depths (0.1, 0.2 and 0.5 mm). Due to the design parameters of the test transducers, it was not possible to investigate groove depths >0.5 mm. These were then tested using the same procedure, but with smaller transmitted signal voltages to avoid clipping of the received signal. The received voltages then had to be amplified to allow comparison with the earlier dataset. Equation 2.28 was used to calculate the expected received amplitudes; using the difference between the driving frequency and natural frequency for a given backplane roughness. This data, averaging the values taken <50 mbar, is shown in Figure 3.9.

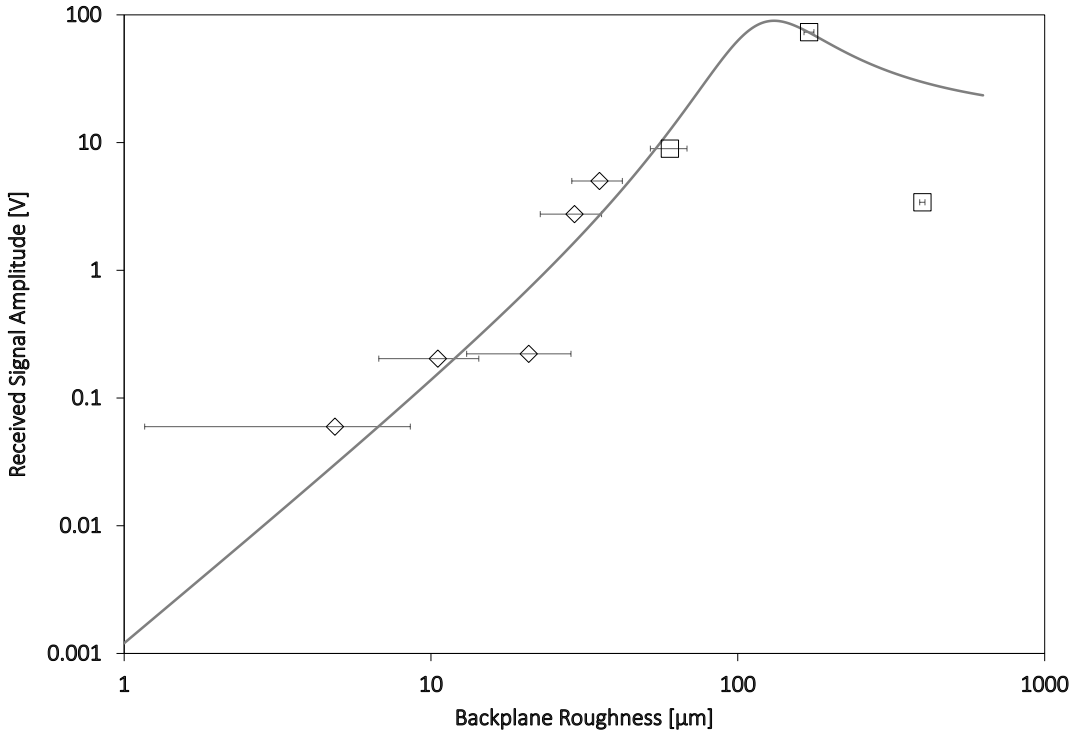


Fig. 3.9: Variation of transducer sensitivity with the different roughness backplanes, including theoretical prediction (solid line). The diamond-shaped points were roughened using abrasive films whereas the square points represent the V-groove backplanes. Plotted error bars represent roughness standard deviations.

The data plotted in Figure 3.9 confirms that transducer sensitivity does not constantly increase with backplane roughness, but that there is an optimum roughness around 0.2 mm for a signal frequency of 100 kHz. Above this roughness, sensitivity seems to decrease; though the one received amplitude measured above the peak roughness was much less than predicted by the theory. This may be partly due to the over-simplicity of the model, as it uses a single air gap, whereas the actual transducer backplanes exhibit a variety of air gap depths. Since the two different backplane profiling methods (abrasive films and grooves) lie on a line, the method used to profile the backplanes is unimportant; only the roughness of the backplane has an effect on received signal amplitudes. The observed behaviour qualitatively matches the analytical prediction and the

position of the peak is consistent with that expected from the analytical model. In addition to the backplane roughness, the sensitivity also depends on whether the driving frequency is much greater or less than the natural frequency of the transducers being tested; since the backplane roughness also affects the natural frequency. The most sensitive backplane roughness is highly dependent on the driving frequency; in this case, the 0.2 mm backplanes produced a natural frequency closest to the driving frequency, and so were the most sensitive. Looking back at the simplified theoretical prediction neglecting frequency dependencies (Equation 2.69), it is unphysical as it predicts that the sensitivity will become infinitely large at very small air gaps. As the air gap decreases to zero, the sensitivity should also fall to zero; as the stiffness of the gas piston will increase until it is infinitely stiff. Therefore, below some optimum air gap value, the sensitivity will necessarily fall off to reach zero at zero air gap depth. The overall stiffness, therefore, should be dominated by the air gap at small air gaps; and the membrane thickness should become more important as air gap is increased above an optimum value.

In addition to affecting the transducer sensitivity, the roughness of each pair of backplanes was expected to dictate the frequency response of the transducers. To verify this, the frequency response was measured using each backplane pair and the results presented as Figure 3.10 for the film profiled backplanes.

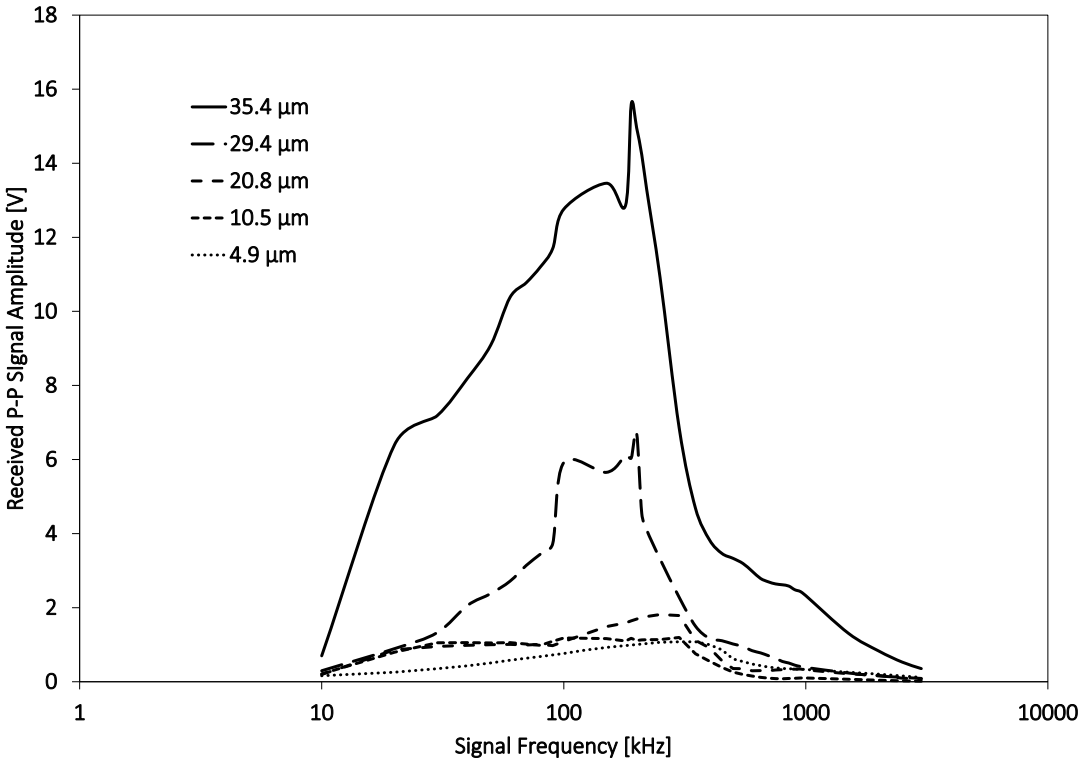


Fig. 3.10: Variation of frequency response with backplane roughness (air, 1010 mbar)

As predicted, rougher backplane transducers result in much lower peak frequencies; and again also much higher sensitivities. The wide range of observed roughness values in each sample leads to wide frequency peaks. In agreement with Equation 2.29, rougher backplanes lead to greater observed fractional peak widths (difference in frequencies where amplitude falls to $1/\sqrt{2}$ either side of peak, relative to peak frequency). The variation in roughnesses for each pair of contoured backplanes would not affect the fractional peak width as any roughness variations would affect the peak frequency and quality factor by equal amounts; and so cancel out. The electronics had a minimal effect on the observed frequency response and so were not corrected for.

The same process was used to obtain the frequency response of the V-groove backplanes, which were found to have much narrower peaks due to the smaller

variability in backplane depths (~1% for V-groove backplanes compared with ~10% for abrasively roughened backplanes). Comparing the measured peak frequency response due to the different roughness backplanes to the expected frequency response from Equation 2.12 yielded a very good agreement (Figure 3.11).

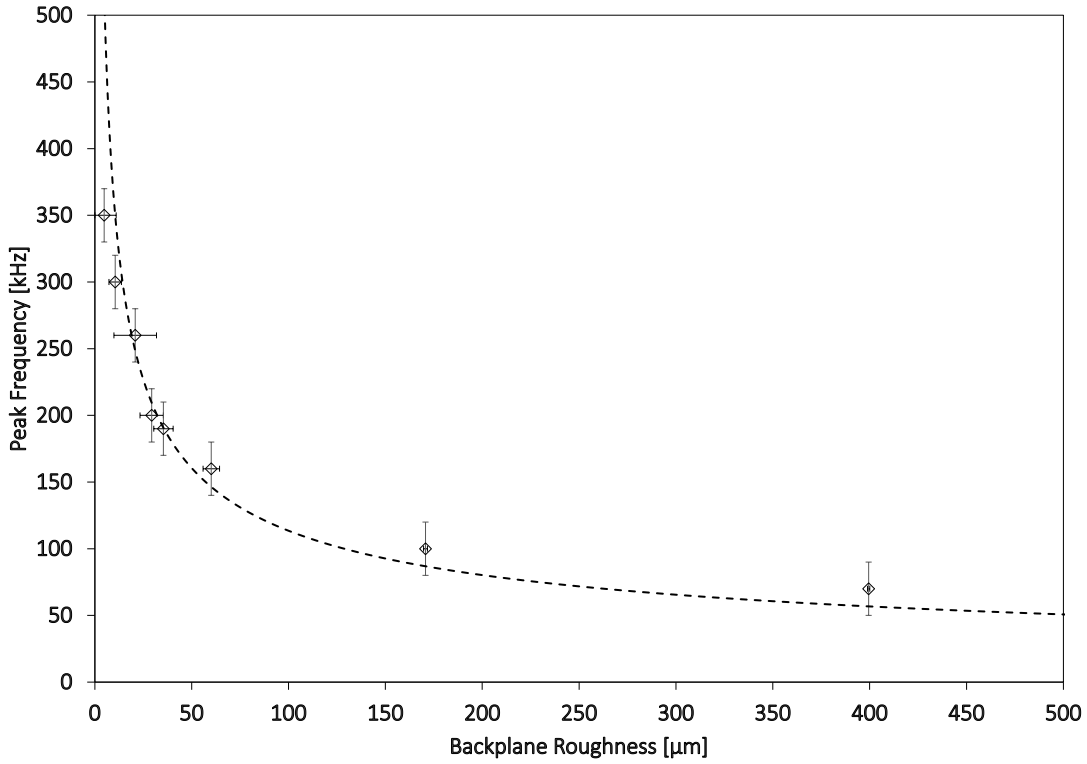


Fig. 3.11: Comparison of the measured peak frequency of the transducers with the theoretical prediction (dashed line). Plotted error bars represent backplane roughness standard deviation and frequency response resolution.

The data in Figure 3.11 confirms that the transducers performed as expected from the theoretical gas piston model in terms of their peak frequencies.

It was predicted that the smoother backplanes would have higher sensitivities but also higher peak frequencies. This should have resulted in a trade-off as it has previously been established how the Martian atmosphere is poorly suited to

high-frequency acoustic wave transmission (Section 1.4.1). However, backplane testing revealed that in general, for these transducers, rougher backplanes are favourable not only for their lower peak frequencies, but also their higher received amplitudes at Mars pressures. Using a signal frequency of 100 kHz, there appears to be an optimum roughness around 0.2 mm which produces the most sensitive transducers. This roughness results in transducers with a favourable peak frequency of 120 kHz in air at 1010 mbar (Section 3.8 investigates how the pressure and gas composition affects peak frequency of these backplanes). However, the narrow peak frequency responses exhibited by the grooved backplanes are undesirable as they could cause "ringing" of the received signal, resulting in more received oscillations than in the transmitted pulse. These additional oscillations can make it more difficult to distinguish which received peaks are due to the signal, and which are a result of the ringing, thereby making it more difficult to establish the time difference between sent and received pulses. This could be mitigated by having a range of groove depths, which would in turn produce a wider frequency response. This disadvantage is offset by the ease at which the desired frequency response can easily be tuned by the depth of the grooves. V-groove backplanes therefore demonstrate high potential for use on Mars; as they exhibit favourable peak frequencies and high sensitivities at low pressures. However, due to the order of testing, most tests were performed with abrasively roughened backplanes.

3.5 Bias Voltage

In order to test to what extent the theory modelled how the transducers behaved using different bias voltages, the bias voltage on the transmitting, receiving and then both transducers was varied and the impact on received signal amplitude measured as before. The results are shown in Figure 3.12.

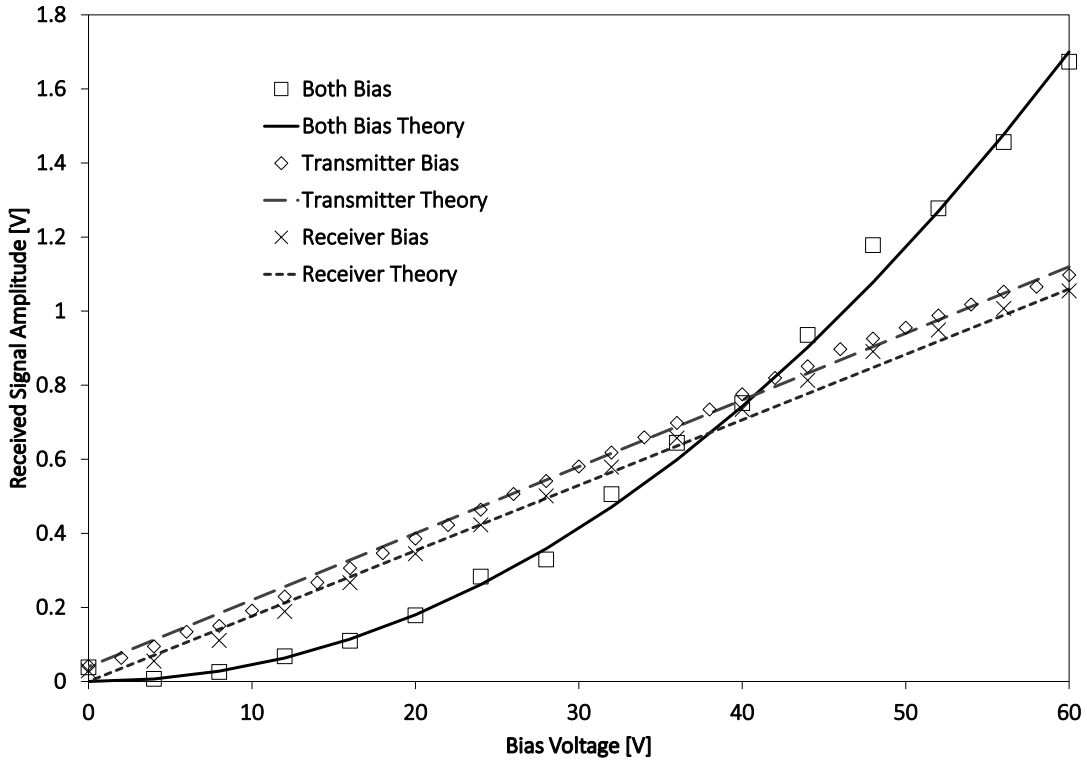


Fig. 3.12: Effect of varying the bias voltage across the transmitter, receiver and both transducers on received signal amplitude. There were fewer points when varying the receiver bias as the analogue dials made it more difficult to specify a specific voltage.

The experimental values fit the theoretical expectation well, with one key noticeable difference. The theory predicted that a zero bias voltage would result in no received signal amplitude, but a small signal was still visible with zero bias. This may be caused by residual charges on the films creating small electric fields between the films and backplanes and effectively performing the same role

as the bias voltage. The polarity of the bias voltage made no appreciable difference to transducer performance.

Whilst large bias voltages considerably increase the received signal amplitude, there is a limiting factor. Above the dielectric strength of the Mylar film (~30 $V/\mu m$), performance is significantly reduced as electrons can tunnel across the dielectric Mylar; creating a short-circuit between the metallised film and backplane. Bias voltages were limited to a maximum of 60 V for all final tests, as initial testing confirmed performance deteriorating above 65 V.

3.6 Membrane Thickness

The third most important factor in maximising received signal amplitude was postulated to be the membrane thickness. Mylar films were primarily chosen for their low density and high dielectric strength, as transducer sensitivity is dependent on the total mass of the film. Higher dielectric strengths allow the use of higher bias voltages, which in turn yield higher received signal amplitudes. The chosen films are also suitable for use on the Martian surface due to their wide operating temperature range and low thermal expansion coefficient. As with the other factors, their frequency response and performance at low pressure were measured.

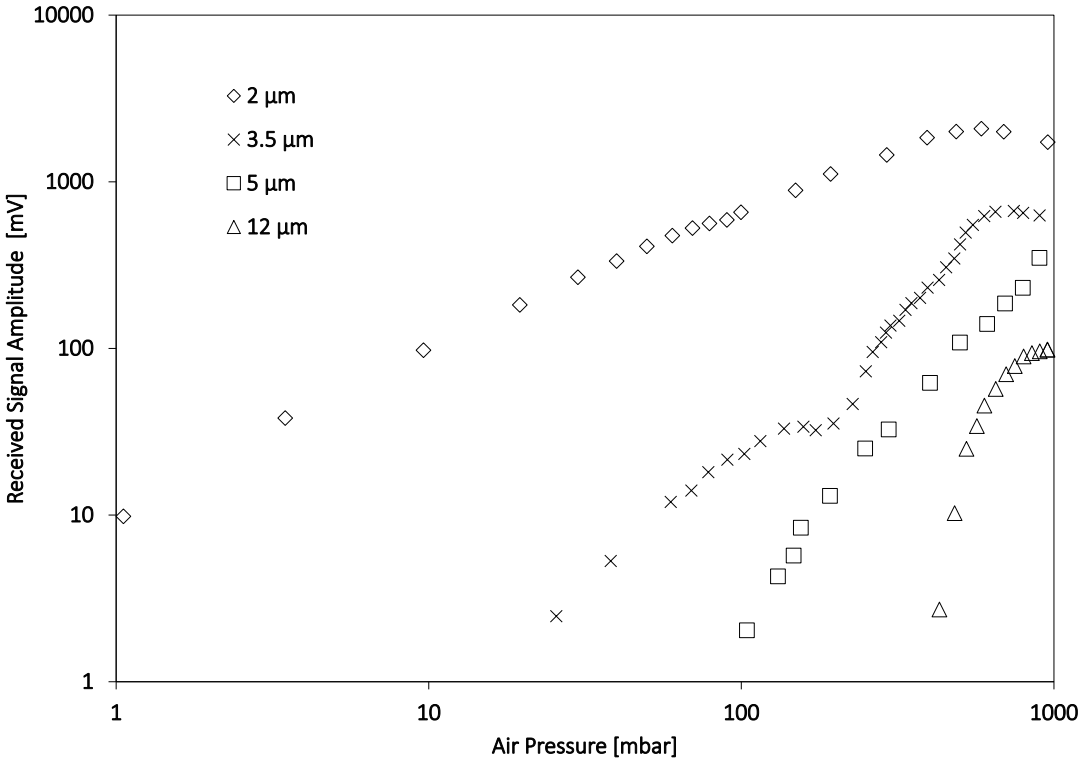


Fig. 3.13: Variation of transducer sensitivity at low pressures with different film thicknesses

The data shown in Figure 3.13 confirms that, as expected, the thinner the films, the greater the amplitude of the received signal. Only the 2 μm films are suitable for use at low pressures; though they would also be less robust and prone to damage than the thicker films. In general, the plots look very much like the expected relationship shown in Figure 2.6, especially for the 2 μm films. Using Figure 2.5, and the ratio of amplitudes at Earth and Mars pressures, the acoustic impedance of the transducers using 2 μm films was estimated to be ~250 $\mathrm{kgm^{-2}s}$.

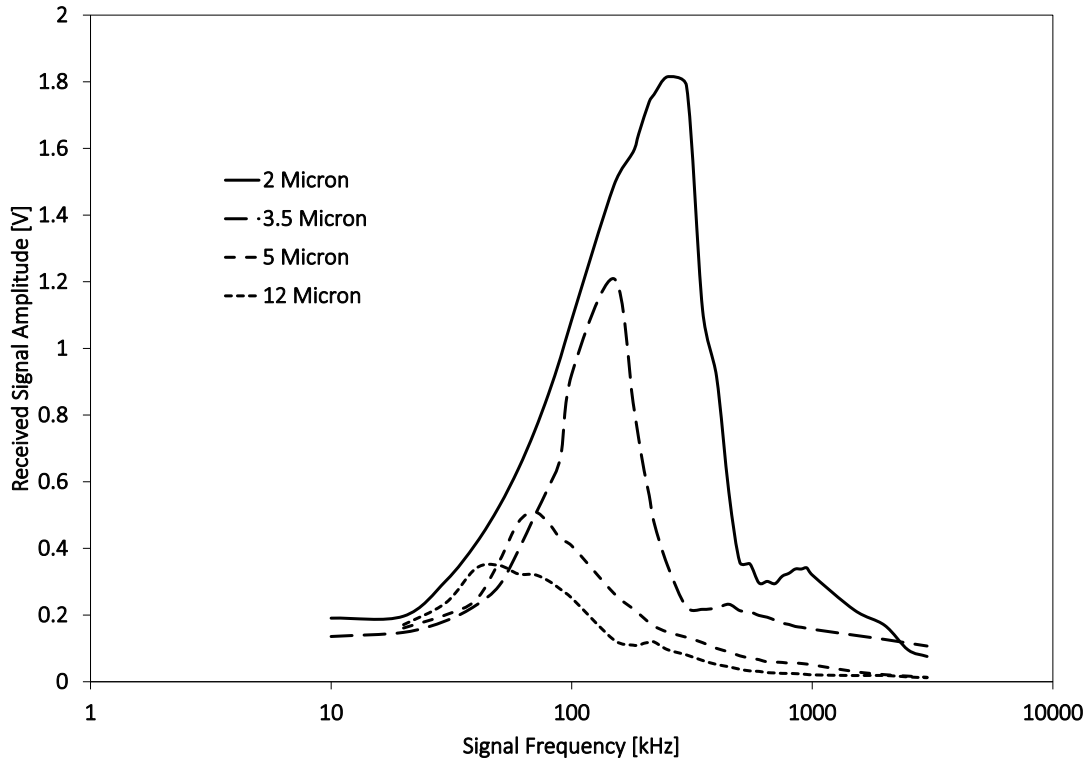


Fig. 3.14: Effect of film thickness on frequency response of the transducers (air, 1010 mbar)

As expected, the peak frequency of the transducers with thinner films was significantly higher than those with thicker films. However, comparing the peak frequencies and peak widths to their expected values yielded worse agreement (Table 3.4).

Film Thickness	Measured Peak Frequency	Theoretical Peak Frequency
2 μm	245 ± 10 kHz	249 ± 107 kHz
3.5 μm	160 ± 10 kHz	188 ± 81 kHz
5 μm	70 ± 10 kHz	157 ± 68 kHz
12 μm	50 ± 10 kHz	102 ± 44 kHz

Tab. 3.4: Comparison of measured and theoretical peak frequencies of different films in air at 1010 mbar (Equation 2.12). Data not taken at low pressure due to insufficient signal amplitudes.

The error range in the theoretical peak frequencies is primarily determined by the large uncertainties in backplane roughness (Figure 3.7) and membrane thickness (10% thickness tolerance specified). However, even with these large associated errors, the gas piston model only just predicts the peak frequencies to within experimental error. This could be because the theory was based on the gas-piston mode, but the thicker films may have been stiffer and so the frequency response may have been more dependent on the membrane stiffness than the size of the gas piston behind the film. Repeating the experiment with backplanes roughened with a more consistent procedure would allow for a better evaluation of the theory in predicting peak frequencies with different film thicknesses, by reducing the large errors associated with the backplane roughness.

Using Equation 2.31, the damping factor of each film was also calculated from the peak width and film mass. The quality factor of the different films was also evaluated (Table 3.5) using the same equation.

Film Thickness	Damping Factor b [kg/s]	Quality Factor Q
2 μm	$(1.09 \pm 0.15) \times 10^{-2}$	1.34 ± 0.20
3.5 μm	$(4.17 \pm 0.64) \times 10^{-2}$	1.90 ± 0.57
5 μm	$(6.67 \pm 1.09) \times 10^{-2}$	0.93 ± 0.38
12 μm	$(1.69 \pm 0.34) \times 10^{-1}$	0.70 ± 0.34

Tab. 3.5: Calculated damping and Quality Factors for each film (Equations 2.29, 2.31)

These results showed that the thicker films are much more heavily damped, as evidenced by larger damping factors and smaller quality factors. This is because the larger effective mass of the thicker films would have lower vibration amplitudes than the thinner films for a given excitation energy. The 12 μm films

have a quality factor quite close to the critically-damped state of 0.5, but all films are essentially under-damped. One observed disadvantage to using the thinner films, other than the undesirable higher peak frequencies, was that their under-damped behaviour could result in "ringing" of the output signal for a short time, with more (albeit smaller) peaks visible in the received signal than the transmitted signal. This phenomenon is discussed further in Section 4.3. It is interesting to note that, whilst the 3.5 μm films had the highest quality factor, they were not nearly as sensitive as the 2 μm films.

Testing confirmed that 2 μm films are the most suitable for use at low pressure (Figure 3.13). However, they are likely to be more prone to damage and their under-damped behaviour could cause "ringing" of the output signal if only transmitting at a single frequency.

3.7 Backplane Diameter

The last of the four parameters to be tested was backplane diameter. In order to investigate how the backplane diameter affected the transducer sensitivity, the received signal amplitudes were measured at low air pressures for backplane diameters ranging from 8 mm to 20 mm (Figure 3.15).

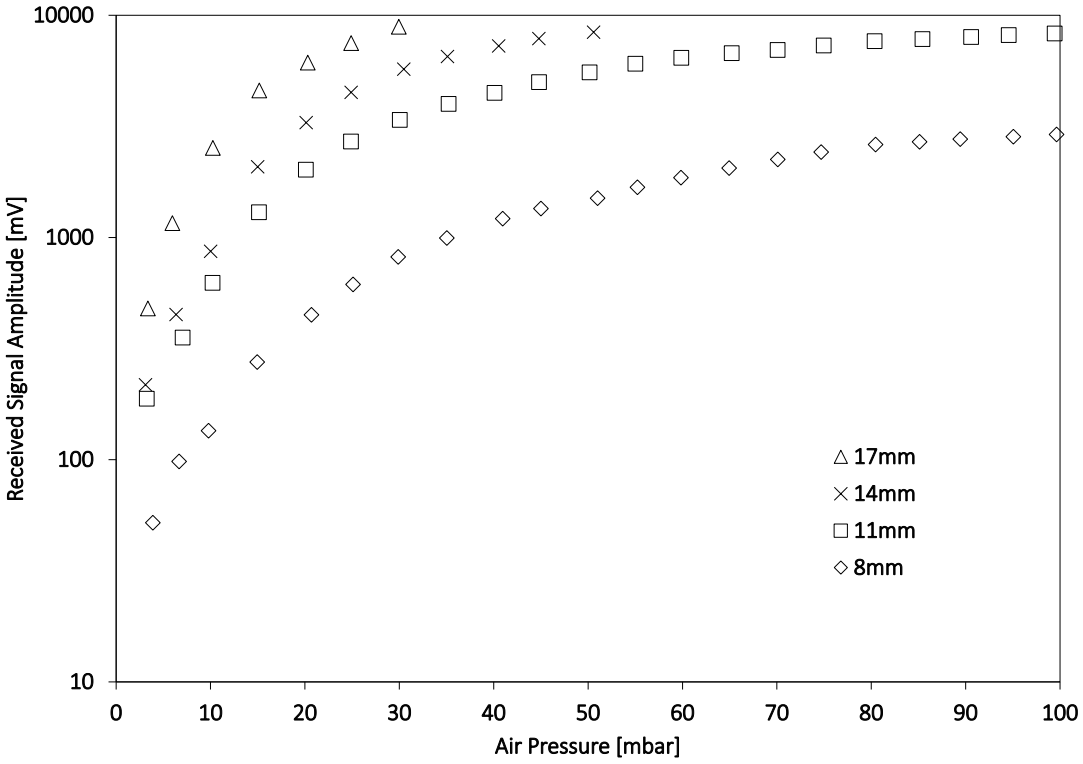


Fig. 3.15: Effect of backplane diameter on received signal amplitude at low air pressures (20 mm values omitted as mostly saturated)

To allow for a better comparison between expected and measured transducer sensitivity, neglecting amplifier saturation, the amplitude values were averaged over five pressures (3, 6, 10, 15, 20 mbar) and plotted against the theoretical expectation (Equation 2.69). These amplitude values are shown in Figure 3.16.

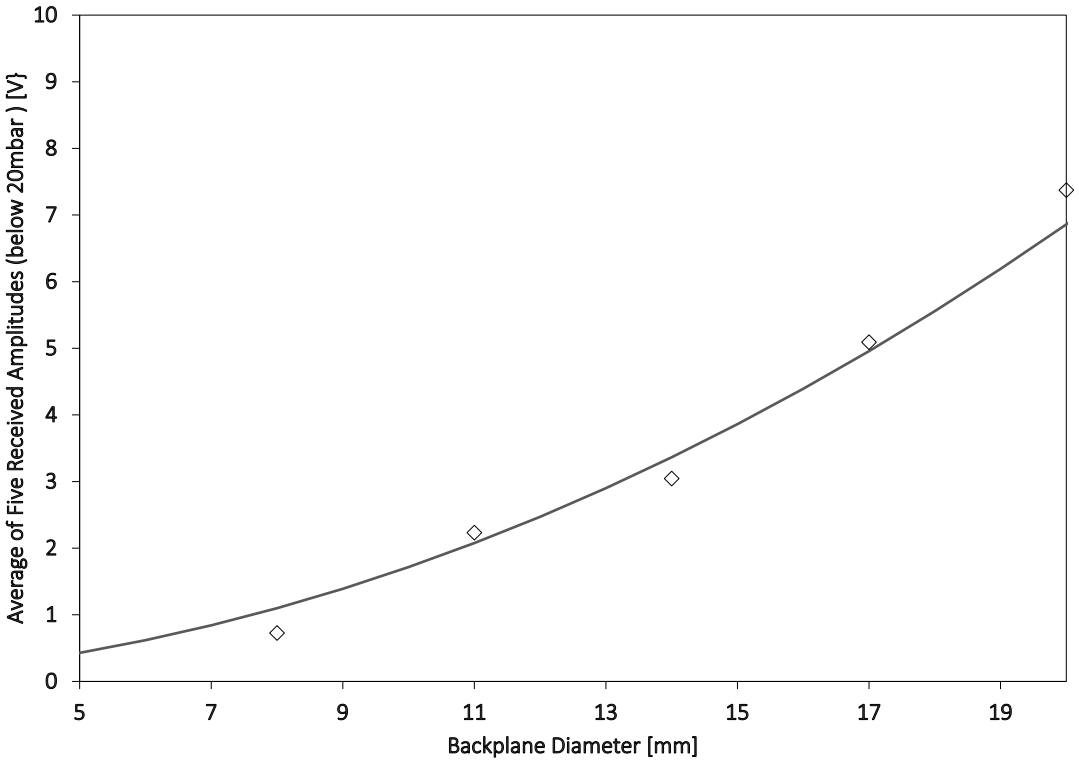


Fig. 3.16: Plot showing how measured received amplitudes compare with theoretical expectation for different diameter backplanes

The experimental results agreed with the theoretical expectations to within 30%. To confirm that the diameter did not affect the frequency response of the transducers, the frequency response of each diameter pair were measured at 1010 mbar, and the peak frequencies found to be equal to within ±3 kHz.

3.8 Low Pressure Frequency Response

To test how well the frequency response of the transducers was described by the gas piston model at low pressures (Equation 2.12), the peak frequency response of the transducers with 0.2 mm groove backplanes was evaluated at various air pressures (Figure 3.8).

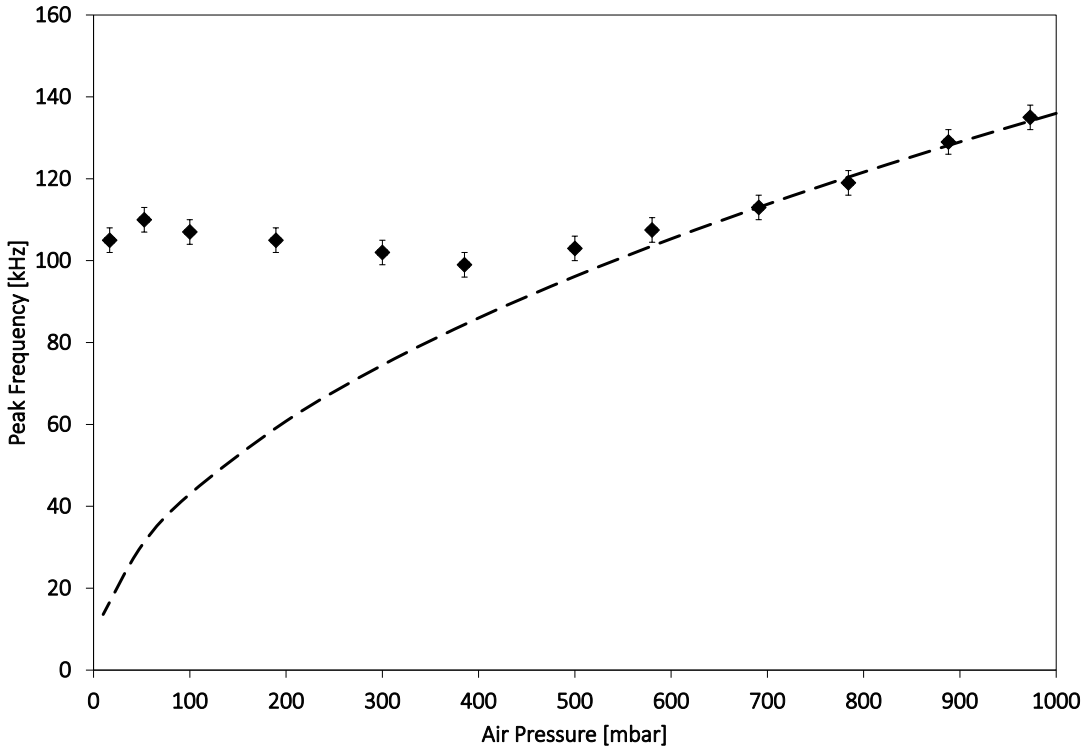


Fig. 3.17: Variation of peak frequency with pressure, compared to theory (dashed line)

The gas piston model was found to predict the peak of the transducer frequency response very well down to 700 mbar; but below that, it tailed off and largely remained constant. This behaviour suggests that, at low gas pressures, the stiffness of the membrane dominates the frequency response, which was constant with pressure. Since the operation of the transducers at low gas pressures requires the use of the thinnest films possible (Figure 3.13), the frequency response at low pressures will be largely independent of pressure, but not backplane roughness. The measured peak frequencies in a carbon dioxide atmosphere were approximately 20 kHz lower than in air at 1010 mbar, so using 2 μm films with the 0.2 mm grooved backplanes would give a peak frequency of approximately 90 kHz on Mars. This is very close to the ideal operating frequency of 85 kHz for maximum signal transmission on Mars (Figure 1.10).

3.9 Optimum Transducer Parameters

The data presented in this Chapter has demonstrated that transducer performance is generally very well modelled by the theoretical framework laid out in Chapter 2 (Table 3.6), with two notable exceptions.

Parameter	Expected Signal Dependence	Measured Signal Dependence
d_a	d_a^{-3}	$d_a^{2.13}$
V_b	$V_b^{2.04}$	$V_b^{2.10}$
d_m	d_m^{-2}	$d_m^{-1.86}$
D	D^2	$D^{2.23}$

Tab. 3.6: Comparison of predicted transducer amplitude behaviour (Equation 2.69) with measured parameter dependence.

Backplane roughness testing revealed that operating frequency choice has a significant impact on transducer performance. It isn't possible to simplify the dependence of received amplitude on backplane roughness as in Equation 2.69. However, the full theoretical model, incorporating different peak frequencies, was found to describe the transducer behaviour well (Figure 3.9). Peak received amplitudes for the optimum signal frequency on Mars are achieved using backplane roughnesses of 0.2 mm.

Increasing the bias voltage between film and backplane was found to greatly increase the received signal amplitude; however the dielectric constant of the Mylar films limits bias voltages to <60 V.

Of the four different film thicknesses tested, only the 2 μm films produced visible signals at 6 mbar in air. The theory predicted the peak frequencies of the transducers incorporating different film thicknesses, but only because of the large errors associated with the backplane roughness. Similarly, the theoretical framework was unable to accurately predict the transducer peak frequencies at air pressures below 700 mbar. This limitation of the model may be due to different relative variations in stiffness of the membrane and air gap with pressure.

To maximise received signal amplitude, the largest transducers possible must be used. Testing confirmed that transducer diameter has no appreciable effect on frequency response, as expected. However, instrument mission constraints of total mass and occupied volume will limit transducer diameters.

The optimum transducers for maximum signal transmission on the Martian surface are therefore large diameter transducers incorporating 0.2 mm roughness backplanes, 2 μm films and 60 V bias between film and backplanes. The transducers under investigation have been verified as capable of operating at Martian pressures in air, and at frequencies required for minimising signal losses to the Martian atmosphere. As has already been established, transducers which work in air at Martian pressures should perform better in CO_2 at the same pressure (Section 1.4). The next Chapter will investigate factors affecting instrument performance; particularly in terms of wind speed measurement under Martian conditions and whether they are capable of meeting the science requirements set out in Chapter 1.

4. INSTRUMENT TESTING AND OPTIMISATION

Chapter 1 established the need for improved anemometry data from the Martian surface; and why capacitive transducers were suitable candidates. Chapter 2 went on to describe how the transducers work theoretically, and these theoretical predictions were verified in Chapter 3 to obtain the optimum transducer parameters for maximum signal transmission under Martian conditions (0.2 mm roughness backplanes, 2 μm films and 60 V bias). In this Chapter, two important instrument parameters are validated: the beam pattern and change in received signal amplitude with transducer distance, to complete the analysis of parameters contained in Equation 2.69. The effectiveness of the whole instrument at measuring wind speed will then be evaluated under simulated Martian conditions.

4.1 Beam Pattern

The transducers were placed 9 cm apart to investigate the shape of the acoustic beam pattern; one was secured in place whilst the other was moved horizontally across the beam in line with a ruler. All other test conditions were as described in Table 3.2. Every 1 mm across, the received signal amplitude was averaged over 200 samples by the oscilloscope. The process was carried out for signal frequencies of 100 kHz and 50 kHz, and the results plotted in Figure 4.1.

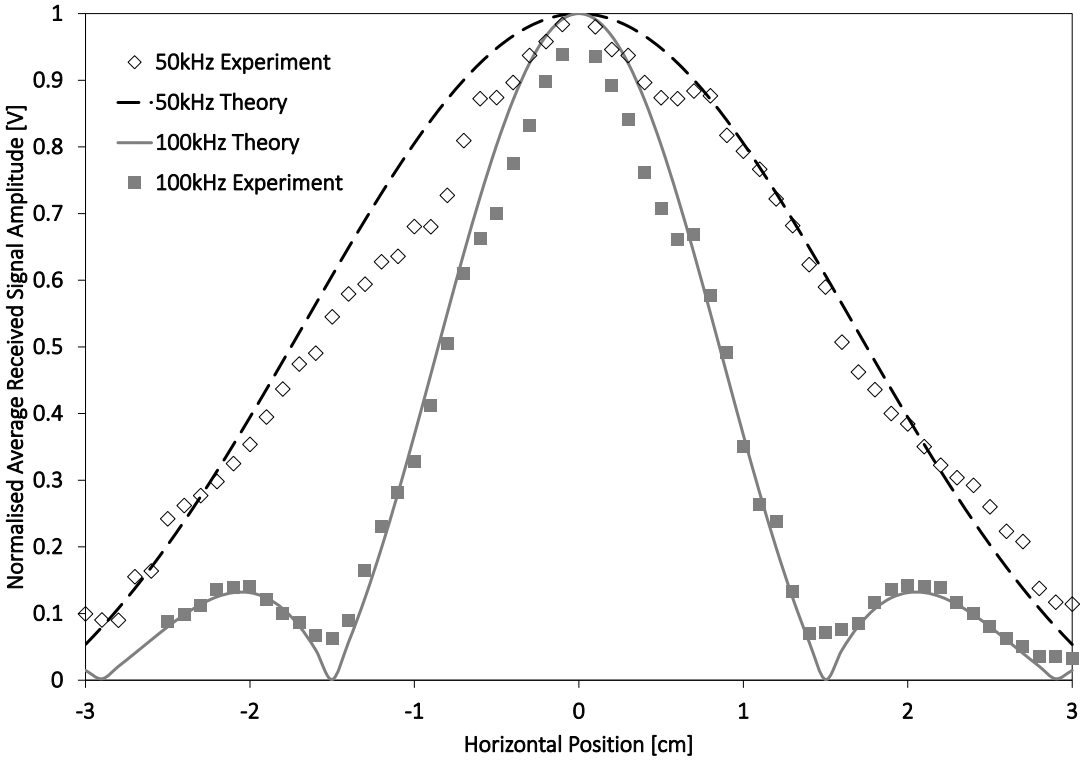


Fig. 4.1: Effect of signal frequency on beam pattern, compared to theoretical predictions. Maximum amplitudes normalised to 1 V for clarity.

As predicted by Equation 2.56, higher signal frequencies produce much narrower beam widths, as beam spreading is reduced. The experimental data fit the theory quite well, except towards the central position where the received amplitude was less than the theory for both frequencies. This was likely due to the random nature of the backplane profiles. Whilst it is beneficial to use higher frequencies for reduced beam spreading, there is a trade-off between beam spreading and attenuation losses (Figure 1.10). Additionally, higher frequencies allow for more pulses per signal and shorter separations so ultimately, exact frequency selection will be dictated by mission constraints.

4.2 Transducer Separation

Whilst possibly not as important as the factors investigated in Chapter 3, transducer separation still has an effect on received signal amplitude. To test the variation in received signal amplitude with transducer separation, the transducers were moved apart, aligned and then the average of the received signal amplitude calculated over 200 samples on the oscilloscope. For this test, the transmitted signal amplitude and bias voltage were reduced to 35 V and 30 V respectively, to ensure there was no signal clipping. The signal frequency was kept constant at 100 kHz.

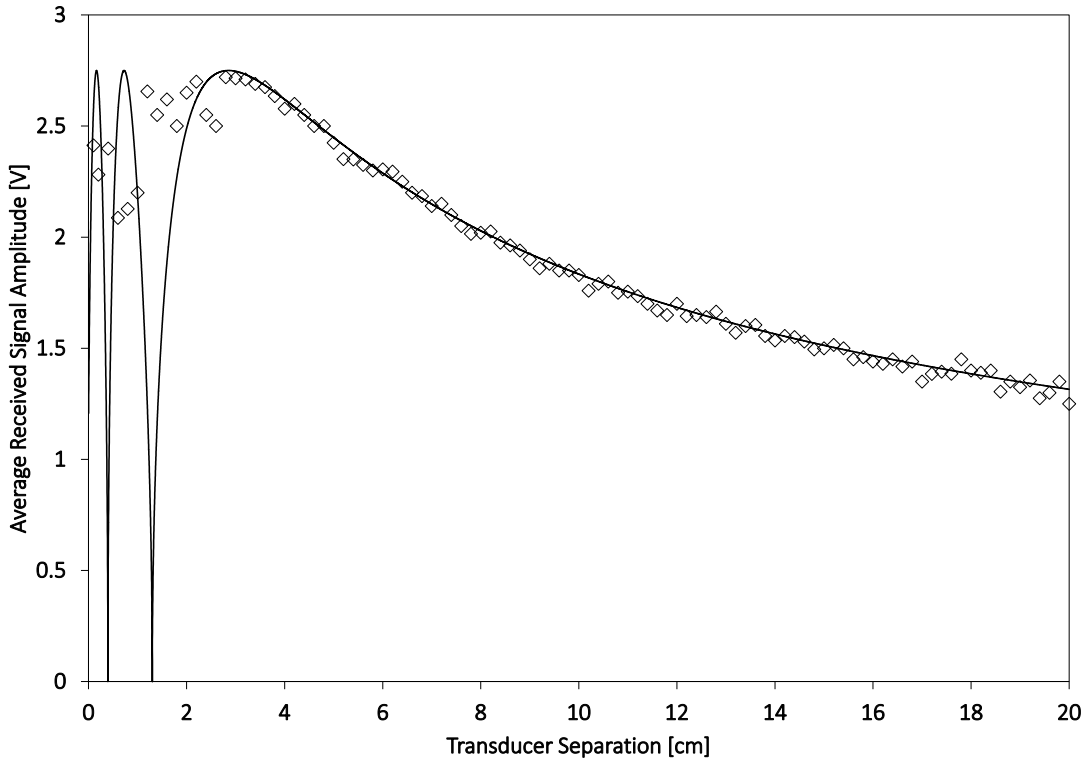


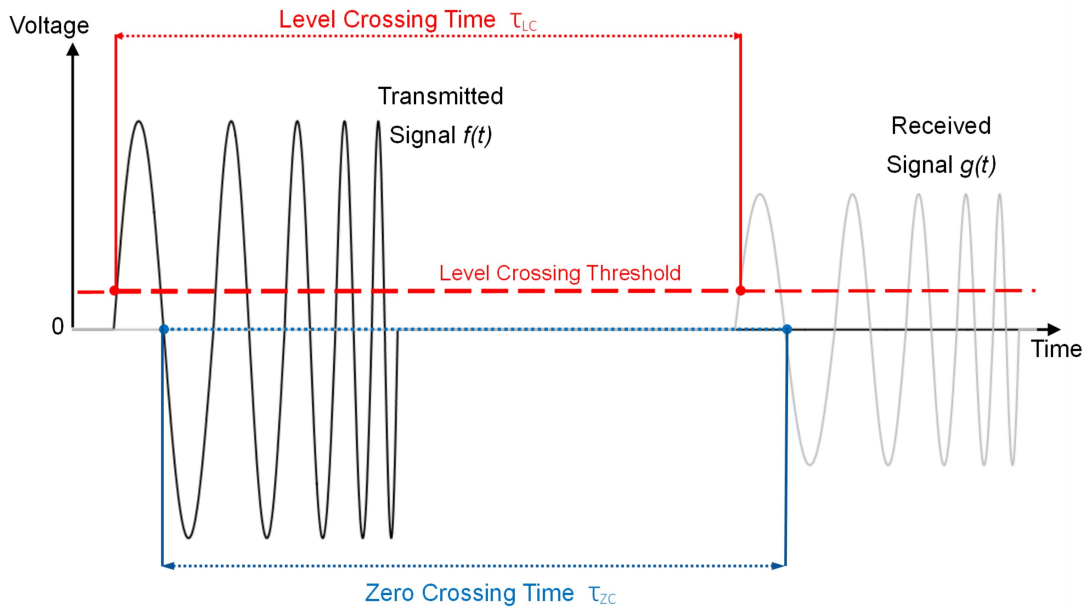
Fig. 4.2: Effect of transducer separation on received amplitude, including theoretical prediction (black line). Natural focus calculated to be 2.94 cm using transducer parameters

The measured attenuation with distance matches the experimental expectation (Equation 2.58) in the Fraunhofer zone (>2.94 cm). At higher separations there

was higher variability from the predicted value; probably due to the greater impact of misalignment on the results since, as transducer separation is increased, any errors in correctly aligning the transducers have a greater impact on the proportion of the transmitted beam which is received.

4.3 Signal Shapes and Detection Methods

The two primary signal detection methods used in acoustic anemometry are level-crossing and cross-correlation. Level-crossing uses a clock to determine the time between the points where transmitted and received signals are first above certain thresholds (Figure 4.3). One particular type of level-crossing, zero-crossing, is where the threshold level is set at zero volts. Since these techniques only require one reference point on the transmitted and received signals, the exact shape of the signal does not make any difference. Level-crossing requires only simple electronics, but its accuracy is reduced as more noise is introduced into the signals.



Cross-Correlation Time $\tau_{CC} = \arg\max_{\tau} \left[\int_{-\infty}^{\infty} f^*(t)\ g(t+\tau)\, dt \right]$

Fig. 4.3: Illustration of the three signal detection methods

Cross-correlation involves a convolution of the transmitted and received signals; such that the difference in number of samples where the correlation between them is the greatest equals the travel time. Cross-correlation requires an ADC for digitisation of the signal and is more computationally intensive than level-crossing, but at the same time allows for the travel time to be calculated even when the signal is hidden in the noise. This is possible because the transmitted and received signals are the same shape; and is a key advantage to cross-correlation as it would negate the impact of dust deposition, and allow data collection under a much wider range of conditions. The added complexity of cross-correlation over level-crossing would add power and mass requirements to an instrument, but this slight increase in device requirements is more than offset by the powerful capabilities of cross-correlation.

Four different signal shapes, using both frequency modulation (chirped) and amplitude modulation (windowed) pulses, were investigated to determine which performed best using cross-correlation at low received signal amplitudes. Hamming windows, commonly used in applications where high SNRs are required, were chosen to modulate the signal amplitude. These windows allow for easier identification of received signals due to the central peak, especially if the received signal exhibits "ringing" behaviour. Theoretically, chirped signals should have narrower peaks than windowed ones due to the range of excitation frequencies present.

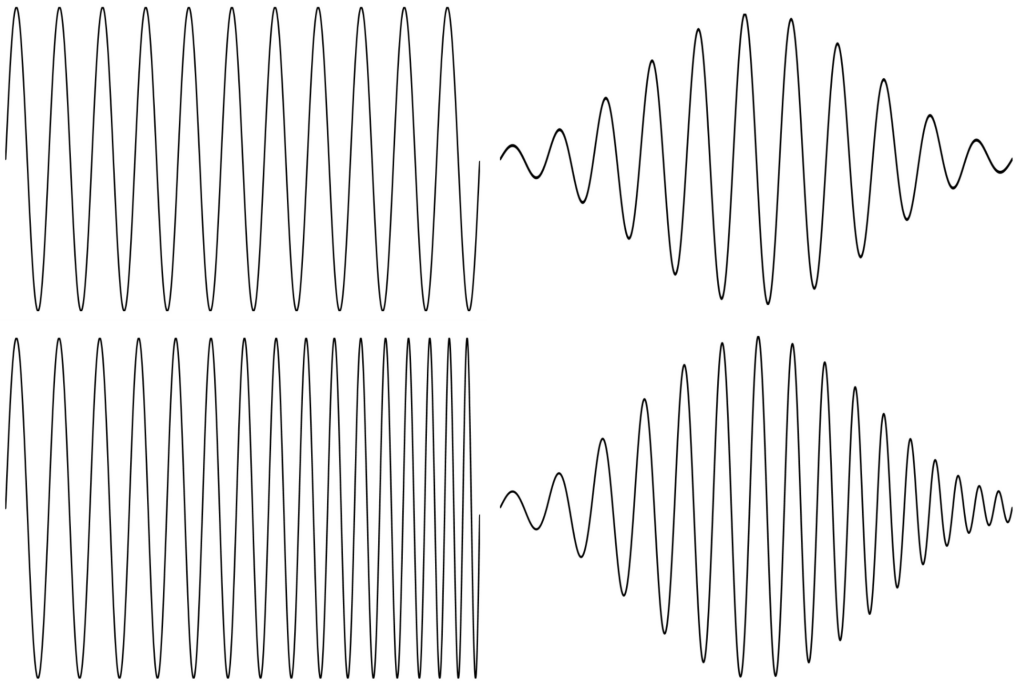


Fig. 4.4: The four different signal shapes under investigation. Signal A (top left): standard pulse train, Signal B (top right): Hamming window of Signal A, Signal C (bottom left): chirped pulse train, Signal D (bottom right): Hamming window of Signal 3. Though axes have been omitted for clarity, the plots are of voltage against time.

The waveform generator only allowed the starting frequency of each signal to be specified, so all signals started with the same initial frequency (100 kHz) and were exactly the same length (110 μs). One benefit of the chirped signals during initial testing was the lack of observed "ringing" of the output signal, so the received and transmitted signal lengths were equal. No signal averaging was used for any tests involving signal detection so as not to negate the noise resilience of each method, and because it would significantly reduce instrument operating frequency.

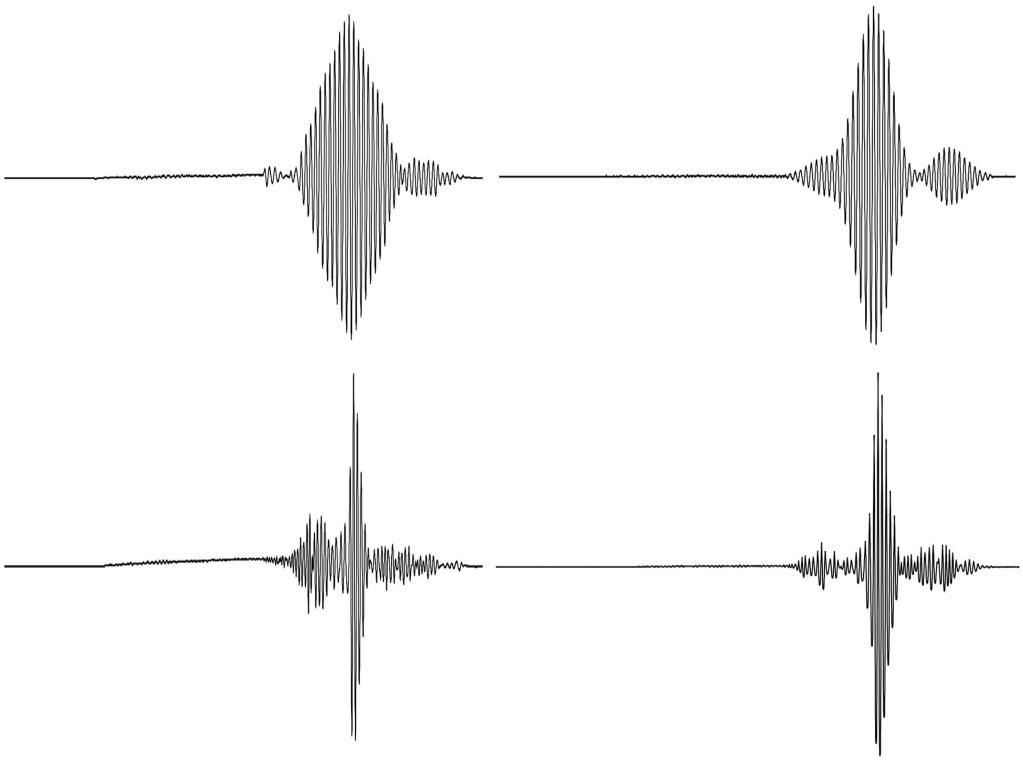


Fig. 4.5: Cross-correlation results (air, 1010 mbar) of the four signals under investigation. Axes have been omitted for clarity and the plots show the result of cross-correlation against number of samples.

Whilst the cross-correlation results of all four signals agreed on the location of the peak (Figure 4.5), there was a large variation observed in peak width and, therefore, the certainty in peak location. To obtain the peak widths, the cross-correlation results were passed through a Hilbert filter [68] to produce an envelope of each result. The amplitudes were then normalised and the half-widths of each peak found to be 749, 554, 56 and 97 samples wide respectively for Signals A-D. Given that the peak was located at 2488 samples, the correlation results of Signal C gave the most precise location of the peak and, as expected, chirped pulses are more accurate than windowed ones. Each sample was 0.12 μs apart, so the Signal C peak width equated to a wind speed error of 0.1 ms^{-1} using an 8.5 MHz sampling rate.

The accuracy of the cross-correlation result is dependent upon the SNR and timing resolution of the ADC used. Whilst it was clear that Signal C performed best on Earth, where the signal amplitudes are large, the test needed to be repeated with smaller signal amplitudes to simulate Martian conditions. However, when the experiment was repeated in air at 3 mbar, the SNR was still sufficiently high to obtain reliable cross-correlations without signal averaging and did not allow for a comparison. The cross-correlation results were seemingly independent of air pressure. To ultimately determine which signal produced the most reliable results at low signal amplitudes, the test was carried out at room pressure, but varying the input signal voltage down to zero and obtaining cross-correlation results every 0.5 V. Signals A and B lost cross-correlation signals at >10 V; whereas Signals C and D worked down to 5 V and 6 V respectively. Thus Signal C gave cross-correlation results at a slightly lower

voltage than the others, but not much lower than Signal D. Signal D is a Hamming-window of Signal C so it makes sense that Signal C, with a larger overall amplitude, performed slightly better at low signal voltages.

For instrument operation at low SNR, these tests have shown that a chirped, non-windowed signal gives optimal performance; both in terms of wind speed accuracy (peak width) and being able to use lower signal voltages. Signal C was further refined to be used at frequencies as low as 10 kHz by shortening it to 5 cycles; but with much greater frequency differences between successive peaks in the sequence. Each successive sinusoid in this optimised signal is 1.4 times the frequency of the previous one, so an initial frequency of 100 kHz would give a maximum signal frequency of 384 kHz. This optimised signal (shown in Figure 4.3) was used for all subsequent tests, including analysing the different signal detection methods in the wind tunnel under Martian conditions (Section 4.4).

4.4 Wind Tunnel Testing

Investigating instrument performance at low pressures in carbon dioxide and in a dusty environment was necessary to validate wind speed measurement under these conditions, and to determine what impact dust deposition may have on transducer operation. Two wind tunnel facilities were used to test the transducers (Figure 4.6). Their schematics can be found in Appendix C.

4.4.1 Wind Tunnel Specifications

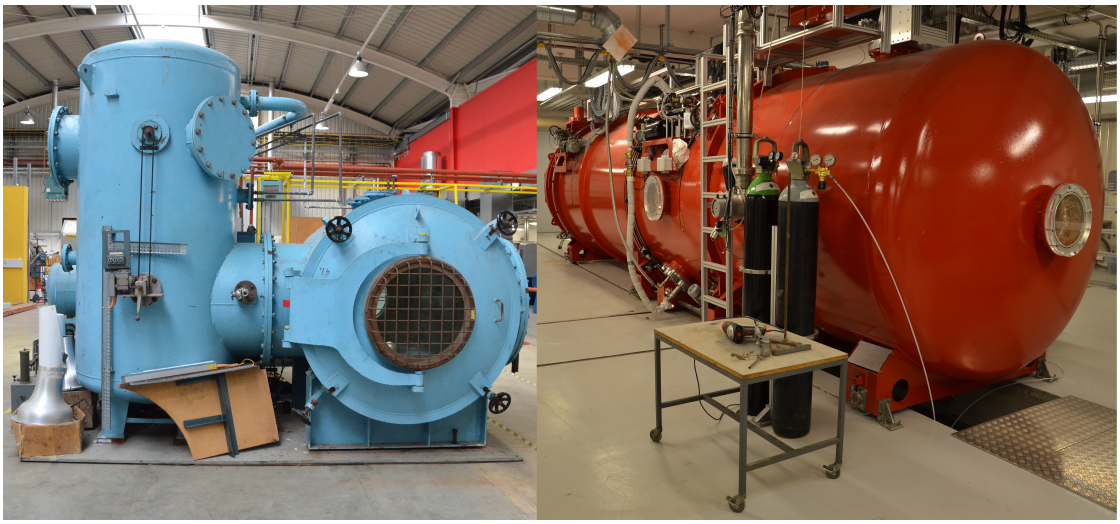


Fig. 4.6: The LDWT [69] (left) and AWTS [70] (right). For scale, the test chamber diameters are roughly equal at the two facilities.

The Oxford Low Density Wind Tunnel (LDWT) was used to test the performance of the transducers measuring wind speeds at low air pressures. The Aarhus Wind Tunnel Simulator II (AWTS II) allowed further testing at low pressures in carbon dioxide with airborne Mars analogue dust. Their operating specifications are compared in Table 4.1.

Specification	LDWT [69]	AWTS [70]
Operation	Open circuit	Closed circuit
Test Section Dimensions [m]	1.5x1.5x1.5	2x2x1
Test Atmosphere	Air*	Air or CO_2
Temperature	Room*	153 - 353 K
Pressure	5 - 1000 mbar	0.07 - 1000 mbar
Wind Speed Range	0.5 - 30 ms^{-1}	0.8 - 18 ms^{-1}
Wind Turbulence	<1%	10 - 18% (no mesh) <2% (double mesh)
Dust	No	5 minute suspension, <2 g/min

Tab. 4.1: Comparison of wind tunnel specifications. *The LDWT can be setup for CO_2 and low temperatures, but was not configured for these conditions as it had recently been relocated

Whilst the two wind tunnels are similar in many ways, they also have key differences. Principally, the LDWT is better for calibrating wind sensors as the wind speed is calculated from sensors in real-time, its flow is much better characterised and it has been designed for laminar flow. The AWTS, however, has only been calibrated at six pressures and a single temperature; but if dust is being used there is also a Dantec Dynamics FlowLite Laser Doppler Anemometer (LDA) for measuring exact particle velocities in two dimensions. The benefits of the AWTS include simulation of a carbon dioxide atmosphere and airborne dust.

4.4.2 Procedure

The test procedure for wind tunnel testing was slightly different from the tests evaluating transducer performance with different components. The same electronics were used; and BNC pass-throughs connected the transducers inside the tunnel to the test electronics outside the chamber. Whilst not the most sensitive transducer setup, due to a technical error, the 20 mm diameter 4.9 μm backplanes and 2 μm films were used in both wind tunnels to enable a comparison of the two facilities. The transmitted signal was a 5-cycle chirped pulse with a frequency range of 100-384 kHz (Figure 4.3). A Picoscope 2207 oscilloscope was used for viewing and storage of the sent and received signals. Once the tests had been completed, the files created were imported into a custom Labview program; which filtered out the received signal through a 10-500 kHz band-pass software filter before performing cross-correlation and level-crossing analysis on the data. The software filter was used to reduce the impact of acoustic, mechanical and high-frequency noise in the received signals;

the cutoff values were chosen to minimise noise whilst still allowing the signal to propagate. Although it was convenient to implement the filter in software for testing, any flight hardware would use an electronic band-pass filter to minimise the required computation power. A zero wind speed time-of-flight value was obtained from the average of 100 acquisitions with no flow, and this value was used to calculate the other wind speeds from the timing differentials. Laminar flow was achieved in both wind tunnels through the use of multiple fine meshes upwind of the test section. The dust used at the AWTS was a typical Mars analogue (Salten Skov I), a local magnetic iron oxide precipitate approximately 1 micron in diameter [71].

4.4.3 CFD Modelling and Transducer Shadowing

Since the flow of gas past the transducers has to pass around the transducer heads, they themselves alter the flow, which therefore changes the measured wind speed between the transducer pair. To investigate this effect further, a series of tests were performed and compared with Computational Fluid Dynamics (CFD) simulation results.

A vertical 2-D grid of particle velocities, in the plane of the acoustic signal, was measured by the LDA at the Aarhus facility. The transducers were aligned parallel to the flow, for maximum shadowing effect, and the LDA took wind speed measurements for 20 s every 5 mm; covering the whole area between the transducers. Since the LDA requires particles to measure the wind speed, 2 g of Mars analogue dust were injected every half hour, timed to coincide with measurements at the periphery of the measured area. This ensured that the vital

data in the middle of the flow were not affected by excessive amounts of dust.

To verify the wind speed readings recorded by the acoustic transducers, Autodesk Simulation CFD 2014 was used to model the different fluid flows around the transducers for the various incident wind speeds, using the CAD files from which the transducer heads were manufactured. The wind tunnel chambers weren't included in the CFD modelling as they would have added significantly to the processing time required for a comparatively very small increase in result confidence, due to the large size of the chambers. The software also calculated the average wind speeds perpendicular to the transducers, in a cylindrical region bounded by the backplanes (10 mm radius). The simulation included three cycles of mesh adaptation before converging on a solution, usually within 500 iterations. The virtual test environment was validated by simulating fluid flow through a cylindrical pipe; the results were found to match Hagen-Poiseuille flow to within 2%. The software was used to model the same conditions in the test section measured by the LDA (3.5 ms^{-1}, 7 mbar, CO_2, 20.4 °C, turbulent flow); and was run with adaptive meshing three times, to optimise the mesh density, before converging on a steady-state solution. The model contained 606,342 nodes, included turbulent flow and converged in 670 iterations. The adaptive mesh results are included in Appendix D.

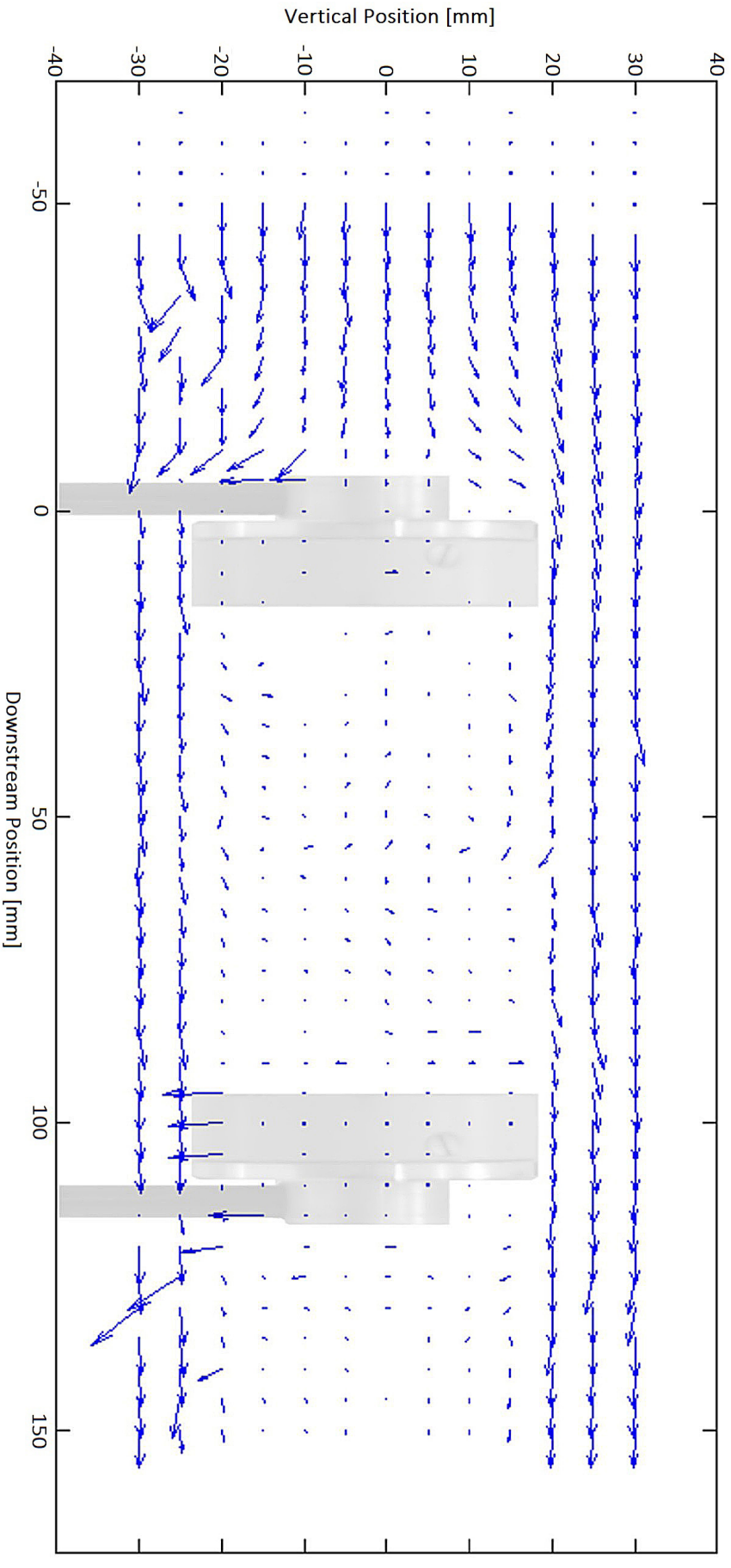


Fig. 4.7: Vector plot showing dust particle velocities from the LDA, including approximate transducer locations (to scale), for a 3.5 ms^{-1} incident wind speed. Erroneous results below the transducers were caused by the LDA passing over wires and other supporting structures. Note that the axes are not 1:1 due to the dimensions of the measured area.

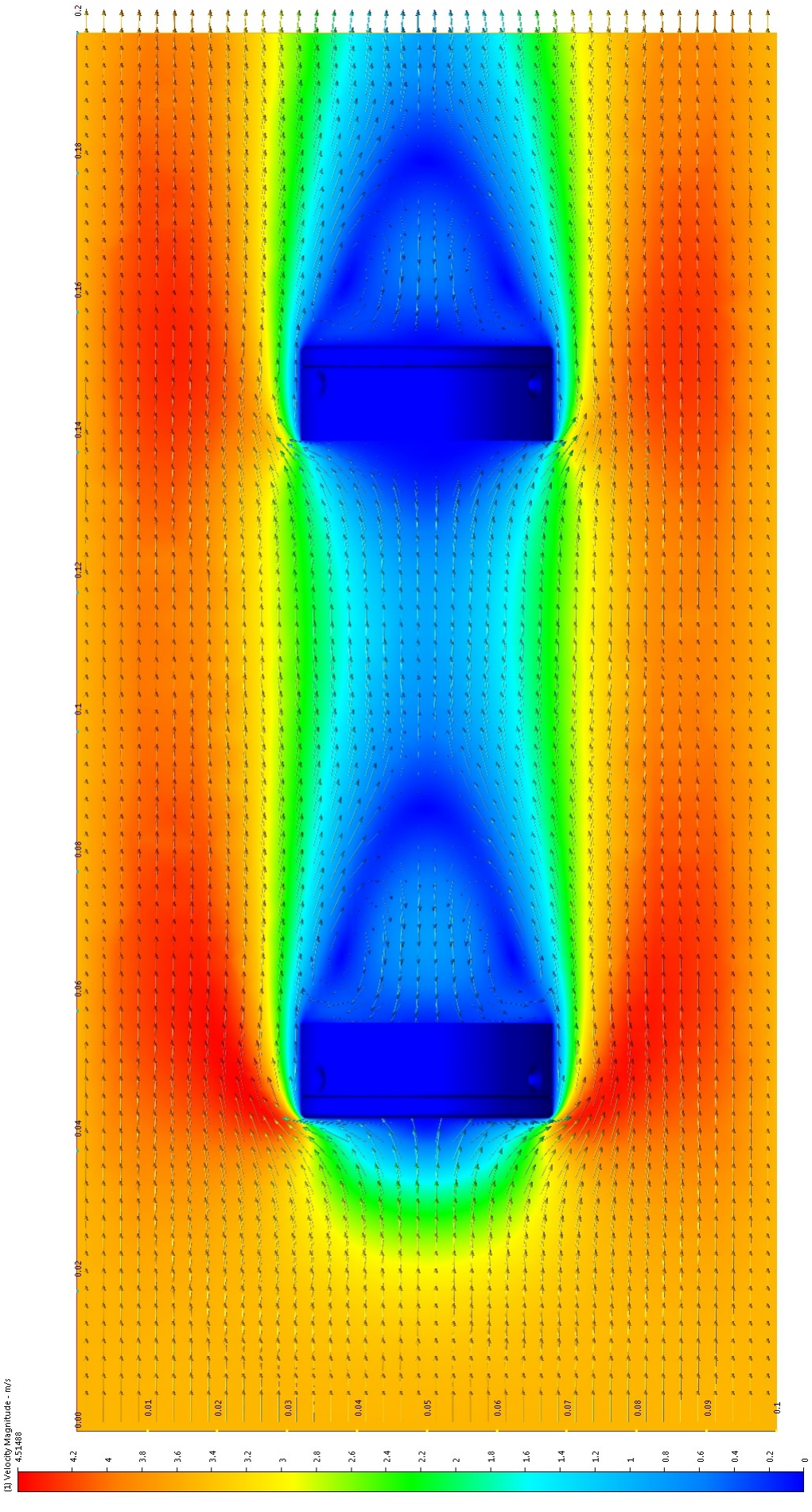


Fig. 4.8: Results from CFD analysis of the transducer shadowing effects parallel to the flow. Environmental conditions are identical to Figure 4.7 and axes are scaled 1:1 in metres.

The CFD model matches the experimental data to within ± 0.6 ms^{-1}. There was a significant decrease in wind speed in-between the transducers and also visible eddies behind each transducer head. The erratic long vectors in the experimental data were caused by reflections from solid objects such as wires, supporting rods and the transducers themselves. There was a general upwelling trend in the experimental data not seen in the CFD model; the mean vertical velocity component averaged in the area between the transducer heads was 0.2 ms^{-1}. This was likely due to wind being deflected upwards from supporting structures beneath the transducers, or the boundary layer inside the chamber. As previously stated, only the flow around the transducer heads was modelled in CFD, and not the supporting structures. The erroneous zero velocities measured upstream of the transducers were a result of the LDA reaching the viewing limits of the porthole and some of the beams being blocked (see Figure 4.9).

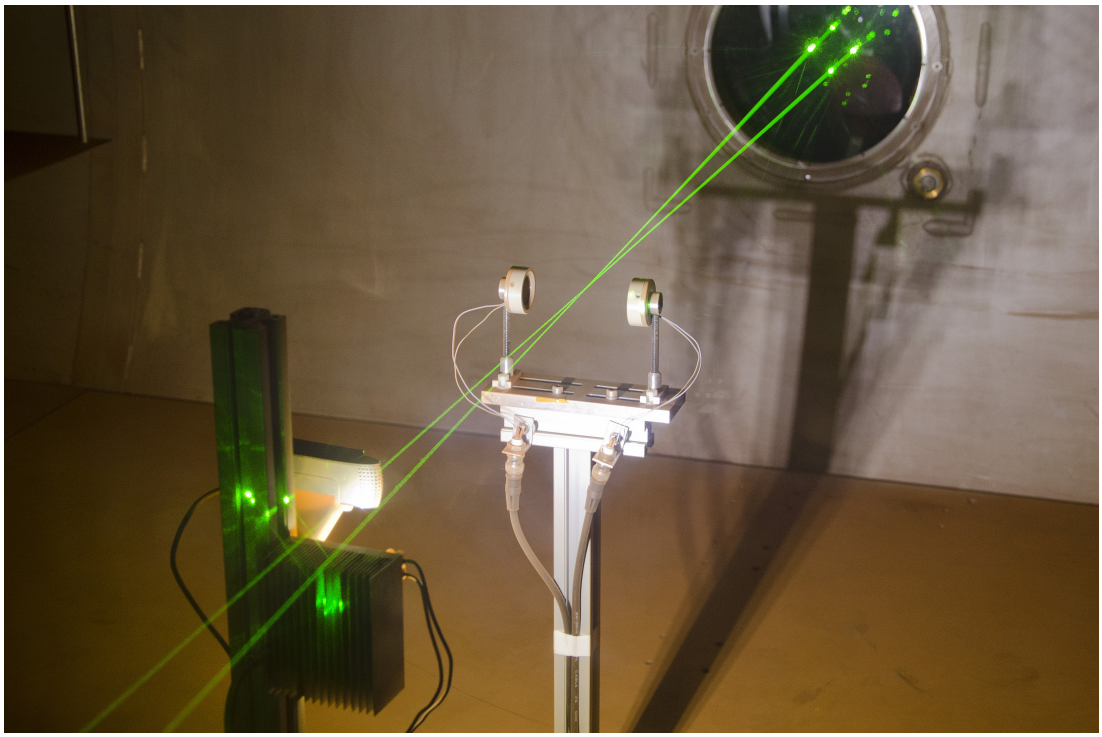


Fig. 4.9: Photograph of the LDA measuring the shadowing effect between the transducers at the AWTS facility

To further investigate the effect of incident flow angle on the wind speed measured by the transducers, the AWTS was run at three different wind speeds and the transducers slowly rotated in the flow whilst measuring the acoustic transducer signals at 10 Hz. This test was carried out in CO_2 at 7 mbar with double meshes (laminar flow) and no dust. The rotation angle and wind speed measured by the transducers were correlated by timestamps in the data. The rotation was performed in both directions and the data averaged to remove hysteresis (Figure 4.10). An offset of 6° in the angle measurements, which could not be attributed to timestamp errors, was corrected for in the results.

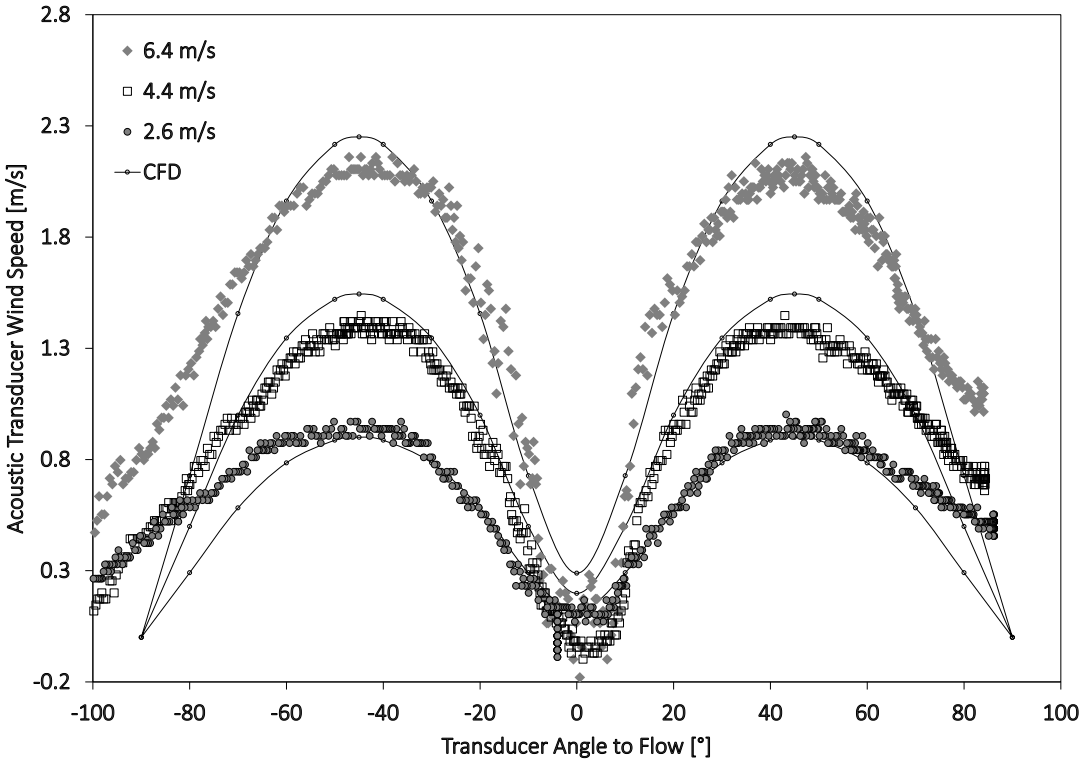


Fig. 4.10: Plot detailing how the incident wind speed angle affects the measured wind speed by the transducers at three different wind velocities.

Though the general shapes of the experimental data and CFD simulations are very similar, the experimental results departed from the modelled behaviour when angled more than 60° to the flow. This may have been due to circulation

patterns caused by the wind tunnel walls and transducer supporting structures; which were not modelled and could result in the small observed wind speeds perpendicular to the flow direction.

An instrument would be able to distinguish between positive and negative angles of incident wind speed through two pairs of orthogonal transducers. However, since the transducers would measure two different angles of incident wind speed for a given measurement, it would not be possible to accurately determine the actual incident wind speed angle using a single pair of these transducers. Accurate calculation of the wind speed angle would be possible using concurrent measurements from two or three transducer pairs in an orthogonal arrangement. Whilst the transducers were reliable at measuring varying uni-directional wind speeds at an angle of 45° to the flow (Section 4.4.4), further investigation into how to minimise shadowing was required. The prototype 14 mm flight-like Oxford transducers were therefore also modelled in CFD under Martian conditions (7 mbar CO_2), and the shadowing effects evaluated at different wind speed angles for the same separation (Figure 4.11).

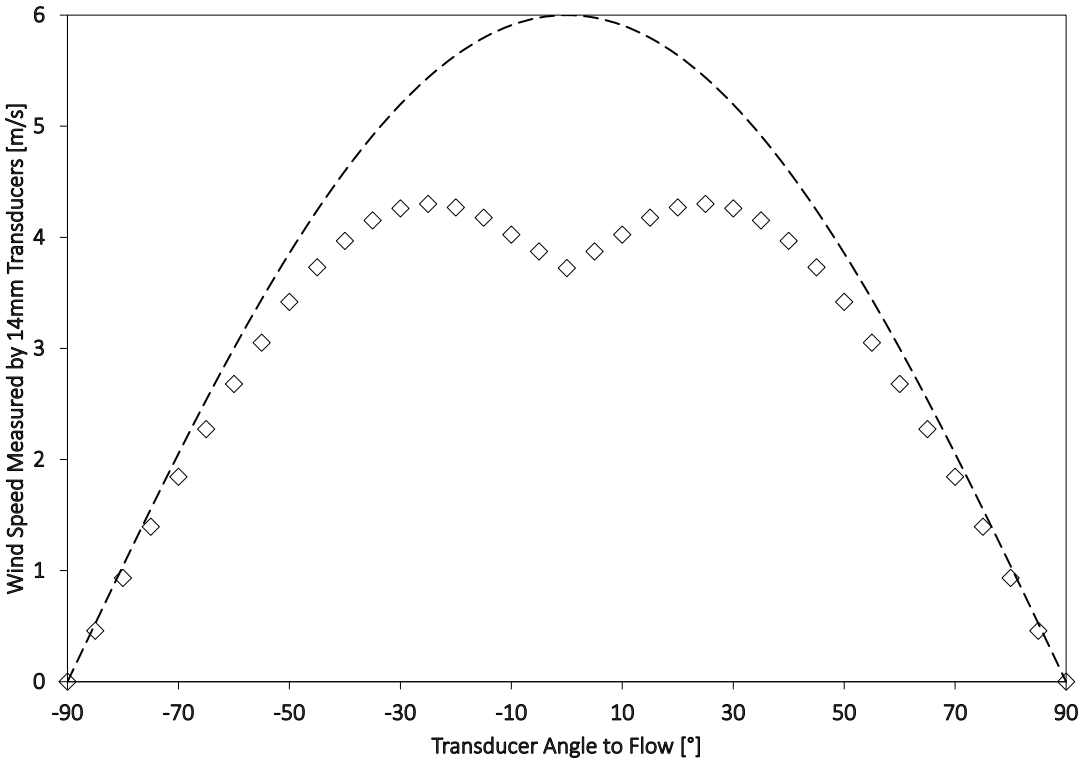


Fig. 4.11: CFD predictions of wind shadowing for the 14 mm flight-like transducers. The dashed line shows the expected cosine relationship between measured speed and angle of incidence for no shadowing effects

The data plotted in Figure 4.11 confirmed that the smaller flight-like Oxford transducers resulted in significantly less shadowing than the larger ones. They gave a much closer result to the expected ideal cosine relationship; but also exhibited noticeable shadowing when the flow was within 40° of the measurement axis. The shadowing error was never more than 38% of the incident wind speed and the measured speed was closer to the expected speed at greater incidence angles. Whilst the 14 mm Oxford transducers were a significant improvement on the larger ones used for testing, they were still not suitable for uniquely determining the angle of incident fluid flows using a single pair of transducers. Further CFD testing revealed that the shadowing effect could not be avoided, only minimised. The amount of shadowing relative to the incident wind speed for different diameter transducers was used to calculate the

angles over which it would not be possible to uniquely determine the incident wind angle; giving the maximum error in wind direction (Figure 4.12).

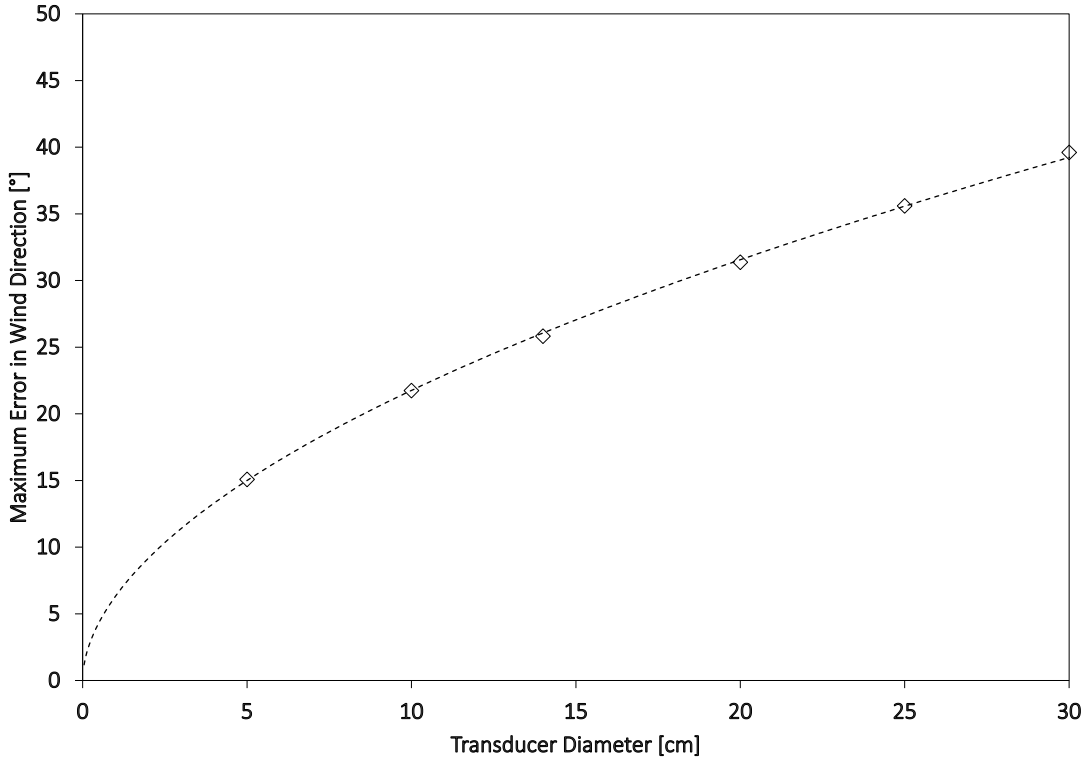


Fig. 4.12: CFD prediction of how backplane diameter affects the error in wind direction, including a power law fit to the data. Simulation conditions: CO_2 atmosphere, 7 mbar, 6 ms^{-1} incident wind speed, 10 cm transducer separation

This confirmed that, no matter how small the transducer diameter, there would always be some discrepancy to the incident wind speed due to shadowing. Even with a transducer diameter of 5 cm, the wind speed direction could only be accurately determined to $\pm 15°$. Since the theoretical angular distribution is a cosine relationship, and the maximum discrepancy between the measured angle and cosine expectation is at zero degrees, there will always be two angles for a given incident wind speed for a single pair of transducers, and shadowing cannot be avoided. However, if two or three pairs of transducers are in an orthogonal arrangement, it is possible to calculate the incident wind angle if the wind measurements are concurrent.

4.4.4 Calibration

The linearity and accuracy of the transducers in measuring wind speed was evaluated at both the LDWT and AWTS facilities. The anemometer's acoustic path was angled at 45° to the flow and the tests run at 13 mbar (air) and 7 mbar (CO_2) respectively. The effect of transducer shadowing at this incident wind speed angle is illustrated in Figure 4.13.

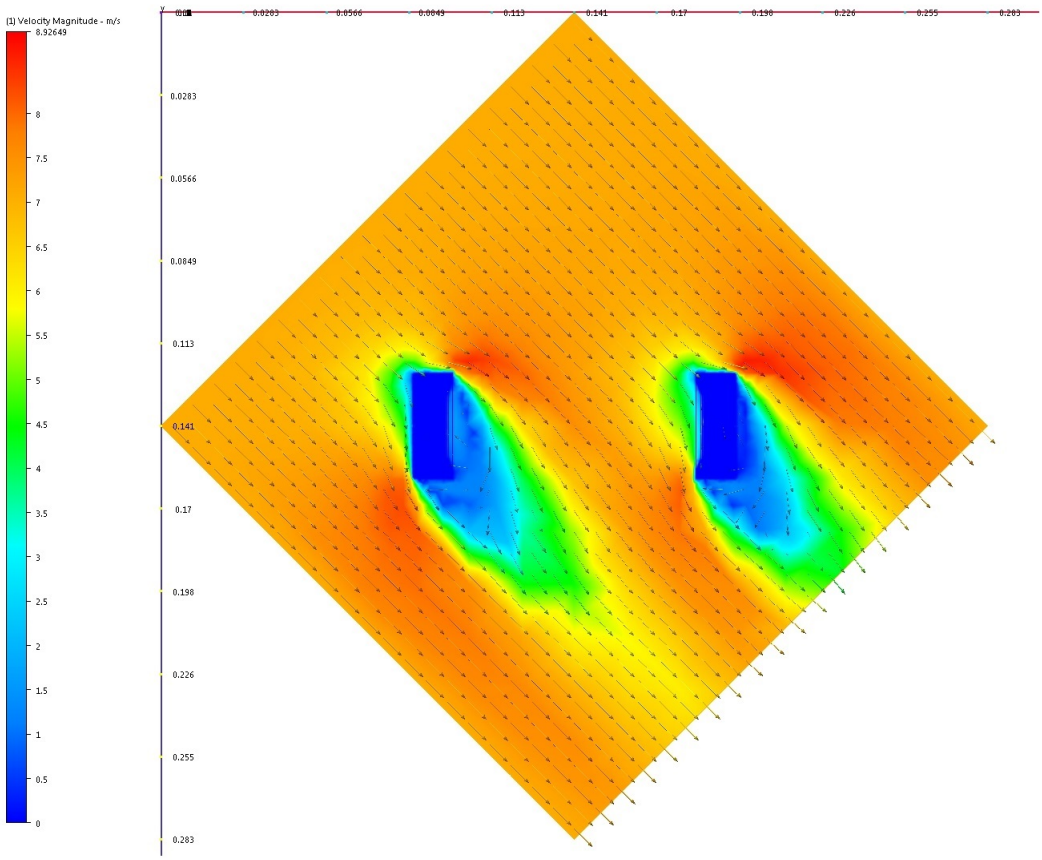


Fig. 4.13: Simulated transducer shadowing at the AWTS, at 45° to the flow (7 ms^{-1}, 7 mbar, CO_2)

The incident wind speeds were varied and upstream meshes implemented to ensure laminar flows. The acquired signals were also used to compare the effectiveness and accuracy of the different signal detection methods.

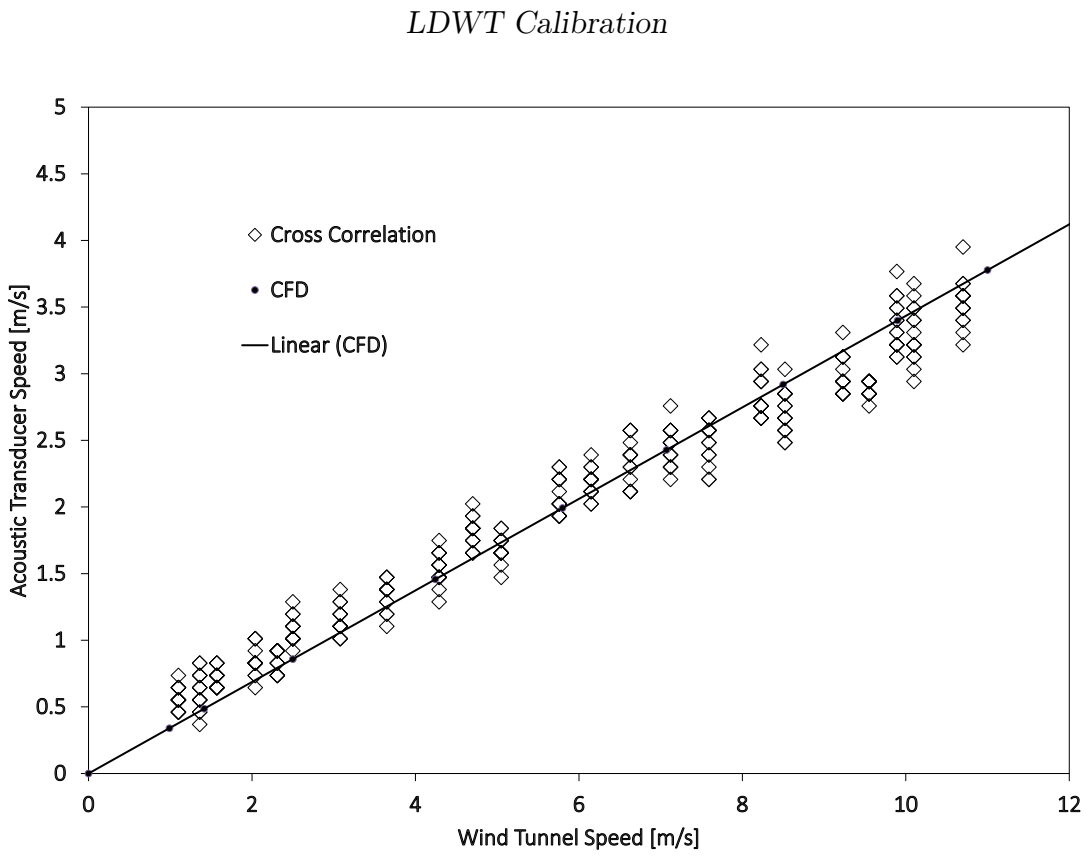


Fig. 4.14: Calibration plot of the acoustic transducers in the LDWT showing cross-correlation results of 15 single, unaveraged acquisitions per wind tunnel speed. Plot includes CFD model analysis of measured speeds and a linear fit

This calibration plot (Figure 4.14) showed that the wind speeds measured by the acoustic transducers were very similar to those expected from CFD simulations. This confirmed that the LDWT had been correctly re-calibrated after being moved; and was measuring the correct wind speeds. Both sets of data showed a linear increase of measured wind speed with incident wind speed but the measured wind speeds were approximately a third of the incident wind speeds due to shadowing. Though some results were omitted for clarity, cross-correlation gave the closest match to the CFD model, followed by level crossing and then zero-crossing. To determine the most repeatable signal detection method, the results were re-analysed following calibration and the variability of the methods with increasing wind speed determined (Figure 4.15).

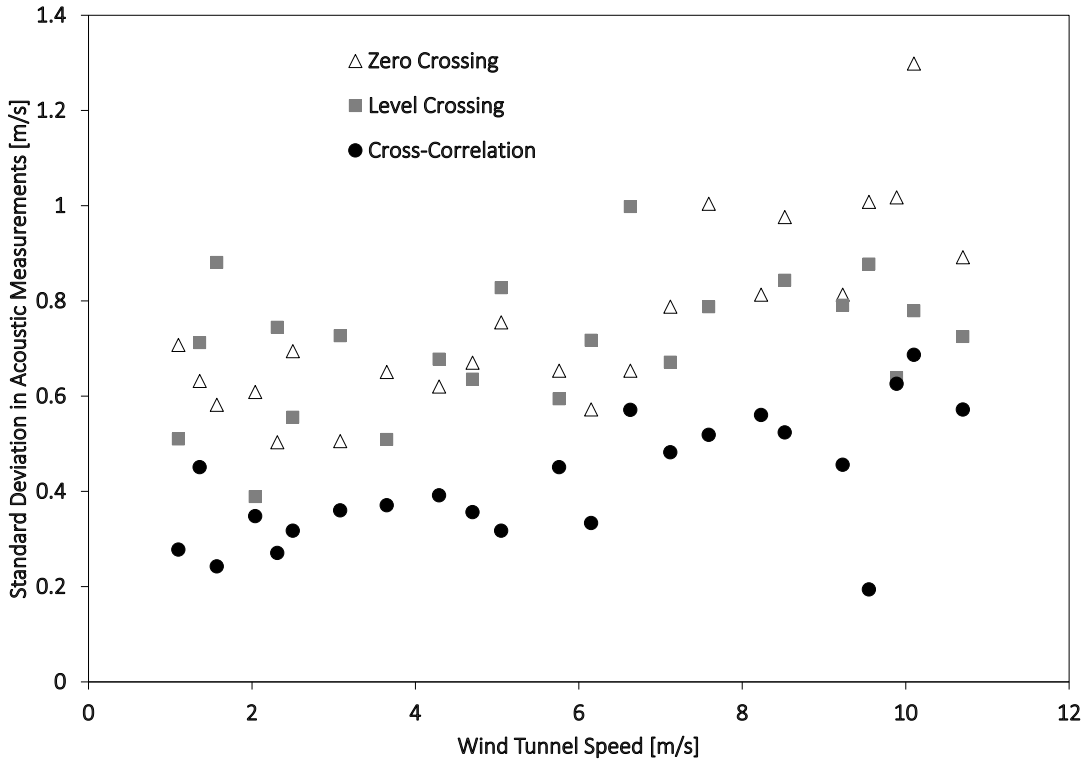


Fig. 4.15: Variation in the repeatability of the various signal detection methods with wind speed. Note that this data was calibrated to the actual incident wind speed using Figure 4.14, and each data point is the standard deviation of 15 single (unaveraged) acquisitions

The variation in wind speeds measured by the acoustic transducers was broadly constant with incident wind speed magnitude. The cross-correlation method gave the most repeatable results, with an average standard deviation of 0.42 ms^{-1}, followed by level-crossing (0.71 ms^{-1}) and zero-crossing (0.76 ms^{-1}). There was a slight increase in variation with wind speed, which was most noticeable in the cross-correlation results. This was attributable to acoustic noise and the manner in which the wind tunnel is operated, as the transducers are effectively high-sensitivity, high-bandwidth microphones. Since the LDWT is an open system, the pumps must be continually running for winds to be generated inside the chamber; varying the air mass flow rate into the chamber then produces different wind speeds. Thus, the constant errors with increasing

wind speed can be explained by the constant acoustic noise generated by the pumps rotating at a constant rotational velocity. The slight increase in noise with wind speed can then be explained by the increasing air volume passing through the very narrow orifice plates before entering the chamber. This was confirmed through further testing. The Rootes pump, which is the loudest and required for Martian pressure wind speeds >11 ms^{-1}, was found to increase the variation to an unacceptable level; the average standard deviations for the different methods became 1.53 ms^{-1} (cross-correlation), 2.56 ms^{-1} (level-crossing) and 3.23 ms^{-1} (zero-crossing). Removing the air flow into the chamber did not make any noticeable change in measured wind speed variation, the only difference occurred when the pumps were turned off. With no pumps running, and at low pressure, the variation in 100 wind speed measurements was found to be less than the 6 cms^{-1} timing resolution of the Picoscope. As a result of the loud operating conditions at the LDWT, the Rootes pumps were not used for testing and so wind speeds were limited to <11 ms^{-1} at Martian pressures. Increasing the lower cutoff of the bandpass filter to 50 kHz may have reduced the impact of the acoustic noise on the results.

AWTS Calibration

Unlike the LDWT test, which was performed in air at 13 mbar, calibration of the sensors at the AWTS facility was performed at 7 mbar in a carbon dioxide atmosphere to better simulate the Martian surface conditions. As explained in Section 4.4.1, the AWTS has only been calibrated for certain environmental conditions. The calibration data only factors in the fan RPM, and so does not take into account the variation in wind speed with pressure, composition or

temperature. Nevertheless, it was important to investigate device performance under Martian conditions (excluding temperature and dust) so, to minimise turbulence, double meshes were used for the AWTS calibration runs. Since cross-correlation was found to be the most accurate and repeatable wind speed measurement method, it was used for further calibration testing at the AWTS in Aarhus (Figure 4.16).

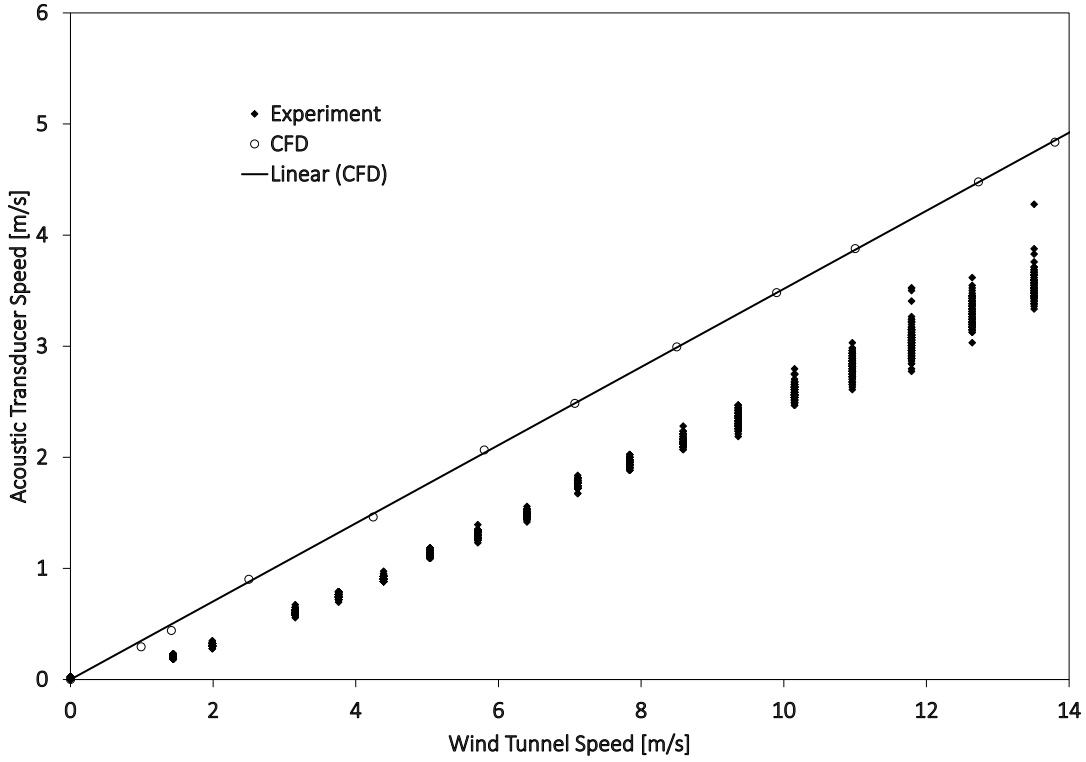


Fig. 4.16: Calibration plot of the acoustic transducers in the AWTS, including CFD model analysis of measured speeds and a linear fit. There are 100 single (unaveraged) acquisitions per wind tunnel speed.

Though there was a reasonable correlation to the CFD simulation, this calibration graph was not as linear as the LDWT calibration. However, since the wind tunnel, CFD model and transducer speeds all matched up in the LDWT, this was most likely due to calibration errors at the AWTS. The wind speeds inside the AWTS are known from a calibration of wind speed against fan RPM. These calibration curves are only available at discrete pressures, and no calibration curve is available at the test pressure (7 mbar) with double meshes in place. There is not enough data available to correct for the non-linear wind speed variation with pressure, so the closest pressure (10 mbar) calibration plot had to be used. Testing was not carried out at the calibrated test pressures as it was not known before testing commenced that the AWTS calibration was only valid at certain pressures. Whilst the AWTS data is uncalibrated for absolute velocity, it still allows for a useful comparison between the acoustic environment of the two facilities.

To investigate the increase in measured wind speed variability with incident wind velocity, the calibrated AWTS transducer data was compared to the LDWT data (Figure 4.17). The use of carbon dioxide, rather than air, had no negative effects on received signal amplitude or wind speed measurement accuracy. As predicted, there was in fact a greater received signal amplitude in carbon dioxide than air at the same pressure.

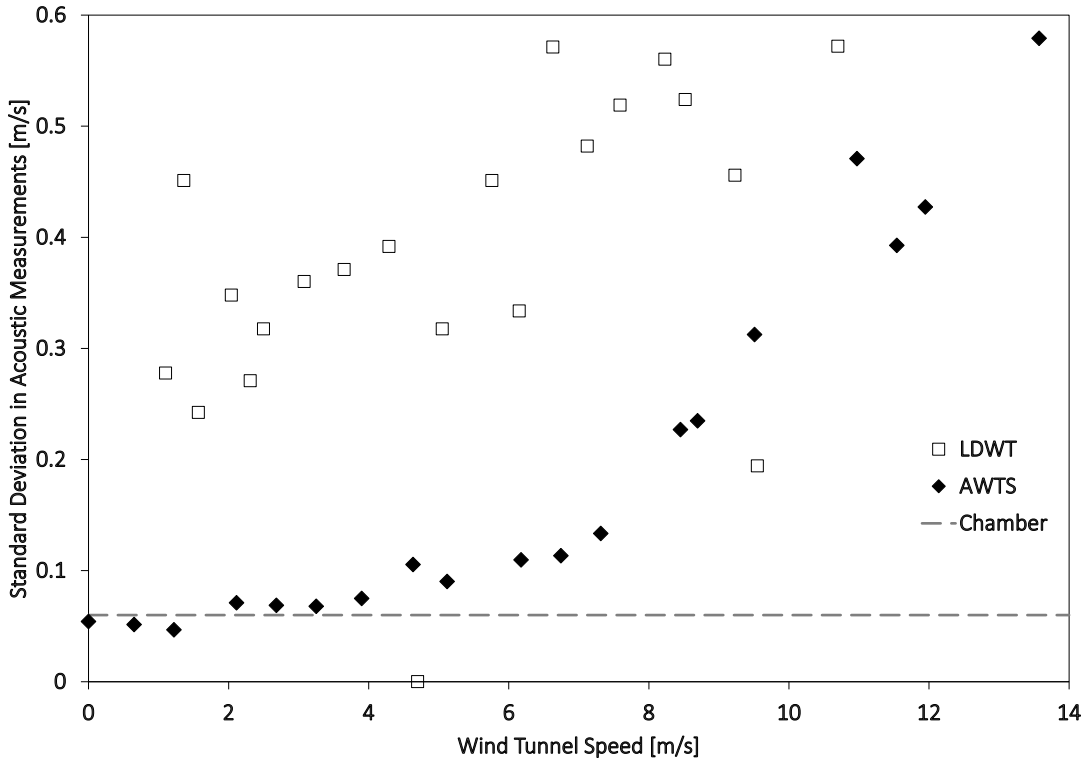


Fig. 4.17: Comparing the recorded wind speed deviations in the acoustic measurements in the two wind tunnels. LDWT data standard deviation only calculated over 15 acquisitions per wind tunnel speed, AWTS standard deviation of 100 acquisitions per wind tunnel speed (the Labview code was automated between the two test runs so could process many more signal acquisitions). The dashed line represents the standard deviation of 100 signals in the low pressure chamber (no acoustic noise or wind).

This data showed that the acoustic environment in the AWTS facility was much more favourable to calibrating acoustic wind sensors than the LDWT; though the transducer wind speed variability was highly dependent on wind speed. Once again, this could be attributed to the manner in which the wind tunnel operates. It is a closed-circuit facility in which a large vacuum chamber is pumped down to remove the air, then back-filled with CO_2 to bring the pressure up to the desired value. The chamber can be left like this for days, and fluid flows of different velocities are generated by varying the rotational speed (RPM) of fans inside the chamber. The acoustic and mechanical noise of the fans was discernible, and noticeably increased with fan RPM (wind speed). Above 600 RPM (6.3 ms^{-1}),

there was considerable noise outside the chamber and so much vibration that the tables next to the wind tunnel shook. This increase is clearly visible in the data, giving further merit to the conclusion that the observed variability was primarily a function of the acoustic and mechanical noise present at the two facilities. One additional explanation for the lower acoustic noise at the AWTS, other than the low-noise fans, is that sound travels shorter distances in carbon dioxide than air due to an attenuation coefficient which is two orders of magnitude greater than air (Section 1.4.1). Once again, with the fans not running, the measured wind speed variability was clearly limited by the 6 cms^{-1} timing resolution of the Picoscope; as illustrated by the dashed line in Figure 4.17. Note that all wind tunnel data acquisitions were unaveraged single oscilloscope traces.

Despite an un-optimised configuration, the transducers performed adequately well in terms of signal amplitude. The LDWT was well-calibrated but noisy, whereas the AWTS was comparatively quiet but poorly calibrated. The LDWT data showed that transducer response to varying incident wind speeds is linear, but did not allow for an accurate evaluation of the repeatability of results. The AWTS could not be used to calibrate the instrument, but confirmed the repeatability of results is the same as that recorded in the laboratory low pressure chamber (6 cms^{-1}). Acoustic noise would not be a problem on Mars due to the highly-attenuating atmosphere and few sources of acoustic noise [72].

4.4.5 Dust Survival

Since the transducers incorporated two-micron thin vibrating films, and sensors on the Martian surface inevitably get coated in dust, it was necessary to determine whether dust deposition would affect transducer performance. This test was performed in the AWTS chamber and involved measuring the received signal and frequency response of the transducers with varying amounts of deposited dust. In total, 80 dust injections of 2 g each were carried out. Each injection involved using a calibrated measuring scoop and spatula to ensure the same amount of dust was injected each time. The dust was placed into the injection port on the chamber using a funnel, then sealed and a valve briefly opened then closed to inject the dust into the chamber. After each injection, one hundred received signals were measured and a photo of the transducers taken, in addition to a frequency response measurement every ten injections. The test was carried out in a CO_2 atmosphere (7 mbar, 20.4 °C) at 3.2 ms^{-1} (measured by the LDA) and without meshes, to encourage turbulence.

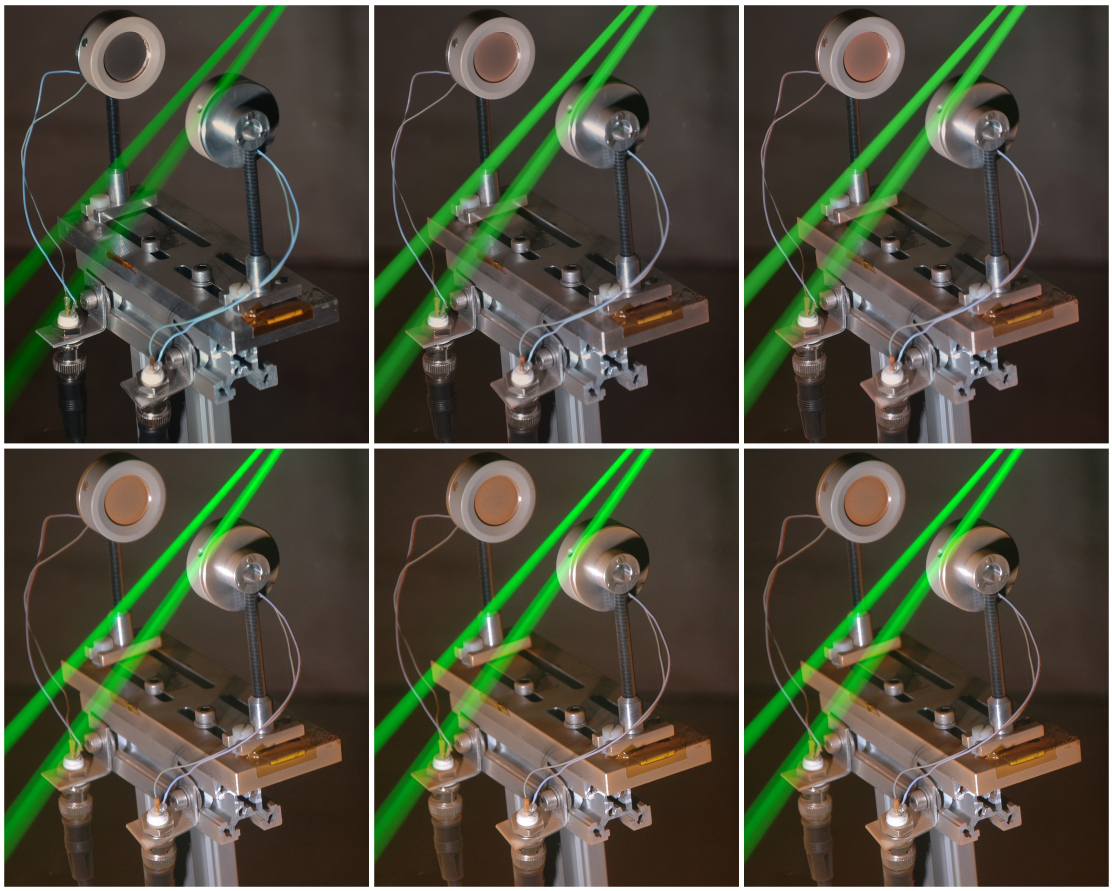


Fig. 4.18: Time lapse photos showing the amount of dust deposition every 16 injections (approximately every 25 sols)

The whole test took just under two hours, and after the test was concluded, the chamber was evacuated then back-filled with air to room pressure and opened. Three upward-facing horizontal surfaces approximately 1 m^2 in area were chosen at random in the vicinity of the test section, and the dust in those areas carefully brushed off and weighed. The average dust density was found to be 0.19 $mgcm^{-2}$, which equated to approximately 120 sols (Martian days) worth of average dust deposition or ~1.5 sols per injection. These calculations were based on conservative estimates of dust deposition rates on Mars [73]; though significant dust lifting events are possible and deposition rates during a dust storm could be considerably higher.

Over the entire length of dust deposition, there was no detectable change in frequency response. However, the amplitude of the received signal did decrease with dust buildup, but not linearly (Figure 4.19).

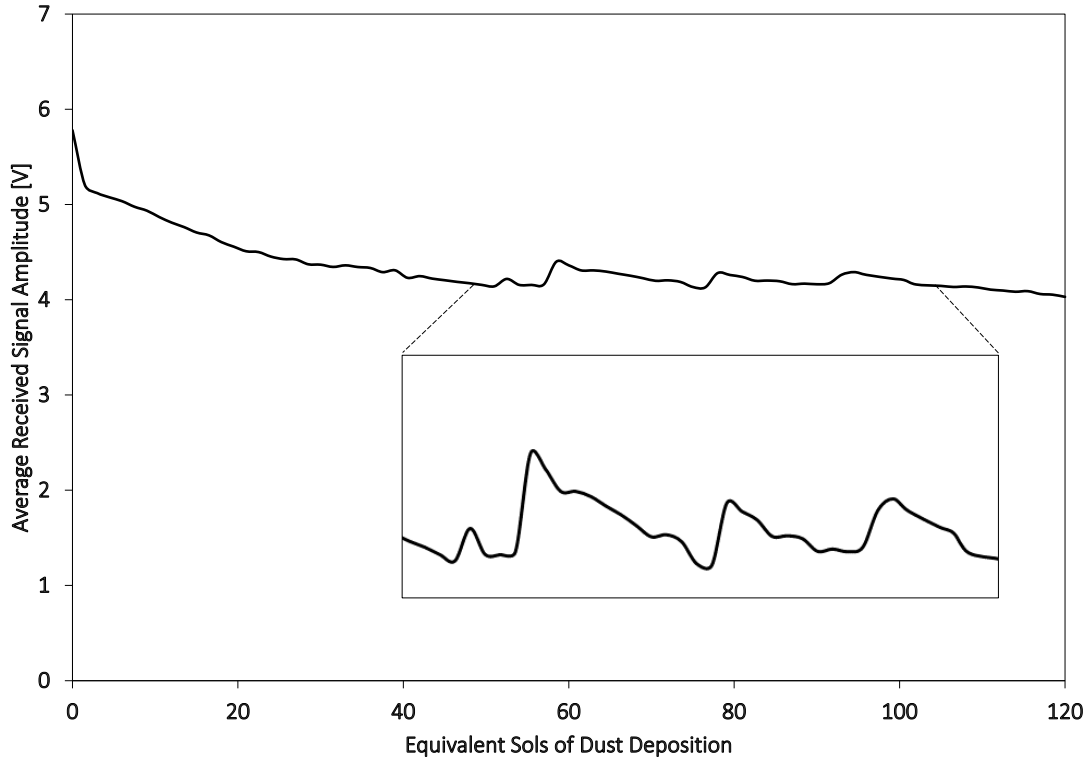


Fig. 4.19: Effect of dust deposition on received signal amplitude. Each amplitude was taken from the average of 100 signals over 10 seconds. The inset section shows four "dust lifting" events more clearly

From the data shown in Figure 4.19, it was clear that increasing amounts of dust reduce the received amplitude; as the dust effectively adds mass to the diaphragm and so changes the response of the diaphragm (Chapter 2). As more dust is deposited, the effect of any additional dust is reduced, which is also visible in Figure 4.18. Once the initial deposition has occurred, subsequent dust exposure may not result in continued build-up of the dust layer, as it is a vertical surface. There were also four noticeable "dust lifting" events between 50 and 100 sols, which served to temporarily increase the received amplitude. At an average rate of 0.011 $Vsol^{-1}$, it would take roughly 370 sols for the received

signal to disappear completely (ignoring any dust lifting events). This is equivalent to just over half a Martian year under nominal conditions, and would be considerably less during a dust storm.

However, the results show that little further degradation is encountered with additional dust exposure up to 120 sols, and the signal loss is less than 30%. As this is crucial for qualification of the transducers on Mars, the effect of dust deposition on these transducers needs to be investigated for longer durations and using analogue materials with different physical properties such as particle diameter and electrostatic charge; which may affect performance differently. If necessary, various methods could be employed to reduce the buildup of dust such as turning off the bias voltage or reversing bias direction. The impact of dust deposition on wind speed detectability would be negated if cross-correlation were used as the signal detection method, as its accuracy is independent of signal amplitude. If using level-crossing, however, a one third reduction in signal amplitude would result in a wind speed error of 30 ms^{-1} on Mars. This would be wholly inadequate for measuring the phenomena of interest (Table 1.1), and it would be impossible to compensate for in the data. Therefore, the impact of dust on transducer performance requires the use of cross-correlation as a signal detection method.

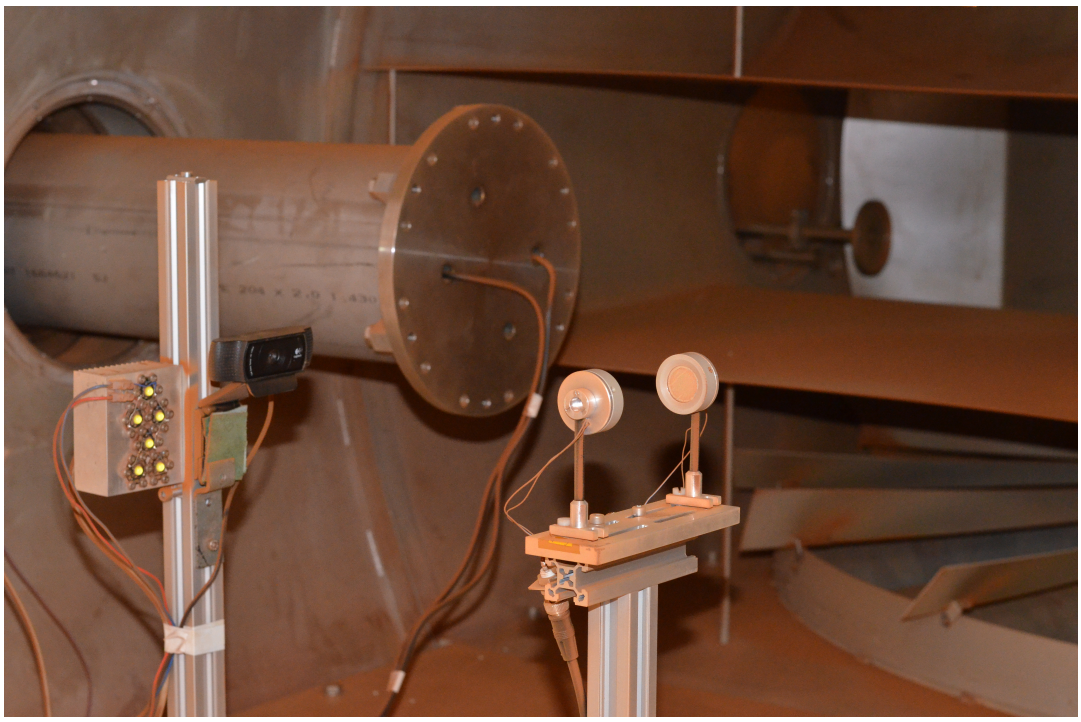


Fig. 4.20: The wind sensor shown at the end of the dust deposition experiment, when the equivalent of 120 sols of dust deposition had been simulated. The light source and webcam are visible to the left, the BNC passthroughs behind the transducers and the wind fan in the bottom right.

4.5 Thermal Cycling

The transducers were put through a thermal cycling regime to test whether they could survive the significant extremes of temperature experienced on the Martian surface. This was necessary to determine whether the expansion and contraction of the different parts at different rates would damage the transducers or affect their performance on Mars. The transducers were housed in a chamber, which was evacuated to a high vacuum (10^{-6} mbar) and the temperature varied between room temperature and -120 °C ten times, with a dwell time of an hour at each temperature extreme. Since a high vacuum was used, it was not possible to test the transducer performance at low temperatures. Due to data acquisition issues, the measured temperature profile is unavailable; however the programmed thermal cycling profile is shown in Figure 4.21.

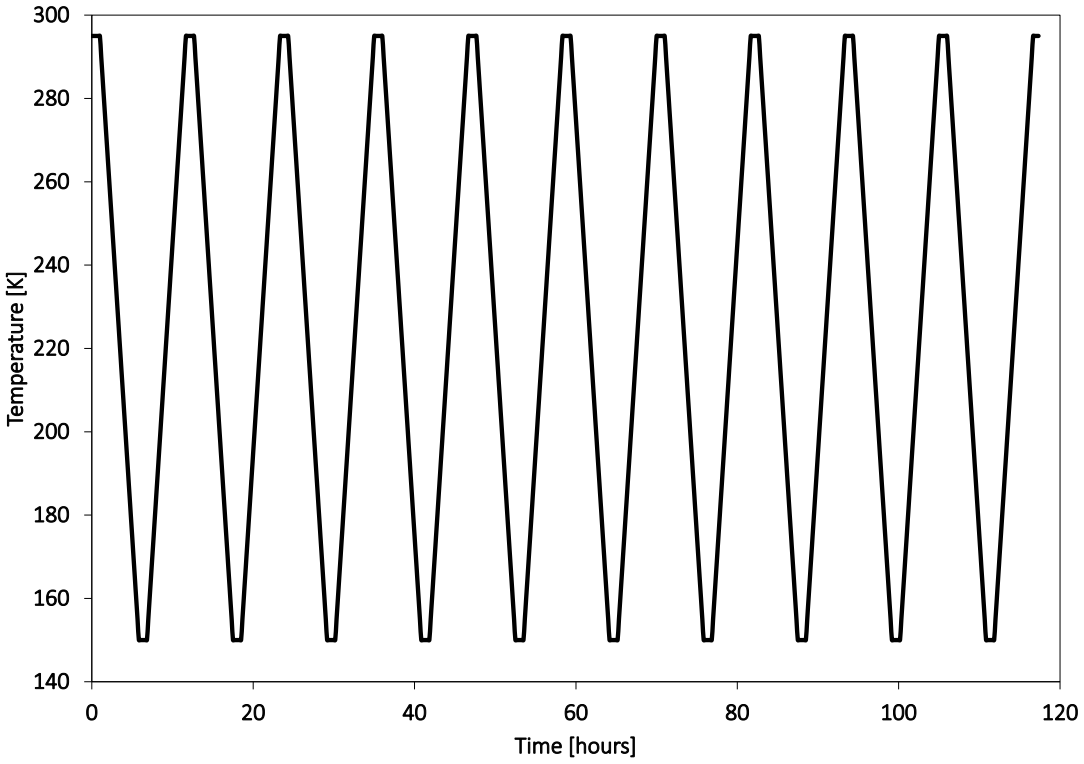


Fig. 4.21: Thermal cycling profile

Following the thermal cycling test, neither the peak frequency of the frequency response nor its amplitude were found to have changed by more than 1%. Whilst this test shows that the transducers have a survival temperature range of -120 °C to 25 °C, further testing would be required to verify the operational performance of the transducers throughout the temperature range.

4.6 Performance Assessment and Future Work

It has been shown that the transducers under development, using roughened 20 mm backplanes and 2 μm films, can achieve 5.8 V signal amplitudes with a transducer separation of 9 cm in a CO_2 atmosphere at 7 mbar; using a 60 V bias voltage and 70 V signal voltage. The most sensitive combination of film and backplane was found to yield a peak frequency response of 95 kHz; very close to

the optimum for maximum signal transmission on Mars. Wind testing confirmed that the instrument is capable of measuring wind speeds 0-30 ms^{-1} at 20 Hz with a 6 cms^{-1} accuracy (limited by the oscilloscope sampling frequency). As such, it is theoretically capable of measuring the phenomena in Table 1.1, and is currently at TRL 6. However, testing has revealed potential operational issues and this section will go on to discuss the further optimisations required before the instrument is suitable for use on the Martian surface.

4.6.1 Electronics

The current electronics will need to be redesigned to be purely comprised of flight-qualified hardware. Flight-qualified components are available to supply the optimum 60 V bias voltage, but the signal voltage will possibly need to be reduced; leading to a reduction in SNR. Given that the typical observed noise in the signal during testing was 400 mV, and even the lathe backplanes achieved an SNR of 130 under Martian conditions, this would not be an issue. A narrow bandwidth electronic filter would be required to reduce the impact of noise, especially low-frequency acoustic noise. Due to time constraints, it was not possible to evaluate how different frequency cutoffs affect the performance of the instrument. Cross-correlation would require the use of an FPGA or DSP chip; A 10 MHz processor would give a wind speed resolution of 5 cms^{-1} on Mars with a 10 cm transducer separation. A digital system, comprising a high-frequency ADC and DSP chip, would enable cross-correlation at the expense of less than a watt in power. A 3-D arrangement of transducers could operate at measurement frequencies up to 1 kHz if the transducers were measuring simultaneously, or 300 Hz if switching between transducer pairs.

The accuracy of the measured wind speed would be determined by the SNR and shadowing effects. For an instrument using 2 μm films, 0.2 mm grooved backplanes, 8 mm diameter backplanes, 60 V bias, 20 V signal, 10 cm separation and 100 kHz signal frequency, the predicted SNR under Martian conditions is 52. Therefore, either cross-correlation or level crossing could be used without signal averaging; and this suggests that the shadowing effects would ultimately dictate the optimum achievable accuracy.

4.6.2 Design Considerations

The most stringent mission constraints would likely be on total mass and volume occupied by the instrument. This would have significant implications on the transducer separation and, therefore, also operating frequency and wind speed resolution (Figure 4.22).

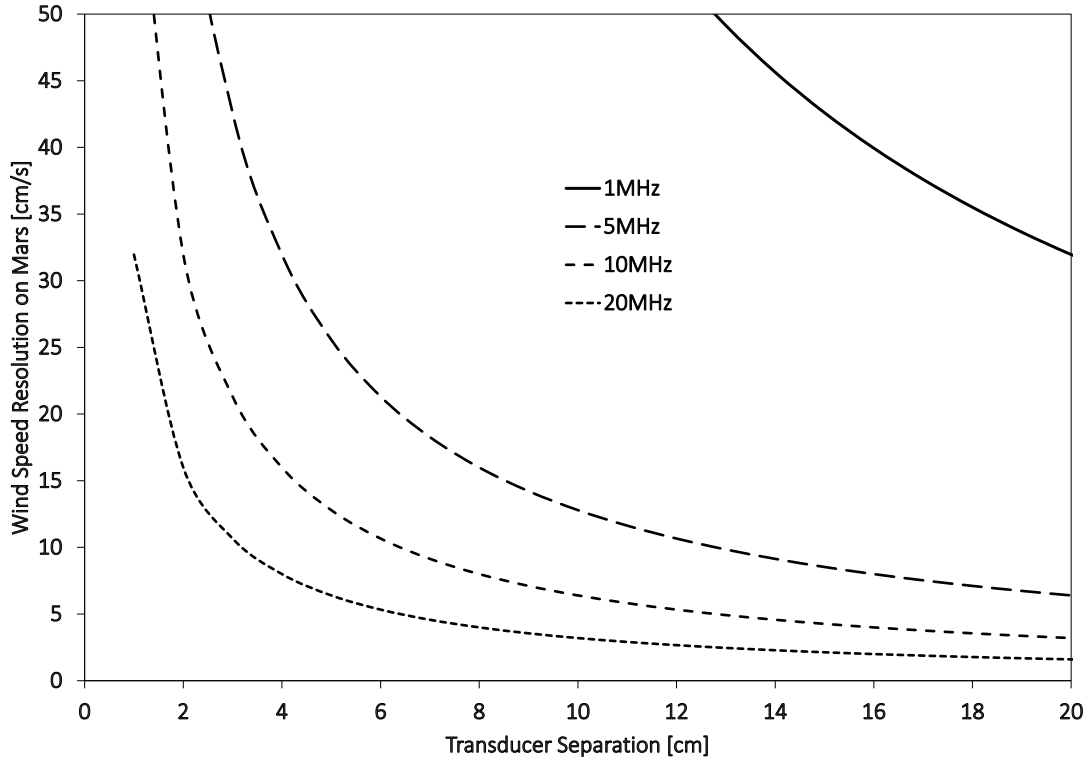


Fig. 4.22: Effect of transducer separation on measured wind speed resolution on Mars at different sampling/timing frequencies

It is evident that longer separations allow for smaller measured wind speed resolutions, which are also highly dependent on sampling/timing frequency. The separation also dictates the maximum signal length and corresponding lowest permissible signal frequency, but to a much lesser extent. For example, using the optimised chirped signal, the minimum signal frequency for a separation of 4 cm would be 17 kHz. Therefore, the effect of separation on minimum frequency can be ignored since a greater separation, in the region of 10 cm, would be preferred to greatly increase the wind speed resolution.

Figure 4.10 shows that wind speed accuracies ~0.3 ms^{-1} are achievable using a single pair of 38 mm diameter transducer heads. CFD simulations and wind tunnel testing have confirmed that the current 38 mm transducer heads result in large shadowing effects due to fluid motion around the transducers. The transducer heads will need to be made smaller (~10 mm diameter) and more aerodynamic to minimise the shadowing effects and reduce the occupied volume and mass. Whilst three orthogonal transducer pairs can compensate for the angle uncertainty in a single measurement, this needs to be tested and validated using CFD models and wind tunnel test data.

4.6.3 Wind Tunnel Testing

Both the LDWT and AWTS were found to have acoustic noise levels which interfered with anemometer operation; particularly for single, unaveraged acquisitions. Due to its large test section, the AWTS is more suitable for measurement of transducer shadowing; however the flow is only well characterised when using the LDA. This requires dust to be introduced into the

chamber so the AWTS is only suitable for development models rather than flight models. Since the accuracy of the measurements is highly dependent on noise, and the noise in the wind tunnels is much greater than on Mars, the received signal amplitude and wind speed accuracy can be more accurately determined in a low pressure chamber. More specifically, it is only the electronics that needs calibrating and not the transducers themselves. This would make calibrating flight models simpler, as the flight transducers would not need to be calibrated; only their sensitivity validated at operating frequencies.

4.6.4 Dust

The current transducers have been verified as working under Martian conditions including temperature, gas composition and airborne dust. Initial testing with Mars analogue dust has shown that there is a noticeable effect on received signal amplitude. Additional investigations are required to determine if additional dust deposition has a further impact on performance, and if cross-correlation ever fails to reliably measure the wind speed. If necessary, various methods could be employed to reduce the buildup of dust; such as turning off the bias voltage or reversing bias direction.

4.6.5 Lander Accommodation

Since three pairs of transducers will be required for 3D wind speed measurements, and to negate the effects of transducer shadowing, transducer orientations will need to be optimised for the best combination of weight, volume occupied and transducer separation. Vertical wind speeds are an order of magnitude less than the horizontal ones; so they will dictate transducer separation. The overall effect of the mast and booms on the measured wind speed will also need to be evaluated in CFD and validated experimentally. Ideally, the transducer paths should overlap to allow measurements of the smallest eddies. Some example orientations with flight-like transducer heads are shown in Figure 4.23.

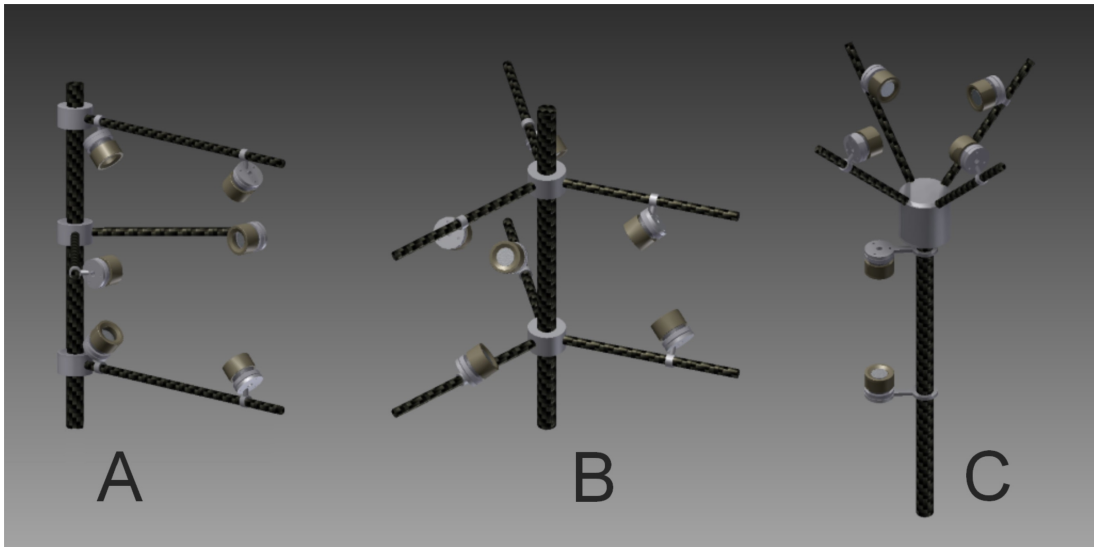


Fig. 4.23: Three different potential transducer orientations allowing for 3-D wind speed measurements

Each of the three configurations shown in Figure 4.23 have benefits and drawbacks to their use. Whilst the the transducer paths overlap completely in configuration A, it is axi-symmetric and has a centre of mass located to the side

of the mast. This would create additional strain on the mast, and require it to be thicker and therefore heavier. The transducer paths in configuration C do not all overlap, but the centre of mass is close to the mast. Additionally, this design allows the vertical and horizontal wind speed accuracies (transducer separations) to be set independently, and there is minimal shadowing from the booms. Whilst the transducer paths do not overlap in design B, which would slightly increase the size of the smallest detectable eddies, the configuration is symmetrical and also allows the horizontal and vertical paths to be set separately. As such, configuration B is the most promising candidate for further CFD analysis as a flight transducer configuration. The instrument, like any wind or temperature sensors on a surface craft, will need to be carefully located as far away from a lander as possible to minimise thermal contamination and wind shadowing errors in the measured data.

5. CONCLUSION

There is a need for wind sensors with high accuracy and measurement frequency for use on the surface of Mars. The wind data obtained from the surface to date has been adversely affected by thermal contamination and calibration issues. Improved data would not only help to constrain and validate theoretical models, but also increase safety and longevity of lander operations. The mechanical and thermal wind sensing techniques used on previous missions, whilst sufficient for basic meteorology, are wholly inadequate for measuring crucial phenomena such as dust and volatile transport. Of the two most promising candidate technologies, optical and acoustic anemometry, ultrasonic acoustic anemometers were ultimately chosen for their lower processing requirements and ability to additionally measure the speed of sound; and therefore temperature. Capacitive ultrasonic transducers were selected for their low impedance and high sensitivity, to maximise signal transmission through the rarefied Martian atmosphere. They consist of a metallised polymer film oscillating on top of a contoured metal backplane.

A theoretical framework was assembled to model transducer performance and determine which factors are the most important in determining received signal amplitude. A pair of transducers were designed and manufactured to allow for testing of a wide range of parameters including thickness of the oscillating

membrane and diameter. Tests were carried out on the assembled transducers to investigate the dependence on these parameters, and their behaviour was generally found to fit the assembled theoretical framework. As predicted, transducer performance was highly dependent on the diameter and roughness depth of the backplanes, the film thickness and bias voltage across the transducer. The frequency response was dominated by the backplane roughness depth for thin films and at atmospheric pressures; but the stiffness of the membrane dictated the response for thicker films and at low gas pressures. It was expected that there would be no received signal with a zero bias; but small signals were still observable when no bias voltage was applied to either transducer. Residual charges on the films may have behaved similarly to the bias voltage, creating an electric field between the aluminised film and backplane. The theoretical framework also failed to predict the dependence of peak frequency response with pressure, possibly due to membrane stiffness effects. These discrepancies reveal limitations of the assembled framework, to be addressed in the future.

After characterisation, the transducers were tested in two separate wind tunnel facilities to evaluate their performance at measuring wind under Martian conditions. The instrument was found to be capable of accurately and reliably measuring the wind speed in a carbon dioxide atmosphere with airborne dust. Wind shadowing by the acoustic transducers was modelled for a range of transducer diameters, and experimentally validated by good agreement with the CFD simulation. These shadowing effects were found to be dependent on transducer diameter and, whilst they could not be entirely negated, they would

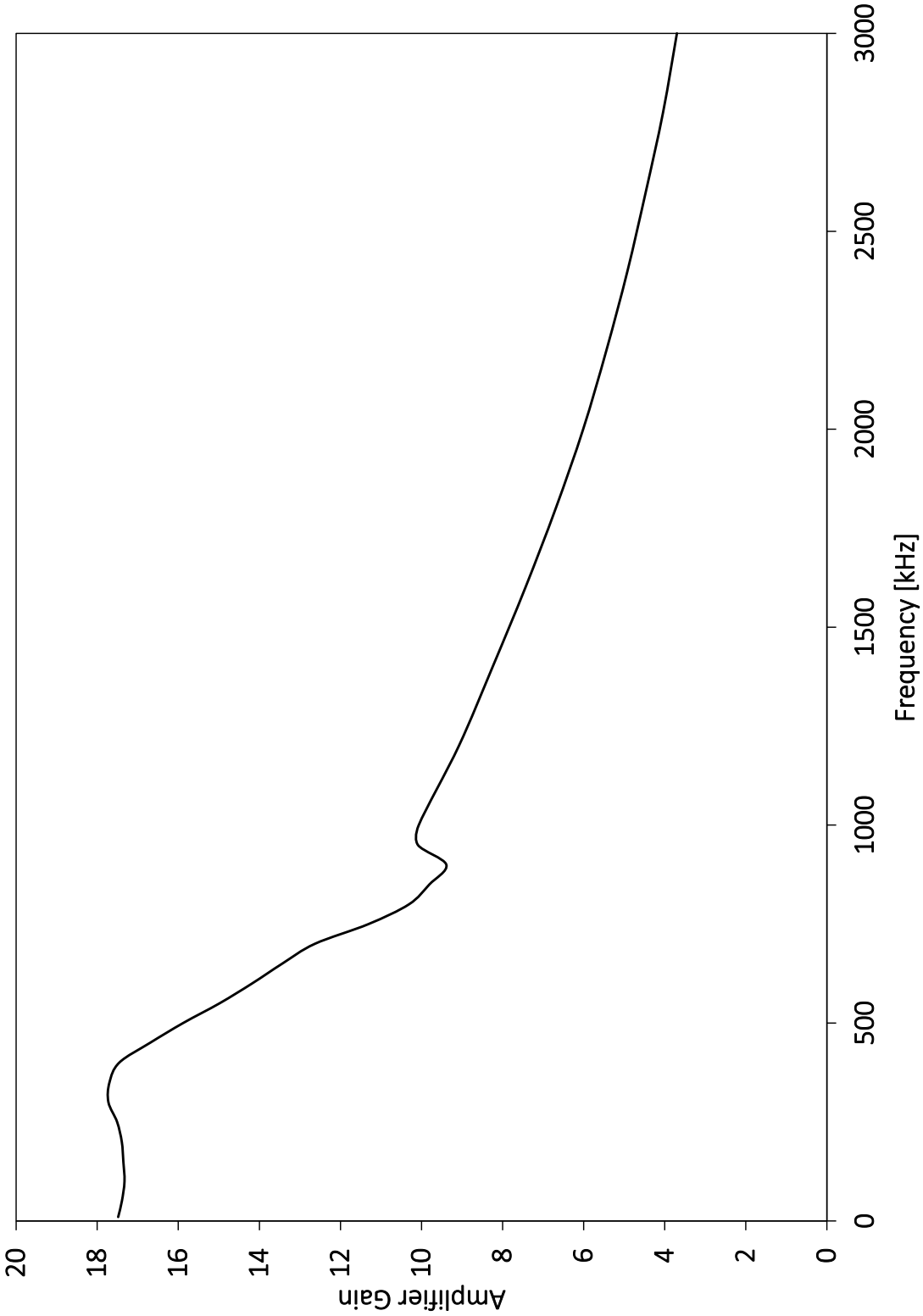
not reduce wind measurement accuracy if two or more orthogonal transducer pairs were measuring simultaneously. Acoustic noise, which limits achievable measurement precision, was found to be a problem in both wind tunnels used. The LDWT was well-calibrated but noisy, whereas the AWTS was acoustically quieter but poorly calibrated. However, the data showed that the instrument output is proportional to the wind speed, and was consistent with the independent CFD simulations of the test scenarios. Testing of the impact of dust deposition on transducer performance found that there was a noticeable change in received amplitude, but that the more dust had been deposited, the lesser the impact of any further dust. It was calculated, based on the data obtained, that these transducers would stop functioning after approximately half a Martian year of constant dust deposition.

It has been shown that capacitive ultrasonic transducers are sensitive enough and can operate at the right frequencies to operate on the Martian surface. The current design can withstand the pressure, composition, temperature variation and dust found on the Martian surface; and is capable of highly accurate and repeatable results. However, there are also two effects which need to be evaluated further. Firstly, the long-term effect of dust deposition on transducer performance needs to be addressed; including other dust analogues with different electrostatic and adhesive properties. If dust deposition is found to be a problem, methods of reducing the deposition such as grounding the films will need to be assessed. Fluid flow around the transducers and supporting beams also needs to be further investigated, to develop a technique for extracting a unique 3-D wind vector from a set of 3-axis time of flight measurements.

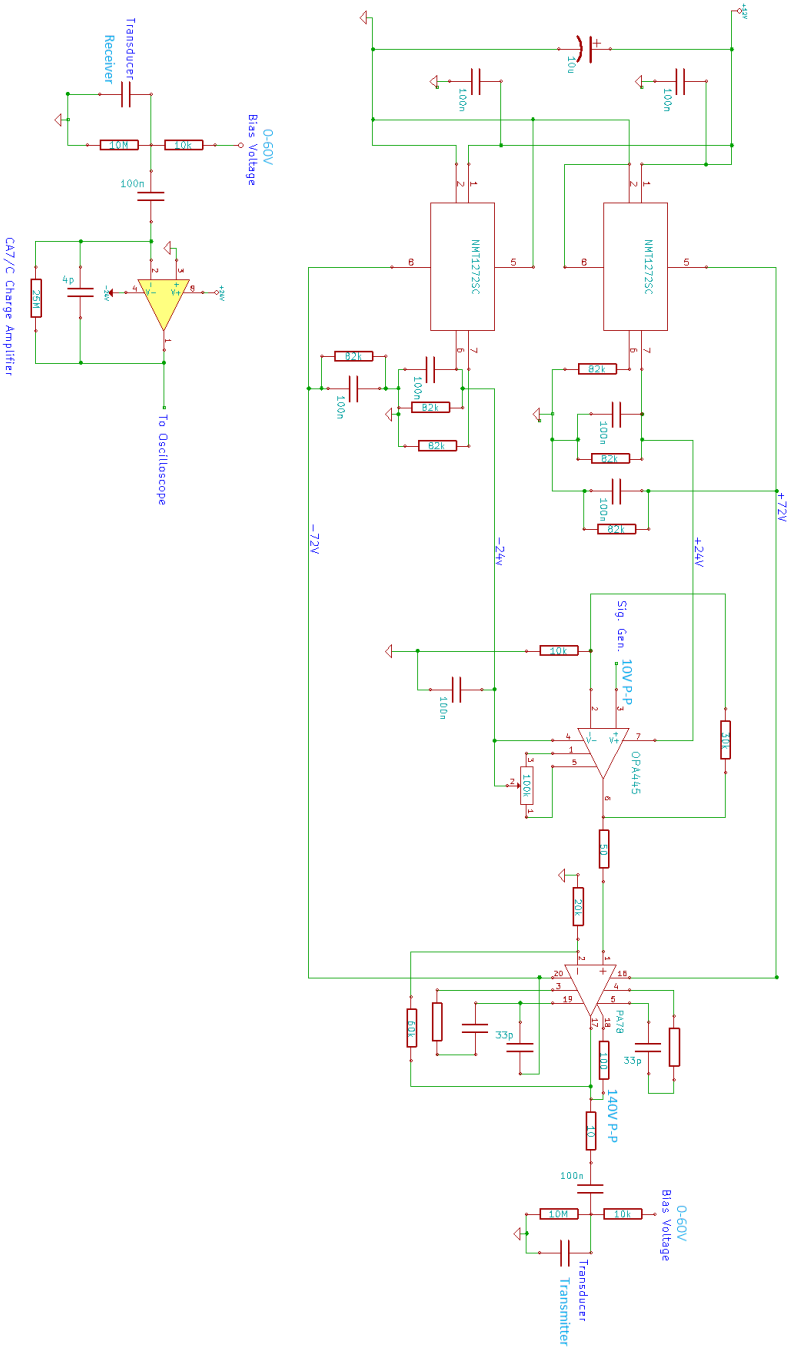
In addition to being used on the Martian surface, the developed transducers could also have applications in terrestrial anemometry, especially at high altitudes, and be adapted to other planetary bodies with atmospheres.

APPENDIX

A. AMPLIFIER FREQUENCY RESPONSE



B. ELECTRONICS CIRCUIT DIAGRAM



The custom-built transmitter electronics is shown on the right, whilst the commercial Cooknell CA7/C amplifier circuit connected to the receiver is illustrated on the left.

C. WIND TUNNEL SCHEMATICS

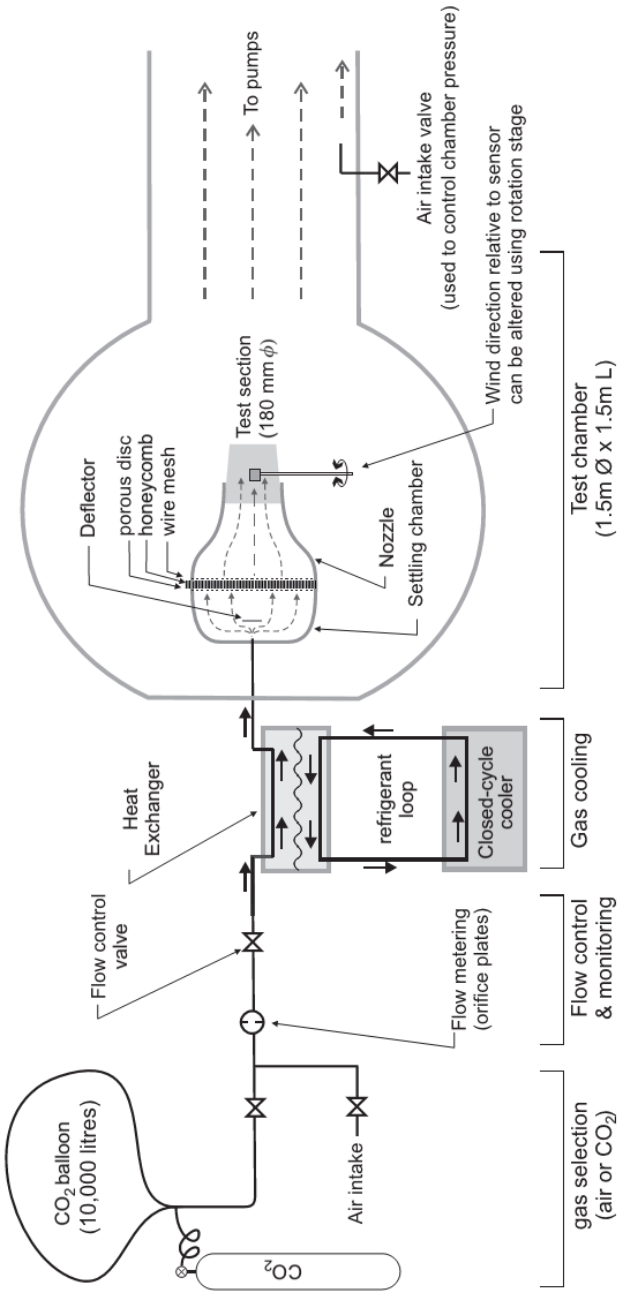


Fig. C.1: LDWT Schematics [69]

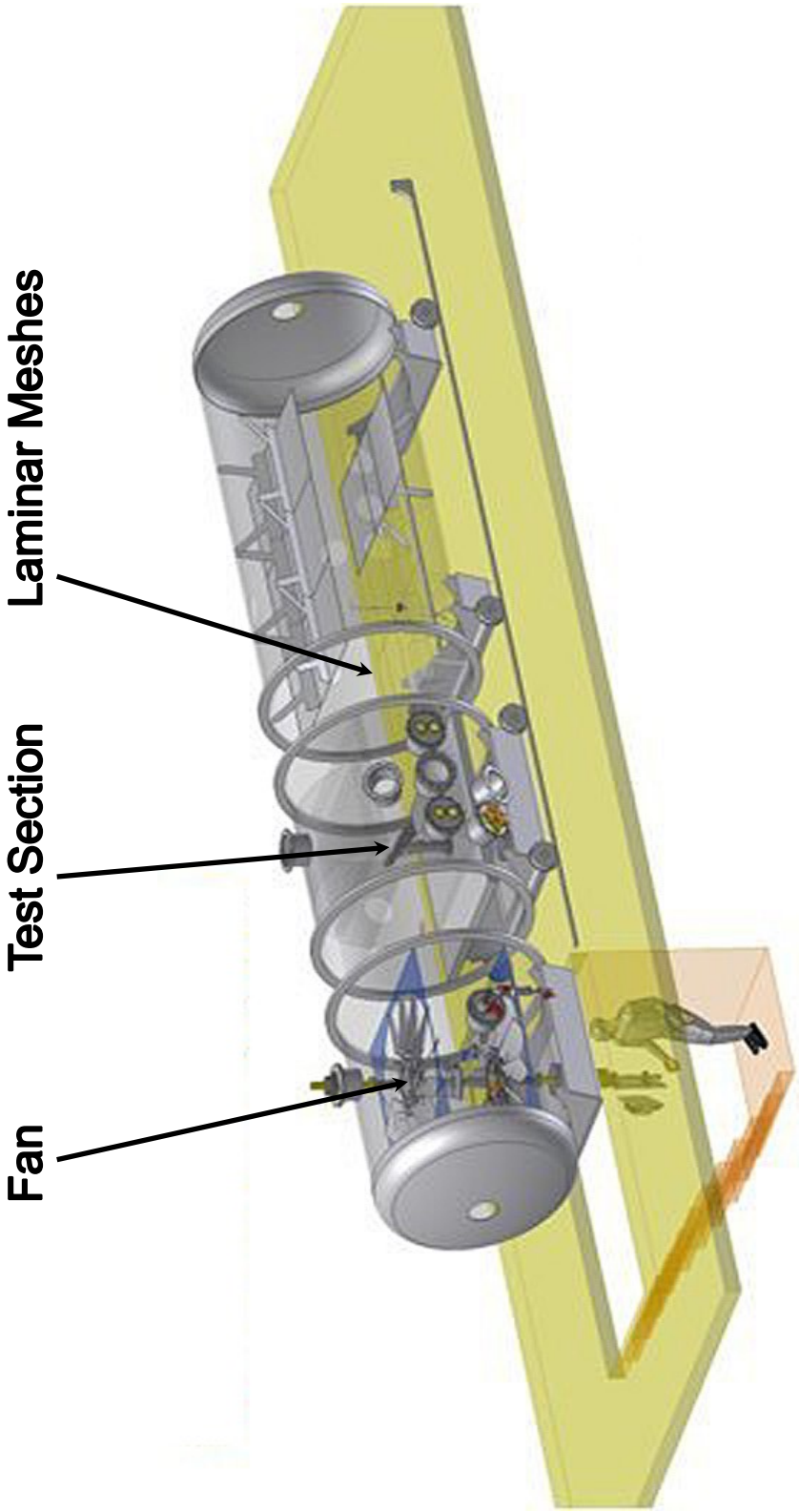
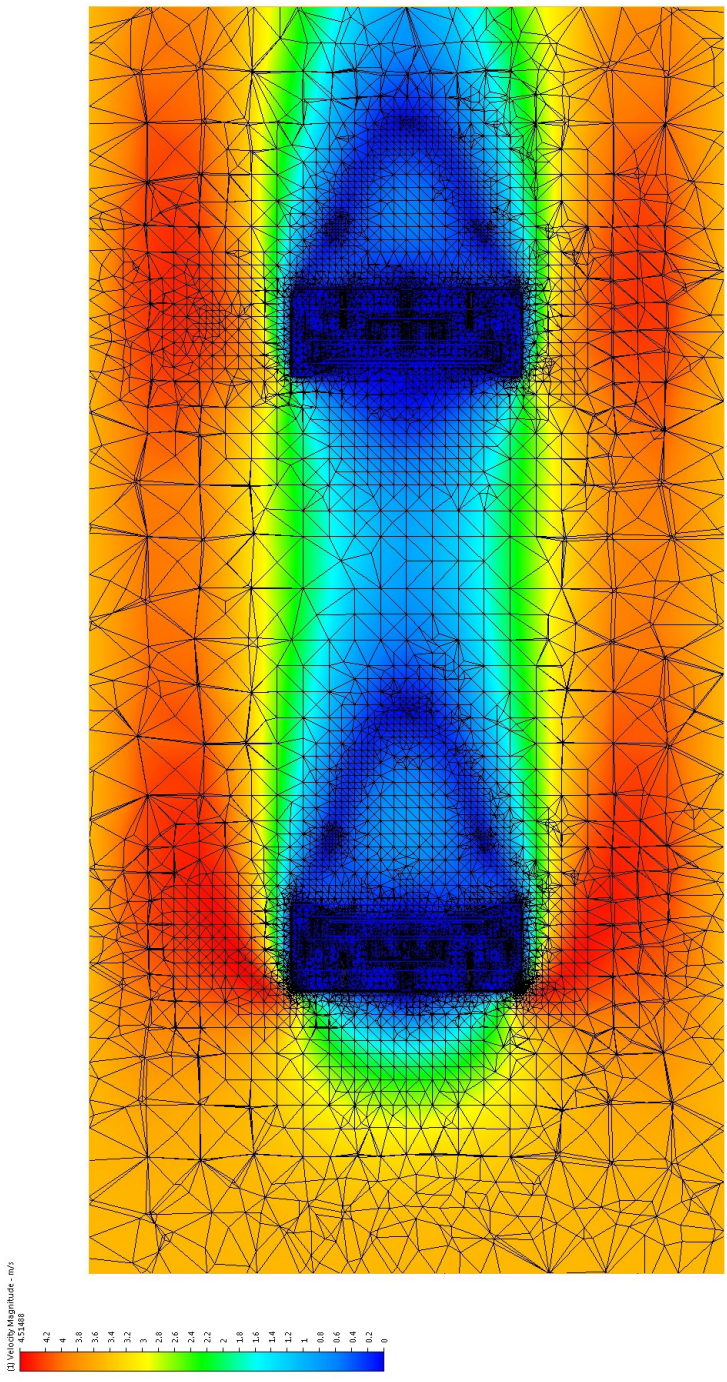


Fig. C.2: AWTS Schematics [70]

D. CFD MESH



Example mesh automatically generated by the CFD simulation for maximum shadowing of the 38mm transducers in $3.5ms^{-1}$ winds in carbon dioxide at 7 mbar

BIBLIOGRAPHY

[1] Image credit: NASA

[2] Mars Pathfinder Data,
$www{-}k12.atmos.washington.edu/k12/mars/LOPS_MPF_allavg_data.html$

[3] Mars General Circulation Modelling Group, NASA Ames Research Centre,
$http://www-mgcm.arc.nasa.gov/MGCM.html$

[4] Spiga, A. and F. Forget (2009). "A new model to simulate the Martian mesoscale and microscale atmospheric circulation: Validation and first results" Journal of Geophysical Research 114(E2): E02009.

[5] $http://upload.wikimedia.org/wikipedia/commons/thumb/f/f1/Atmospheric_boundary_layer.svg$

[6] Stull, R. B. (1988). An Introduction to Boundary Layer Meteorology, Springer.

[7] Zurek, R. W., J. R. Barnes, et al. (1992). "Dynamics of the atmosphere of Mars." Mars 1: 835-933.

[8] Sutton, J. L., C. B. Leovy, et al. (1978). "Diurnal Variations of the Martian Surface Layer Meteorological Parameters During the First 45 Sols at Two Viking Lander Sites." Journal of the Atmospheric Sciences 35(12): 2346-2355.

[9] Larsen, S. E., H. E. Jorgensen, et al. (2002). "Aspects Of The Atmospheric Surface Layers On Mars And Earth." Boundary-Layer Meteorology 105(3): 451-470.

[10] Tillman, J. E., L. Landberg, et al. (1994). "The Boundary Layer of Mars: Fluxes, Stability, Turbulent Spectra, and Growth of the Mixed Layer." Journal of the Atmospheric Sciences 51(12): 1709-1727.

[11] Petrosyan, A., B. Galperin, et al. (2011). "The Martian Atmospheric Boundary Layer." Rev. Geophys. 49(3): RG3005.

[12] Spiga, A. and S. R. Lewis (2010). "Martian mesoscale and microscale wind variability of relevance for dust lifting." Mars 5: 146-158.

[13] Balme, M. and R. Greeley (2006). "Dust devils on Earth and Mars." Rev. Geophys. 44(3): RG3003.

[14] Sagan, C. and R. Bagnold (1975). "Fluid transport on Earth and aeolian transport on Mars." Icarus 26(2): 209-218.

[15] Jasper, F. K., J. R. P. Eric, et al. (2012). "The physics of wind-blown sand and dust." Reports on Progress in Physics 75(10): 106901.

[16] Kok, J. F. (2010). "Difference in the wind speeds required for initiation versus continuation of sand transport on Mars: Implications for dunes and dust storms." Physical Review Letters 104(7): 074502.

[17] Image credit: NASA/JPL-Caltech/UA

[18] Greeley, R., M. R. Balme, et al. (2003). "Martian dust devils: Laboratory simulations of particle threshold." Journal of Geophysical Research: Planets (1991-2012) 108(E5).

[19] Stanzel, C., M. Patzold, et al. (2006). "Dust devils on Mars observed by the high resolution stereo camera." Geophysical research letters 33(11).

[20] Jakosky, B. M. and J. H. Jones (1997). "The history of Martian volatiles." Reviews of Geophysics 35(1): 1-16.

[21] Haberle, R. M., C. P. McKay, et al. (2001). "On the possibility of liquid water on present-day Mars." Journal of Geophysical Research: Planets (1991-2012) 106(E10): 23317-23326.

[22] Farahani, R. and C. F. Lange (2012). "Method for calculating near surface water vapor flux under local winds on Mars." Planetary and Space Science 73(1): 271-282.

[23] Banfield, D. (2007). MWX: The Next Generation Met Package for a Mars Network Mission. 7th International Conference on Mars, Pasadena.

[24] Lorenz, R. D. (1996). "Martian surface wind speeds described by the Weibull distribution." Journal of spacecraft and rockets 33(5): 754-756.

[25] Hess, S. L., R. M. Henry, et al. (1977). "Meteorological Results From the Surface of Mars: Viking 1 and 2." J. Geophys. Res. 82(28): 4559-4574.

[26] Image Credit: NASA/JPL-Caltech/University of Arizona/Texas AM University

[27] King, L. V. (1914). "On the convection of heat from small cylinders in a stream of fluid: determination of the convection constants of small platinum wires, with applications to hot-wire anemometry." Proceedings of the Royal Society of London. Series A 90(622): 563-570.

[28] Murphy, J. R., C. B. Leovy, et al. (1990). "Observations of Martian Surface Winds at the Viking Lander 1 Site." J. Geophys. Res. 95(B9): 14555-14576.

[29] Chamberlain, T. E., H. L. Cole, et al. (1976). "Atmospheric Measurements on Mars: the Viking Meteorology Experiment." Bulletin of the American Meteorological Society 57(9): 1094-1104.

[30] Greeley, R. and J. Iversen (1985). "Wind as a geological process on Earth." Mars, Venus and Titan: Cambridge University Press.

[31] Hess, S. L., R. M. Henry, et al. (1979). "The seasonal variation of atmospheric pressure on Mars as affected by the south polar cap." Journal of Geophysical Research: Solid Earth (1978-2012) 84(B6): 2923-2927.

[32] Seiff, A., J. E. Tillman, et al. (1997). "The atmosphere structure and meteorology instrument on the Mars Pathfinder lander." Journal of Geophysical Research: Planets 102(E2): 4045-4056.

[33] Schofield, J. T., J. R. Barnes, et al. (1997). "The Mars Pathfinder Atmospheric Structure Investigation/Meteorology (ASI/MET) Experiment." Science 278(5344): 1752-1758.

[34] Image Credit: NASA/JPL-Caltech

[35] Kowalski, L., J. Ricart, et al. (2009). "Sensitivity analysis of the chip for REMS wind sensor." Spanish Conference on Electron Devices, IEEE

[36] Gomez-Elvira, J., C. Armiens, et al. (2012). "REMS: The Environmental Sensor Suite for the Mars Science Laboratory Rover." Space Science Reviews 170(1-4): 583-640.

[37] $http://www.spaceflight101.com/msl-rems-science-reports.html$

[38] Haberle, R. M., J. Gomez-Elvira, et al. (2014). "Preliminary interpretation of the REMS pressure data from the first 100 sols of the MSL mission." Journal of Geophysical Research: Planets 119(3): 2013JE004488.

[39] Image Credit: NASA/JPL

[40] Sullivan, R., R. Greeley, et al. (2000). "Results of the Imager for Mars Pathfinder windsock experiment." J. Geophys. Res. 105(E10): 24547-24562.

[41] Gunnlaugsson, H. P., C. Holstein-Rathlou, et al. (2008). "Telltale wind indicator for the Mars Phoenix lander." J. Geophys. Res. 113(E3): E00A04.

[42] Taylor, P. A., D. C. Catling, et al. (2008). "Temperature, pressure, and wind instrumentation in the Phoenix meteorological package." Journal of Geophysical Research, Planets 113.

[43] NASA PDS Phoenix Dataset

[44] Holstein-Rathlou, C., H. P. Gunnlaugsson, et al. (2010). "Winds at the Phoenix landing site." J. Geophys. Res. 115: E00E18.

[45] Davy, R., J. A. Davis, et al. (2010). "Initial analysis of air temperature and related data from the Phoenix MET station and their use in estimating turbulent heat fluxes." J. Geophys. Res. 115: E00E13.

[46] Merrison, J. P., H. P. Gunnlaugsson, et al. (2004). "A miniature laser anemometer for measurement of wind speed and dust suspension on Mars." Planetary and Space Science 52(13): 1177-1186.

[47] Ringrose, T., J. Zarnecki, et al. (2001). "Martian dust devil detection with the Beagle 2 wind sensor." 32nd Lunar and Planetary Science Conference

[48] Petculescu, A. and R. M. Lueptow (2007). "Atmospheric acoustics of Titan, Mars, Venus, and Earth." Icarus 186(2): 413-419.

[49] Tan, P. (2009). "Examination of ultrasonic flow meter in CO2-rich applications." 8th South East Asia Hydrocarbon Flow Measurement Workshop.

[50] ISO 9613-1:1993

[51] Banfield, D., P. Gierasch, et al. (2004). "Mars Acoustic Anemometer." AGU Spring Meeting.

[52] Hietanen, J., P. Mattila, et al. (1993). "Factors Affecting the Sensitivity of Electrostatic Ultrasonic Transducers." Measurement Science Technology 4(10): 1138-1142.

[53] Grandia, W. A. and C. M. Fortunko (1995). "NDE applications of air-coupled ultrasonic transducers." 1995 IEEE Ultrasonics Symposium Proceedings, Vols 1 and 2: 697-709:1636.

[54] Banfield, D. and R. Dissly (2005). A Martian sonic anemometer. IEEE Aerospace Conference.

[55] Carr, H. and C. Wykes (1993). "Diagnostic measurements in capacitive transducers." Ultrasonics 31(1): 13-20.

[56] Fundamentals of Acoustics, L.E.Kinsler, A.R.Frey, John Wiley & Sons, PP136-138.

[57] $http://www.cooknell-electronics.co.uk/products/CA7\%20Charge\%20Amplifier.html$

[58] Matsuzawa, K. "Condenser Microphones with Plastic Diaphragms for Airborne Ultrasonics, II." Journal of the Physical Society of Japan 15: 167.

[59] Shu, Z.-Z., M.-L. Ke, et al. (2008). Design and fabrication of condenser microphone using wafer transfer and micro-electroplating technique. Design, Test, Integration and Packaging of MEMS/MOEMS, IEEE.

[60] Suzuki, K., K. Higuchi, et al. (1989). "A silicon electrostatic ultrasonic transducer." Ultrasonics, Ferroelectrics and Frequency Control, IEEE Transactions on 36(6): 620-627.

[61] Rafiq, M. and C. Wykes (1991). "The performance of capacitive ultrasonic transducers using V-grooved backplates." Measurement Science and Technology 2(2): 168.

[62] Tan, C. W. and J. Miao (2009). "Design optimization of condenser microphone: A design of experiment perspective." The Journal of the Acoustical Society of America 125: 3641.

[63] Ganji, B. A. and B. Y. Majlis (2004). "Condenser microphone performance simulation using equivalent circuit method." IEEE International Conference on Semiconductor Electronics.

[64] Haller, M. I. and B. T. Khuri-Yakub (1996). "A surface micromachined electrostatic ultrasonic air transducer." IEEE Transactions on Ultrasonics, Ferroelectrics and Frequency Control, 43(1): 1-6.

[65] Tilmans, H. A. (1996). "Equivalent circuit representation of electromechanical transducers: I. Lumped-parameter systems." Journal of Micromechanics and Microengineering 6(1): 157.

[66] http://www.ritsumei.ac.jp/se/~ sugiyama/research/re_3.1e%27.html

[67] Anderson, M. J., J. A. Hill, et al. (1995). "Broadband electrostatic transducers: Modeling and experiments." The Journal of the Acoustical Society of America 97: 262.

[68] Dugundji, J. (1958) "Envelopes and pre-envelopes of real waveforms." IRE Transactions on Information Theory 4.1 : 53-57.

[69] Wilson, C. F., A. L. Camilletti, et al. (2008). "A wind tunnel for the calibration of Mars wind sensors." Planetary and Space Science 56(11): 1532-1541.

[70] Holstein-Rathlou, C., J. Merrison, et al. (2013). "An Environmental Wind Tunnel Facility for Testing Meteorological Sensor Systems." Journal of Atmospheric and Oceanic Technology 31(2): 447-457.

[71] Nornberg, P., H. P. Gunnlaugsson, et al. (2009). "Salten Skov I: A Martian magnetic dust analogue." Planetary and Space Science 57(5): 628-631.

[72] Williams, J.-P. (2001). "Acoustic environment of the Martian surface." J. Geophys. Res. 106(E3): 5033-5041.

[73] Landis, G. A. (1996). "Dust obscuration of Mars solar arrays." Acta Astronautica 38(11): 885-891.

Further reading:

Electrostatic Ultrasonic Transducers

Bashford, A. G., D. W. Schindel, et al. (1997). "Field characterization of an air-coupled micromachined ultrasonic capacitance transducer." The Journal of the Acoustical Society of America 101(1): 315-322.

Carr, H., W. S. H. Munro, et al. (1992). "DEVELOPMENTS IN CAPACITIVE TRANSDUCERS." Nondestructive Testing and Evaluation 10(1): 3 - 13.

Clark, J. A. (1981). "A matched impedance, electrostatic approach to hydrophone design." Journal of Sound and Vibration 77(1): 51-59.

Ge, L. (1998). "A theoretical model of electrostatic ultrasonic transducers with micro air-gap structure." Chinese Science Bulletin 43(9): 728-731.

Hutchins, D. A., D. W. Schindel, et al. (1998). "Advances in ultrasonic electrostatic transduction." Ultrasonics 36(1-5): 1-6.

Li-Feng, G. (1999). "Electrostatic airborne ultrasonic transducers: modeling and characterization." Ultrasonics, Ferroelectrics and Frequency Control, IEEE Transactions on 46(5): 1120-1127.

Manthey, W. and et al. (1992). "Ultrasonic transducers and transducer arrays for applications in air." Measurement Science and Technology 3(3): 249.

Mattila, P. and et al. (2000). "Capacitive ultrasonic transducer with net backplate." Measurement Science and Technology 11(8): 1119.

Medley, A. P., D. R. Billson, et al. (2006). "Properties of an electrostatic transducer." The Journal of the Acoustical Society of America 120(5): 2658-2667.

Munro, W. S. H. and C. Wykes (1994). "Arrays for airborne 100 kHz ultrasound." Ultrasonics 32(1): 57-64.

O'Sullivan, I. J. and W. M. D. Wright (2002). "Ultrasonic measurement of gas flow using electrostatic transducers." Ultrasonics 40(1-8): 407-411.

Schindel, D. W. and D. A. Hutchins (1991). "Capacitance devices for the controlled generation of ultrasonic fields in liquids." Ultrasonics Symposium, 1991. Proceedings., IEEE 1991.

Schindel, D. W., D. A. Hutchins, et al. (1995). "The Design and Characterization of Micromachined Air-Coupled Capacitance Transducers." IEEE Transactions on Ultrasonics Ferroelectrics and Frequency Control 42(1): 42-50.

Walker, A. J. and A. J. Mulholland (2010). "A theoretical model of an electrostatic ultrasonic transducer incorporating resonating conduits." IMA Journal of Applied Mathematics 75(5): 796-810.

Warren, J. E. (1975). "Capacitance microphone static membrane deflections: Comments and further results." The Journal of the Acoustical Society of America 58(3): 733-740.

Mars Meteorology

Bass, H. E. and J. P. Chambers (2001). "Absorption of sound in the Martian atmosphere." The Journal of the Acoustical Society of America 109(6): 3069-3071.

Greeley, R. (2002). "Saltation impact as a means for raising dust on Mars." Planetary and Space Science 50(2): 151-155.

Harri, A. M., T. Siili, et al. (1995). "Aspects of atmospheric science and instrumentation for martian missions." Advances in Space Research 16(6): 15-22.

Heavens, N. G., M. I. Richardson, et al. (2008). "Two aerodynamic roughness maps derived from Mars Orbiter Laser Altimeter (MOLA) data and their effects on boundary layer properties in a Mars general circulation model (GCM)." J. Geophys. Res. 113(E2): E02014.

Holstein-Rathlou, C. (2011). "Wind related evolution of the Martian surface." PHD Thesis.

Kahre, M. A., J. L. Hollingsworth, et al. (2011). Coupling Mars' Dust and Water Cycles: Effects on Dust Lifting Vigor, Spatial Extent and Seasonality. The Mars Atmosphere: Modelling and Observations.

Kok, J. F. and N. O. Renno (2008). "Electrostatics in Wind-Blown Sand." Physical Review Letters 100(1): 014501.

Merrison, J. P., H. P. Gunnlaugsson, et al. (2007). "Determination of the wind induced detachment threshold for granular material on Mars using wind tunnel simulations." Icarus 191(2): 568-580.

Parteli, E. J. R., M. P. Almeida, et al. (2009). "Sand transport on Mars." Computer Physics Communications 180(4): 609-611.

Peter A. Taylor, W. W., Babak Tavakoli Gheynani and P-Y Li (2006). "MARS BOUNDARY-LAYER AND DUST MODELLING FOR THE PHOENIX LANDER LOCATION." Fourth Mars Polar Science Conference.

Renno, N. and J. Kok (2008). "Electrical Activity and Dust Lifting on Earth, Mars, and Beyond." Space Science Reviews 137(1): 419-434.

Ryan, J. A., R. M. Henry, et al. (1978). "Mars meteorology: Three seasons at the surface." Geophys. Res. Lett. 5(8): 715-718.

Sullivan, R., R. Arvidson, et al. (2008). "Wind-driven particle mobility on Mars: Insights from Mars Exploration Rover observations at 8220;El Dorado8221; and surroundings at Gusev Crater." J. Geophys. Res. 113(E6): E06S07.

Sullivan, R., D. Banfield, et al. (2005). "Aeolian processes at the Mars Exploration Rover Meridiani Planum landing site." Nature 436(7047): 58-61.

Taylor, P., P. Y. Li, et al. (2007). "Modelling dust distributions in the atmospheric boundary layer on Mars." Boundary-Layer Meteorology 125(2): 305-328.

Wurm, G., J. Teiser, et al. (2008). "Greenhouse and thermophoretic effects in dust layers: The missing link for lifting of dust on Mars." Geophys. Res. Lett. 35(10): L10201.